FLEXIBLE ELECTROCHEMICAL SENSORS BASED ON IRIDIUM OXIDE

FOR BIOMEDICAL APPLICATIONS

by

XUESONG YANG

DISSERTATION

Submitted in partial fulfillment of the requirements

for the degree of Doctor of Philosophy at

The University of Texas at Arlington

August, 2019

Arlington, Texas

Supervising Committee:

    Jung-Chih Chiao, Supervising Professor

    Wei-Jen Lee

    Michael Vasilyev

    Yuanbo Peng

    Yuze Sun

Table of Contents

List of Illustrations

List of Tables

List of Abbreviations

ΔI	Current Fluctuation
B12C4	Sodium Ionophore VI
DA	Dopamine
DI	Deionized Water
DOS	Bis (2-ethylhexyl) Sebacate
dV	Hysteresis Error
EDAX	Electron Dispersive Analysis
Glu	Glutamate
Glut	Glutaraldehyde
H_2O_2	Hydrogen Peroxide
I'	Current Overshoot
Ir	Iridium
$IrCl_4$	Iridium Tetrachloride
IrO_x	Iridium Oxide
iSFET	Ion-Sensitive Field Effect transistor
ITO	Tin-doped Indium Oxide
I–V	Current-Potential
K_2CO_3	potassium carbonate
K-TpClPB	Potassium Tetrakis Borate
LO_x	Lactate Oxidase
Na-TFBD	mmol/liter
PBS	Sodium Lipophilic Salt
Polyurethane	Phosphate Buffer Solution
Pt	Hydro-Aliphatic Urethane Diacrylate
PVC	Platinum
RE	Poly Carboxylate
RFID	Reference Electrode
SE	Radio-Frequency Identification
SEM	Self-Reference Electrode
SIROFs	Scanning Electron Microscopy
T_o	Sputtered Iridium Oxide Films
V'	Transition Time
WE	Potential Drift
ΔV	Working Electrode
δV	Potential Fluctuation
RE	Potential Deviation
	Reference Electrode

ABSTRACT

FLEXIBLE ELECTROCHEMICAL SENSORS BASED ON IRIDIUM OXIDE

FOR BIOMEDICAL APPLICATIONS

Xuesong Yang, Ph.D.

The University of Texas at Arlington, 2019

Supervising Professor: Jung-Chih Chiao

Considering the disadvantages of the costly, laborious, and time-consuming traditional clinical analyses, there is a tendency of developing non-hospital point-of-care which allows patients to monitor their health conditions conveniently at home. To optimize the convenience of the point-of-care instruments, a wearable device with the ability of detecting different biological components in different biological conditions is preferer. The device should also have the qualities of rapid analyses, high accuracy, and high sensitivity. To accomplish these requirements, we proposed a flexible electrochemical sensor based on iridium oxide (IrOx). As a noble metal, iridium oxide has the advantages of bio-compatible, stable, and corrosive resistance in electrolyte solutions. It also has a wide-pH sensing range, which makes it perfect material for biological conditions monitoring. Our IrOx-based sensor provides instantaneous and continuous response with high spatial and temporal resolutions. It also has the advantages of excellent flexibility, simplicity in fabrication, cost effectiveness, and low power consumption which makes it suitable for wireless data transduction. In the meanwhile, our IrOx-based sensor shows reliable performance when tested in biomimetic environment for various bio-applications.

Lactate detection by an in-situ sensor is of great need in clinical medicine, food processing, and athletic performance monitoring. In this work, we present a flexible, easy to fabricate, and low-cost biosensor base on IrOx. The sensor is characterized by the scanning electron microscopy (SEM) and the cyclic voltammetry (CV). The flexibility, durability, sensibility,

and selectivity of the sensor were examined. The sensor shows an average surface area normalized sensitivity of 9.25 µA/(cm^2 mM) with a life time of 4 weeks. It shows little response to interference chemicals, such as glutamate and dopamine.

pH is a crucial indicator in various biological conditions. Since many biological reactions are pH dependent, a responsive pH sensor adaptable to various mechanical environments is desired owning to its capability of providing real time monitoring of the reaction status. In this work, we conduct in-depth study of the performance of the IrOx-based pH sensor. The factors which could influence the performance of the pH sensor have been investigated. Various pH sensors are fabricated with different IrOx deposition techniques, different metal substrates and adhesion layers, and different sizes of the sensing area. The SEM and electron dispersive analysis (EDAX) are conducted to evaluate the physical condition and quality of the IrOx sensing films before and after used in acidic/ alkaline environment. The pH sensors are evaluated for the sensitivity, potential fluctuation, potential deviation, potential drift, hysteresis effect, interference effect, and effective pH detection ranges.

To evaluate the feasibility of utilizing our IrOx-based sensors in real-life, experiments are conducted to check the performance of the sensors for various biomimetic applications. Firstly, an ultra-flexible IrOx-based pH sensor with robust performance and simple fabrication processes is fabricated for skin test. The pH sensor is tested in flat and deformed conditions with a mechanical apparatus. A promising sensitivity of 49.3 mV/pH in the pH range between 2 and 13 at the room temperature is obtained in both scenarios. When attached to skin, the pH sensor shows excellent conformity with reliable pH response. The response time, stability, reversibility, and repeatability of the sensor are investigated in both types of physical settings. Comparing with a commercial sensor, our sensor has the advantages of smaller size, faster responding time, and better accuracy in the testing environment with insufficient liquids. Secondly, an integrated IrOx-based sensor-array is fabricated for sweat measurement. Sweat is one of the body fluids that can be obtained non-invasively and easily. Real-time monitoring of sweat can provide immediate

information about body chemistry. In this study, our multi-functional sensor-array is capable of detecting lactate concentration, sodium ion concentration, and pH level of the sweat, with excellent sensitivity, reversibility, and stability. The advantages of good conformity, low fabrication cost, and noninvasiveness make our flexible IrOx-based sensor-array a promising diagnostic tool for sweat analysis.

Chapter 1

INTRODUCTION

1.1. Motivation

Nowadays, clinical analyses have become expensive, laborious and time-consuming. Hence, there's an increasing need for the non-hospital point-of-care, which allows patients to monitor their health conditions at home continuously in a convenience way. However, there are challenges for the point-of-care measurement, such as the realization of rapid analyses with high accuracy and sensitivity. To overcome the technique challenges, studies have been conducted on the wearable electrochemical sensors. The wearable sensor realizes the personalized medicine through instant detection of the body fluids, such as the sweat. The electrochemical sensor allows continuous, precise and fast measurement. In combination, the wearable electrochemical sensor could provide instantaneous and continuous response to the in-contacted sensing sites with high spatial and temporal resolutions.

There are variety types of electrochemical sensors, such as the polymer-based sensor, silicon-based sensor, carbon-based sensor, and metal/ metal oxide - based sensor. Each of the sensors has its unique properties and advantages. Among the all the sensor types, the metal/ metal oxide - based sensor has the advantages of simplicity in fabrication, cost effectiveness, and low power consumption. For wearable biomedical applications, the essential requirements are bio-compatibility, deformability, and wireless data transduction ability. Being a noble metal, iridium oxide has the advantages of bio-compatible, stable, and corrosive resistance in the electrolyte solution. Iridium oxide also have a wide-pH sensing range. These abilities made iridium oxide a perfect material of wearable electrochemical sensors for bio-applications.

To optimize the convenience of the point-of-care instruments, the wearable device should have the ability to detect different biological components in different biological conditions. Therefore, a flexible IrOx-based sensor with multiple sensing abilities is preferred. There are several challenges: First, the feasibility of utilizing IrOx-based sensor for bio-molecules detection;

1

Second, the stability of the IrOx-based sensor in different testing environments; Third, the performance of the IrOx-based sensor in real-life tests, such as on-skin/ in-sweat measurement. Therefore, the crucial aim of my research work is to investigate the performance of the flexible IrOx-based sensors being tested in biomimetic environment for various bio-applications.

1.2. Methods and Approaches

Lactate is a common biological component with closely correlated with our lives. In food processing, by detecting the lactate concentration we can monitor the stage of the fermentation and check the freshness of the food produce. Lactate detection is also important in aquaculture and stock raising business. By tracking the lactate concentration of the fish and stocks we can get information of the health condition of the animals and limit the usage of antibiotics. Hence in the long term reduced the antibiotics consumed by human body. Checking the lactate level is also important for human. An abnormally high concentration of lactate is usually related with some disease, such as tissue ischemia, liver disease, kidney disease, sepsis and shock. Hence lactate detection is meaningful. In my dissertation, the first approach is focusing on the detection of lactate with a flexible IrOx sensor.

pH is a crucial indicator in various biological conditions. By checking pH level, we can monitor the enzyme reactions, evaluate the healthiness of digestive system, and check the stage of fermentation in food processing. The conventional pH sensors have the shortage of bulky configuration, which makes them unsuitable for in-contact monitoring. Hence developing a flexible pH sensor with good sensitivity and wide pH range is in great need. The second approach in my dissertation is focusing on the in-depth study of pH sensor based on iridium oxide.

As the laboratory experiments are often conducted in the ideal state with control groups, the feasibility of utilizing the device in real life is often questionable. Hence the real-life evaluation is necessary to evaluated the performance of the sensors. The third approach in my dissertation is focusing on the real-life measurement of the IrOx-based sensor/ sensor array for various bio-applications.

1.3. Specific Aims

- Design, fabricate, and measure the flexible IrOx-based lactate sensor in biomimetic environment. Investigate the device performance improved by the IrOx sensing film, comparing with the commonly used Au electrode.

- Conduct in-depth study to evaluate the performance, hysteresis effect, and interference effect of the IrOx-based pH sensors fabricated with various configurations, deposition techniques, and metal substrates.

- Design, fabricate, and measure an ultra-flexible IrOx-based skin pH sensor. Test the pH sensor in normal/ deformed conditions and on skin.

- Design, fabricate, and evaluate an IrOx-based multi-functional sensor-array for the detection of the physiological information in sweat.

1.4. Dissertation Architecture

There are three major parts presented in this dissertation. First part will be the design, fabrication and performance test of the IrOx-based lactate sensor which is in chapter 3. The IrOx-based lactate sensor is fabricated with MEMS technologies in the cleanroom. A control group of Au-based lactated sensor is fabricated to evaluated the difference in performance. The cyclic voltammetry experiment is first conducted to check the performance of the sensor with different sensing areas, the electrical characteristics of the sensor before and after loaded with enzymes, the difference of the surface roughness between the Au and IrOx sensing films. The cyclic voltammetry experiment is also conducted for a titration test. Then, a chronoamperometry experiment is conducted to evaluate the responsivity, sensitivity, selectivity, and longevity of the lactate sensor. The longevity of the Au-based and IrOx-based sensors are conformed with the scanning electron microscopy analysis. Finally, the lactate sensor is tested in deformed condition to check the flexibility.

The second part will be the investigation of IrOx-based pH sensors which is in chapter 4. First, the performance of the IrOx-based pH sensors fabricated with different fabrication

techniques are evaluated. The sensors fabricated with the sol-gel technique and the electro-chemical deposition technique are compared for sensitivity, hysteresis effect, and life time. Secondly, the performance of the IrOx-based pH sensors fabricated with different metal substrates are evaluated. The pH sensors made with Ni-based, Al-based, and Au-based substrates are compared for pH measurement range, sensitivity, hysteresis effect, potential fluctuation, potential deviation, and potential drift. For each metal type various adhesion layers are applied. The scanning electron microscopy analysis and electron dispersive analysis are conducted to check the surface quality of the metal film and the component of IrOx before and after use. Thirdly, the hysteresis effect of the pH sensor is investigated. The IrOx-based pH sensors made with different metal substrates and different sensing areas are tested for the hysteresis effect. Finally, the interference effect of the IrOx-based pH sensor is investigated. An IrOx-based sodium ion sensor is fabricated. A three-channel calibration system is invented to calibrated the interference effect of the IrOx-based pH sensor.

The third part will be the biomedical applications of the IrOx based sensor which is in chapter 5 and chapter 6. Frist, an ultra-flexible IrOx pH sensor is invented for skin measurement. The sensor is test in three conditions: nature condition, deformed condition, and attached to skin. The sensitivity, response time, reversibility, and repeatability of the sensor being tested in different conditions are evaluated. Secondly, an integrated multi-functional IrOx-based sensor-array is invented for sweat measurement. The sensor-array is designed to detect the lactate acid and sodium ion inside sweat, and monitor the sweat pH in the meanwhile.

The background information of the iridium and iridium oxide is expounded in Chapter 2. The future work is described in Chapter 6. The future work involves integrate the IrOx-based sensors to a wearable radio-frequency identification (RFID) integrated circuits for data transduction and logistics applications.

Chapter 2

LITERATURE REVIEW OF IRIDIUM AND IRIDIUM OXIDE

2.1. Iridium and Iridium Oxide

Iridium (Ir) is a noble metal which is stable in both acidic and alkaline aqueous environments. It also has high resistance to aggressive chemical reagents such as the oxidizing agents [2.1]. Depending on different fabrication techniques, iridium can be oxidized to various types of iridium oxide (IrOx), with different structures and kinetics effects [2.2]. The specific structure of the IrOx leads to different applications. For instance, the IrOx with high crystalline structure can be used to improve the properties of the solar cell in energy harvesting system [2.3]. The IrOx with low crystalline property is suitable for pH sensing owning to its good stability for long term measurement.

2.2. Iridium Oxide Fabrication Techniques

There are several techniques to deposited the iridium oxide film. Sputtering deposition is one of the major techniques and has become popular recently. The advantage of the sputtering deposition is that a sensing film with a distinctive rutile pattern could be achieved for the deposition conducted at 200 ⁰C. However, to achieve a stable film the deposition rate must be maintained at a very slow rate of less than 2 nanometers per minute. Other parameters such as the oxygen and argon pressure ratios, position of the target, and RF powers also need to be controlled during deposition to achieve good pH sensing parameters [2.4]. The deposition target is also costly.

Thermal oxidation is a way to achieve good quality oxide film with the thermal process. The pure iridium metal could be oxidized to iridium oxide when it is heated in the air or oxygen at a high temperature of 800 ⁰C [2.5]. The advantage of the thermal oxidation is that a thick sensing film could be achieved which provides reliable pH potentials. The disadvantage of the thermal oxidation is that a high process temperature is required, which limits the fabrication materials. To make flexible pH sensor polymer is commonly used as the substrate material, however it often cannot survive at a temperature above 350 ⁰C. The high temperature also leads to brittle sensing

film. The sensing film has a tendency to crack after the thermal process which makes the adhesion property an issue.

Sol-gel deposition is another way to deposit the iridium oxide film with the thermal process. The sol-gel deposition includes the dip-coating [2.7, 2.8] and the thermal treatment [2.9]. The iridium tetrachloride (IrCl4) is used as the starting material [2.7]. The coating precursor solution contains IrCl4, ethanol and acetic acid. The dip-coating process has a withdraw rate of around 2-centimeter per minute. By controlling the thermal treatment temperature at around 300 °C, the IrCl4 turns to iridium oxide film without impurities. By controlling the temperature and the withdraw rate we can obtain desired iridium oxide sensing films. Comparing with the thermal oxidation, the sol-gel deposition is cost effective and it is suitable for the fabrication of flexible device based on polymer substrate.

Electrochemical deposition is the technique to deposit iridium oxide film with the wet process. When the iridium is electrochemically activated in an electrolyte a hydrous iridium oxide layer is formed. To fabricate the iridium oxide sensing film, the electrode with iridium is placed in H2SO4 or NaOH solutions. A swapping potential is applied to the electrode by a potentitiostat. The advantage of the electrochemically deposited iridium oxide is its porous structure, which makes it suitable to transport water, protons and other ions [2.6]. The disadvantage is that during fabrication the current and applied potentials need to be controlled precisely. The potentitiostat and the pure iridium substrate are also costly.

Electro-deposition is another way to deposit iridium oxide film with the wet process. Comparing with the electrochemical deposition, it cost less since it does not require the pure iridium substrate. A soluble iridium precursor containing iridium tetrachloride (IrCl4), hydrogen peroxide (H2O2), oxalic acid (CH3COOH) and potassium carbonate (K2CO3) is used for deposition [2.10]. During deposition the potentitiostat is used and a current under control is applied to the electrode. The quality of the forming iridium oxide film depends on the pH level of the precursor, operating temperature, and the controlled current density. The disadvantage of the

electrodeposition is that the crystallization of the iridium oxide is not as good as the thermal oxidation process.

2.3. Iridium and Iridium Oxide for Biomedical Applications

Owning to its unique properties, IrOx has been widely accepted in biomedical applications. In neuroscience applications, IrOx electrodes has been used as the reference electrode in the electrophysiological recording and stimulation because of its high charge density, biocompatibility, and corrosion resistance in electrolyte solutions. Weiland [2.11, 2.12] reported using iridium oxide thin film as electrode material for chronic neural stimulations. The electrochemical measurements indicate that iridium oxide had low impedance and a high charge storage capacity, which make it suitable for stimulating electrode. The iridium oxide electrode also consumes less power comparing with commonly used platinum electrode.

Slavcheva reported using sputtered iridium oxide films (SIROFs) as charge injection material for functional electrostimulation [2.13]. The results obtained from the surface analysis and the electrochemical experiments indicates that the SIROFs has a unique hyperextended surface area, which provides easy access into the film by the electrolyte ions required for a charge-transfer process of a remarkably reversible type. The excellent electrochemical behavior makes SIROFs an ideal electrode material for neural stimulating electrodes, especially in the field of functional electrical stimulation.

Lee investigated the biocompatibility and charge injection property of iridium film formed by ion beam assisted deposition [2.14]. In his study, the charge injection capability of Ir electrode was compared with the commonly used Pt electrode as a stimulating neural electrode. The charge density of Pt was small and unchanged with increasing number of activating cycles, while the Ir electrode continuously produced increases in charge density. The experiment also shows that the charge injection density of Ir electrode in physiological solution is higher than the Pt electrode under the identical stimulating condition.

Iridium oxide film has stable mechanical properties on both rigid and flexible electrode, which makes it suitable for long-term experiments. Tolosa reported an electrochemically deposited iridium oxide reference electrode integrated with an electroenzymatic glutamate sensor on a multi-electrode array microprobe. It shows the IrOx film is stable during the heating, wetting and drying steps used to deposit polymer films and enzyme on the biosensing sites of the multi-electrode array microprobe. The iridium oxide electrode is suitable in long-term experiments in which the sensor might be anchored to a mammalian organ.

IrOx electrode has been used as the pseudo-reference electrodes for biomedical recording. Coung [2.16] reported a sol-gel deposited IrOx electrode for bio-electrochemical sensing applications. The reported dopamine sensor with sol-gel IrOx working and pseudo-reference electrodes on the same probe shows similar sensitivity but less noise and better limit of detection than the commonly used gold working electrode and an external Ag/AgCl reference probe. The flexible IrOx electrodes can be utilized in long-term implants to detect in situ multiple neurotransmitters for diagnosis of neural disorders.

In many biomedical in vivo applications, reduction of power consumption and elimination of wire connection are important issues. Huang [2.17] reported a flexible pH sensor based on the iridium oxide sensing film. The flexible pH sensor performed rapid responses to pH level variations statically and dynamically. The electrodes produced distinct potentials responding to various titration steps, with good stability, repeatability and reversibility.

IrOx has been used for intracortical neural stimulation. Stuart [2.18] reported an IrOx microelectrode for in vitro electrochemical potential transient measurements in buffered physiologic saline. The electrode has been pulsed in cat cortex at levels from near-threshold for neural excitation to the reported in vitro electrochemical charge-injection limits of activated iridium oxide.

Novel immunosensors based on antibodies immobilized in electrochemically grown iridium oxide thin film matrices have been developed. Wilson [2.19] reported a new method for

immunosensor fabrication with IrOx matrices. The oxide acts as a hydrophilic, highly porous, three-dimensional matrix that can immobilize antibodies and retain their activity. This research offers the potential for high antibody loadings and is suitable for mass production of sensors in an easy and economical manner.

IrOx has also been used for microfabricated biosensors and biochips. Yang [2.20] utilized IrOx as quasi-reference electrodes that operate in buffered solutions for glucose sensing. The response of the reported sensor is found to be equivalent to the response of the same sensor employing a commercial Ag/AgCl reference electrode.

In summary, IrOx has high reachable charge capacity, which is superior than the traditional metals electrode such as platinum and gold. IrOx can also eliminate the side-effects such as gas evolution and metal corrosion during charge deliveries. Furthermore, the rougher surface of IrOx film is expected to provide a larger expanded reactive area, which provides excellent electrical characteristics. The unique properties of IrOx has made it an attractive material for electrode fabrication.

Chapter 3

IRIDIUM OXIDE BASED SENSOR FOR LACTATE SENSING

3.1. Introduction

Lactate is a common analyte due to its wide variety of applications. Lactate detection by an in-situ sensor is of great need in clinical medicine, food processing, and athletic performance monitoring. In the field of food processing, L-lactate is present in fermentation of cheese, yoghurt, butter, pickles, sauerkraut, and other food products [3.1], [3.2]. Monitoring lactate concentrations can be used to assess the condition of freshness in dairy products [3.1]. In fish cultivation, health and stress levels of fishes can be monitored by testing the lactic acid concentrations, thereby limiting the mass use of antibiotics and the inadvertent consequences by human consumption of the residual antibiotics [3.3], [3.4].

In human bodies, lactate is metabolized predominantly in the kidney and liver [3.5]. The normal lactate level range in the human body is 0.5–2.0 mM/L [3.6], [3.7]. Hyperlactatemia is defined when lactate levels are between 2 mM/L to 5 mM/L [3.8], [3.9]. When lactate levels exceed 5 mM/L, the conditions indicate severe lactic acidosis [3.10]. In the fields of human performance monitoring, lactate levels play a key role to brain blood flow and has an impact on brain activation during exercise-induced fatigue [3.5]. Transient lactic acidosis can occur due to excessive lactate production from tissue hypoxia or increased cellular metabolism caused by strenuous exercise [3.10–3.12]. By monitoring the lactate thresholds in endurance athletes, a lactate sensor can inform users of their limits during exercise [3.5].

In clinical medicine, hyperlactataemia is an indicator of systemic tissue dysoxia or abnormal microcirculatory perfusion [3.13]. It may also indicate the severity liver injury and the accompanying multiple organ failure [3.11], [3.14]. Lactic acidosis is indicative of tissue ischemia, liver disease, kidney disease, sepsis, and shock [3.12]. Persisting lactic acidosis may indicate an issue with hepatic metabolism in which the lactate production exceeds the rate the liver can metabolize [3.14]. Persisting high blood lactate concentration is associated with poor prognosis

in patient mortality [3.6]. Measuring blood lactate accurately enables clinicians with an early-prediction prognosis [3.15]. High levels of local lactate within head, neck and uterine tumor cells may be associated with a greater risk of cancer metastasis [3.6]. Measuring lactate levels may lead to differentiating between metastatic and benign tumors in those regions [3.6, 3.7].

In clinical practice, blood lactate levels can be measured using central laboratory test equipment, point-of-care blood gas analyzers, spectrophotometric analyzers, and emerging hand–held devices [3.16-3.18]. The conventional analyzers have certain disadvantages, such as the large size, heavy weight, lack of deformability, and complexity of operation. Techniques such as indirect spectrophotometry, liquid chromatography, and magnetic spectroscopy [3.19–3.21] require the use of sophisticated equipment and the systems could be expansive, which are unsuitable for wearable, implantable, or disposable applications. With the increasing needs for portable devices, varieties of techniques have been presented. Baker and Gough have demonstrated a modified platinum and silver wire electrode with the pore-free silicon rubber insulation layer. The result showed a sensitivity of 10 nA/mM [3.22]. Schabmueller et al. demonstrated a micromachined lactate sensor using a titanium–platinum working electrode and titanium–platinum–iridium oxide reference electrode on a double side silicon on insulator wafer [3.23]. Burmeister et al. demonstrated a three-layered microelectrode array using Nafion and polyurethane on ceramic. The result showed a detection limit of 0.078 ± 0.013 mM [3.24]. Multi-site sensors have been investigated to monitor lactate and glucose among other parameters. Perdomo et al. have demonstrated a multi-enzyme sensor with flow channels on a microfabricated silicon chip for real-time monitoring [3.25]. Elie et al. demonstrated an amperometric sensor with arrayed platinum electrodes on a glass substrate, with linearity up to 90 mM lactate [3.26]. Kurita et al. introduced a microfluidic device with carbon film electrodes on glass plates [3.27]. The result showed a lactate detection limit of 2.3 μM.

Deformability, wireless data transduction, and low power consumption are essential for biomedical in-vivo applications. Sensors with rigid substrate such as silicon, ceramic and glass

have the disadvantages of being brittle and creating tissue damage when inserted into tissues. To address the needs, polymer-based flexible sensors have been proposed. Revzin et al. have demonstrated a lactate/glucose/pyruvate sensor array using deposited gold electrodes on Mylar substrate. The result showed a lactate sensitivity of 0.24 µA/(cm2 mM) [3.28]. Weltin et al. have demonstrated a lactate and glutamate sensor using deposited platinum/titanium electrode on polyimide foil [3.29]. In this work different membranes were studied to overcome the weak bounding problem between the enzyme and the metal electrode, which commonly exists for surface-type sensors [3.29]. Labroo and Cui have demonstrated a graphene-based lactate nanosensor on a flexible polyester film. The result showed a detection range of 0.08–20 µM [3.30]. Jia et al. have demonstrated a skin-worn lactate sensor utilizing screen-printed carbon electrodes on temporary transfer "tattoo-base" paper. The result showed lactate sensing with a linearity up to 20 mM [A31]. Khodagholy et al. have demonstrated an organic electrochemical transistor for lactate detection with an ionogel solid-state electrolyte [3.32].

In this section, we invented a flexible, light weight, micro-sized lactate sensor which can be integrated to our previously demonstrated wearable wireless module for data transduction [3.33]. The sensor configuration and the fabricated procedures have been simplified to allow low-power amplifier integration and reduce fabrication cost. A dual-electrode sensor based on lactate oxidase (LOx) has been fabricated and measured. The self-referencing method [3.34] was applied to eliminate the interference of similar chemicals such as glutamate and dopamine as well as noises from other conductive ions.

The inert and bio-compatible material iridium oxide is used to fabricate the working electrode. Cox and Lewinski have demonstrated the use of IrOx in hydrogen peroxide detection [3.35]. Schabmueller et al. have used IrOx as reference electrode [3.23]. Yet, IrOx has never been used as based electrodes for lactate detection. Based on literatures, the capability of delivering a higher charge density makes IrOx an attractive electrode material [3.36], [3.37]. A reachable charge capacity of 4 mC/cm2 is much higher than common metals such as platinum

and gold, which have the charge capacities of a few tens of μC/cm2 [3.37]. Besides, during charge deliveries IrOx can eliminate the side-effects such as gas evolution and metal corrosion, which commonly exist in metals [3.37]. Furthermore, IrOx film was expected to have a rougher surface profile than gold, which provides a larger expanded reactive area for enzyme loading. Since gold is the most commonly used material for bio-applications, we fabricated and compared the performance between the Au-based and IrOx-based lactate sensors.

There are several methods to fabricate iridium oxide films. The sputtering deposition method requires a costly target [3.38]. The thermal oxidation method requires a high temperature range [3.38]. The electro-deposition method requires a stable power supply system to control the film thickness and quality [3.39]. In this section, we chose the sol-gel process to fabricate iridium oxide [3.34]. The sol-gel process is easy to conduct without high thermal budgets.

Our flexible lactate sensor performed with good sensitivity, selectivity, and flexibility, without having to use membrane or cross-link materials. The deformable capability enables the sensor to be used on skin or in vivo. The simpler, low-cost and time-efficient fabrication method makes it possible as disposable devices. The sensor could be used for a variety of test-and-dispose bio-applications, such as food processing tests, daily ex-vivo tests for patients, infants, and seniors, and emergency-response use, without causing secondary pollution to the subjects.

3.2. Fabrication and Methods

3.2.1. Materials

Lactate oxidase (Pediococcus species), L-glutamic salt, and 3-Hydroxytyramine hydrochloride were used (Sigma-Aldrich). L-lactic acid (lithium salt) 99% was obtained from Fisher Scientific. 1.3-mg LOx was dissolved in 500-μL 1X phosphate buffer (PBS) solution to form the lactate oxidase enzyme stock solution [40]. Slight agitation was needed to accelerate the dissolution. Then the stock solution was aliquoted to 20 μL and stored at –20°C. 960-mg L-lactic acid (lithium salt) was dissolved in 10-ml 10X PBS –to form 1-M L-lactate stock solution. The stock solution was stored at the room temperature. 38 mg of 3-Hydroxytyramine hydrochloride

was dissolved in 200–mL deionized (DI) water to form the 1-mM dopamine (DA) stock solution. 37.428 mg of L-glutamic salt was dissolved in 200-mL DI water to form the 1-mM glutamate (Glu) stock solution.

3.2.2. LOx Coating and Working Principle

To load the enzymes, the frozen LOx stock solution was kept in the room temperature for half an hour until completely thawed. The stock solution was gently agitated by a syringe tip to restore uniformity. The electrodes were cleaned by DI water and dried by air. 10-µL stock solution was transferred by a Hamilton syringe and deposited onto the electrode under a stereomicroscope. The same enzyme coating process was repeated by 4 times. The sensors were sealed in a container and kept at the room temperature for 2 days before tests. This allowed the protein to be cured hence to prolong the life–time of the sensors in the testing buffer solution.

The operation of the lactate oxidase and the destruction of hydrogen peroxide at the anode were based on the chemical reactions below:

$$\text{L\_lactate} + O_2 \xrightarrow{LOx} Pyruvate + H_2O_2 \tag{1}$$

$$H_2O_2 \rightarrow HO_2 \cdot + H^+ + e^- \tag{2}$$

$$HO_2 \cdot \rightarrow O_2 + H^+ + e^- \tag{3}$$
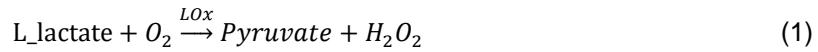
3.2.3. Gold-electrode Device Fabrication

The sensor probe was fabricated on a 125-µm thick flexible polyimide film. The substrate was cleaned by acetone and dried. Electron-beam deposition process was performed to pattern a layer of 200-nm thick gold on 50-nm thick chromium. Photolithography and wet-etching were carried out to pattern the probes with different electrode sizes of 1000 × 1000 µm², 500 × 500 µm², and 100 × 50 µm². A self-reference electrode (SE) was patterned next to the working electrode (WE) with the identical size and configuration. A second photolithography process was performed to form an insulation and protection layer. The samples were covered by SU8-25 (MicroChem) with open windows of sensing and contact pads for WE and SE. Each sensor

contained one WE and one SE closely to each other. The substrate with electrodes and connection lines was tailored by a sharp blade to a shaft shape that allowed the electrodes to be immersed in solution while the contact pads stayed above the liquid. Copper wires were attached to the contact pads by silver epoxy (Arctic Silver). The WE was loaded with LOx enzymes afterwards. The step-by-step fabrication processes and the top view of the sensor are shown in Figure 3-1. The entire sensor was covered by a SU-8 encapsulation layer while the two sensing pads and two connection pads were exposed. The WE was deposited with lactate oxidase while the SE was not. The dashed lines indicate the metal lines underneath the insulation layer connecting the sensing electrodes and contact pads. Silver epoxy was used to fix copper wires which were connected to the measurement instruments.
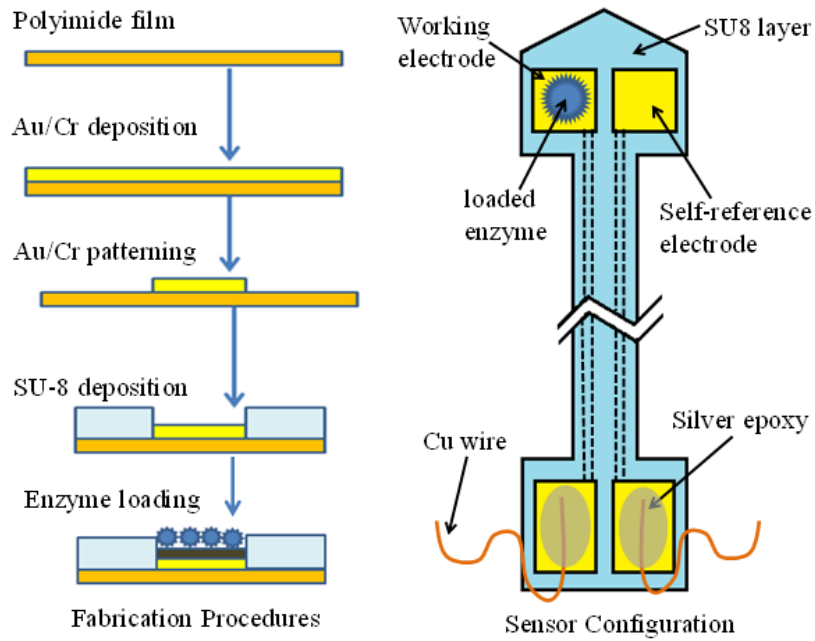
Figure 3- 1. Fabrication process and sensor configuration of the gold electrode.

3.2.4. IrOx-electrode Device Fabrication

The IrOx sensor fabrication process is shown in Figure 3-2. After metal deposition, a thick layer of SU8-100 (MicroChem) was spin-coated and patterned to form a micro-well on the god surface. Sol-gel process was conducted by dip-coated the sensor in the sol-gel solution (1-g iridium, 42-mL 95% ethanol, 10-ml 80% acetic acid). The amount of iridium accumulated on the surface was in proportional to the depth of the SU8 well. However, the SU8-100 layer became brittle with the increase of thickness and the pattern was easily damaged during fabrication. Several different thicknesses had been tested and a thickness of 100 μm was preferred. After dip coating, a layer of iridium mixture was formed on the patterned substrate, followed by a 20-minutes soft-bake at 75°C to remove the moisture. Then the flexible polyimide substrate was bent to peel off the SU8-100 layer.
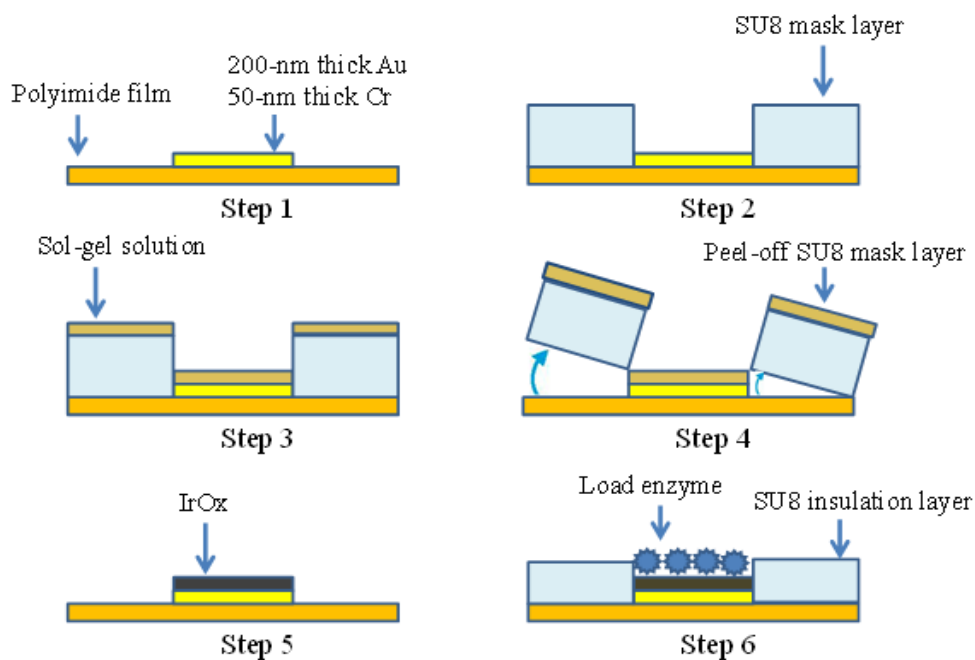
Figure 3-2. Fabrication process of the iridium oxide electrode.

Afterwards, a thermal treatment was conducted to oxidize the iridium with a heating profile from 25°C to 325°C in a 3-hours period. Then the temperature was maintained at 325°C for 4 hours, before cooling down in a 7-hours period. An SU8-25 insulation layer was patterned over the metal patterns and cooper wires were connected to the contact pads. Detail information for the sol-gel process can be found in our previous work [3.34]. Finally, lactate enzyme stock solution was loaded on the IrOx sensing film. The sensor configuration of the iridium oxide sensor is the same as the gold sensor.

3.3. Experiments and Results

3.3.1. Measurement Procedures

In comparison of the performance of the Au-based and IrOx-based lactate sensor, we conducted several experiments to investigate the property and performance of the two types of sensors. Cyclic voltammetry experiment was conducted to evaluate the surface roughness of the IrO_x and Au films. Chronoamperometry Experiments were conducted to evaluate the performance of the IrOx- and Au- based sensor such as the sensitivity, selectivity, response time, flexibility, and longevity. Scanning electron microscopy was conducted to measure the loaded enzyme quantity on the IrOx- and Au- sensing film, and to check the sensing surface quality of the IrOx- and Au- sensing film after usage.

3.3.2. Cyclic Voltammetry Characterization

3.3.2.1. CV Experiment on the Electrode with Different Sensing Areas

Cyclic voltammetry was performed on Au electrodes with different sizes before loaded with enzymes. The CV experiments were conducted in the 40-mL PBS, 150-mL KCl solution. Figure 3-3 shows the current-potential (I–V) curves of Au electrode with the sizes of 1000 × 1000 µm2 and 100 × 500 µm2. It is obvious that with a larger size the I–V curves were broader, indicating higher current values. Thus, the electrode with the size of 1000 × 1000 µm2 was expected to have a better performance than a smaller size.

17
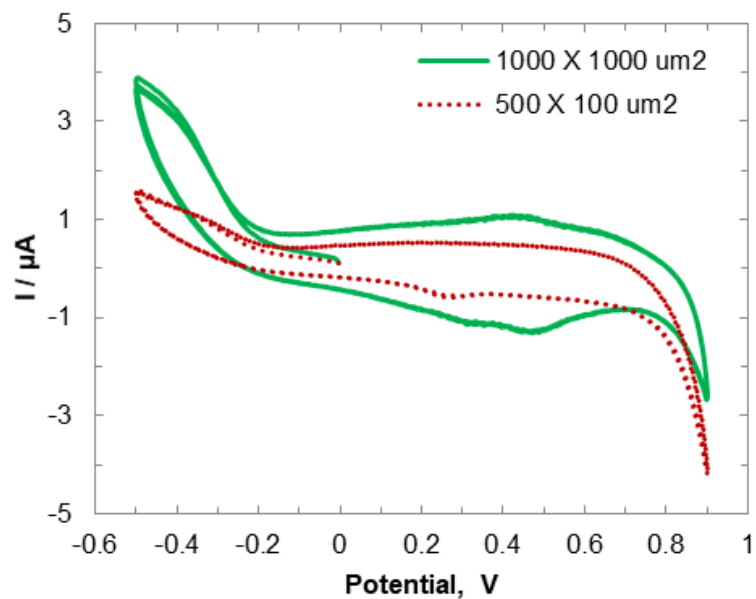
Figure 3-3. Cyclic voltammograms of gold electrodes with the sizes of 1000 × 1000 µm^2 and 100 × 50 µm^2.
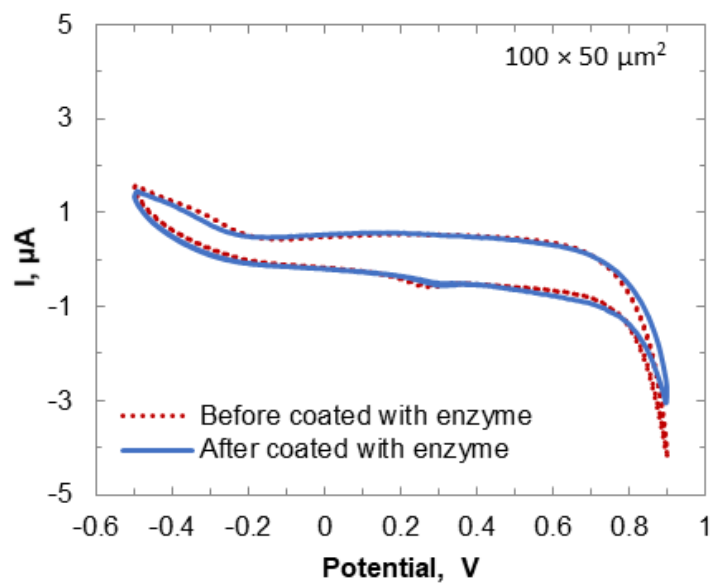
Figure 3-4. Cyclic voltammograms of the Au ensor with a size of 100 × 50 µm^2 in PBS with 150-mM KCl before and after enzyme coating.

3.3.2.2. CV Experiment on Electrode Before and After Enzyme Coating

The CV tests were performed on the $100 \times 500 \ \mu m^2$ Au electrode before and after enzyme coating. The CV experiments were conducted in the 40-mL PBS, 150-mL KCl solution. As shown in Figure 3-4, a small redox peak at 0.25 V appears after the sensor was loaded with enzyme. The result shows no enzyme blocking effect was observed, which agreed with the literature [3.40].

3.3.2.3. CV Experiment on Electrode Surface Roughness

Based on literature, the surface with a higher roughness factor provides more reaction area, which improves the sensitivity [3.41]. Cyclic voltammetry was applied to quantitatively analyze the surface roughness of Au and IrOx sensing films. The CV experiments were conducted on the $500 \times 500 \ \mu m^2$ Au and IrOx sensors in the potential window of –0.5 to +1.0 V in 40-mL 1X PBS with 150-mM KCl. A scanning rate of 300mV/s was applied.

The roughness factor can be calculated as the ratio of the active reaction area to the geometric area. The functions are shown below:

$$\rho = {A_r} / {A_g} \tag{4}$$

$$A_r = {Q_H} / {Q_{H^*}} \tag{5}$$

where ρ is the roughness factor, Ar is the active reaction area, and Ag is the geometric area. QH is the total charge, which can be calculated by taking the integral of the CV curve. QH* is the charge density for the single layer molecules of the substrate surfaces. Based on the literature, IrOx has more charge density than Au [3.42]. In the experiments, QH* (the absorption of oxygen) of 386 $\mu C/cm^2$ is applied to Au. For IrOx, it is in the range of 500–1900 $\mu C/cm^2$, depending on the film conditions [3.43], [3.44]. By taking the integral in the CV plots, the QH was obtained. Figure 3-5 (a) and (b) shows the integral regions for IrOx and Au (grey area), respectively.
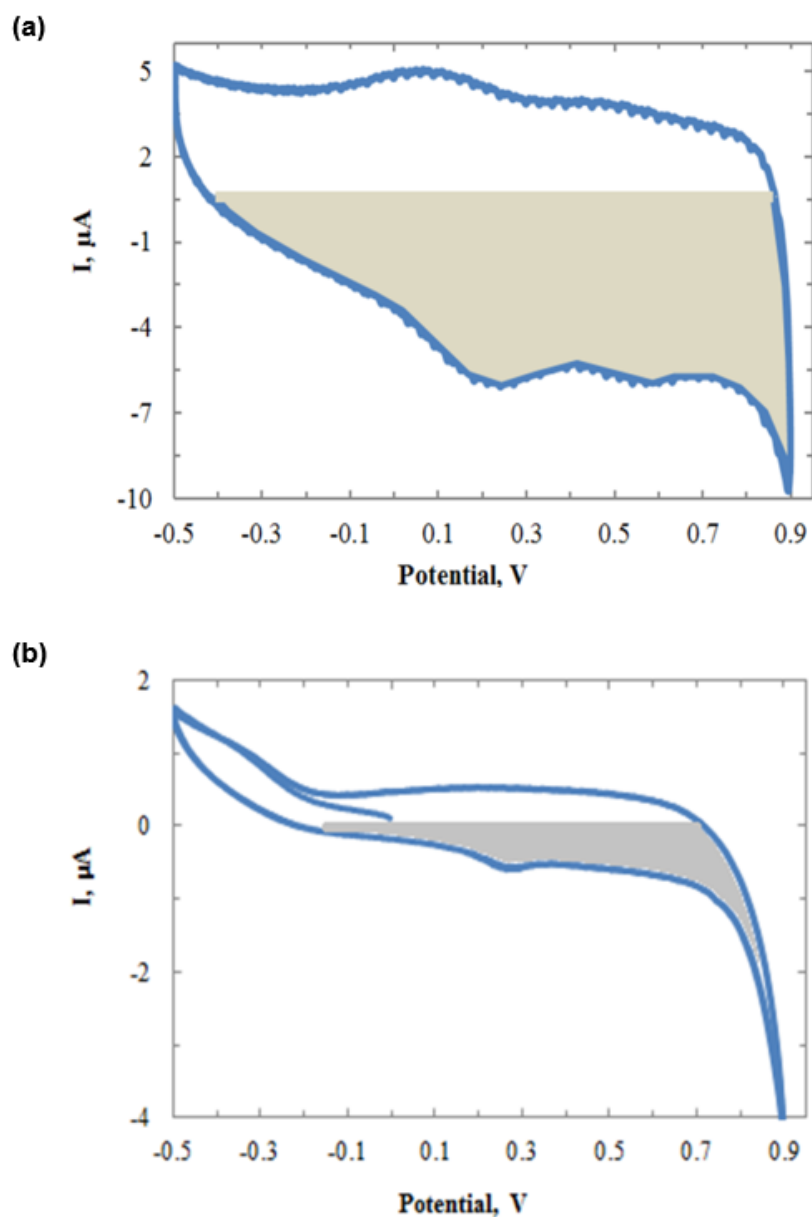
Figure 3- 5. CV plots of (a) IrOx film versus an Ag/AgCl electrode in 1X PBS at 300 mV/s; (b) Au film under the same condition. Grey areas were used for calculation of integral regions for Au and IrOx.

After calculation, the roughness factor ρ for Au was obtained as 0.512. For IrOx, QH by calculation was 5.69 and with QH* in the range of 500–1900 µC/cm2, the ρ was in the range of 1.2–4.5496. Clearly IrOx had a higher roughness factor and more enzymes could be loaded on the sensing surface. As expected, the IrOx sensing film increased the sensor sensitivity. Figure 3-6 shows the CV plots for Au and IrOx sensors with the same electrode size of 100 × 50 µm2. The result showed the conductivity was greatly improved for the IrOx electrode, with a small reduction peak observed at around 0.19 V.
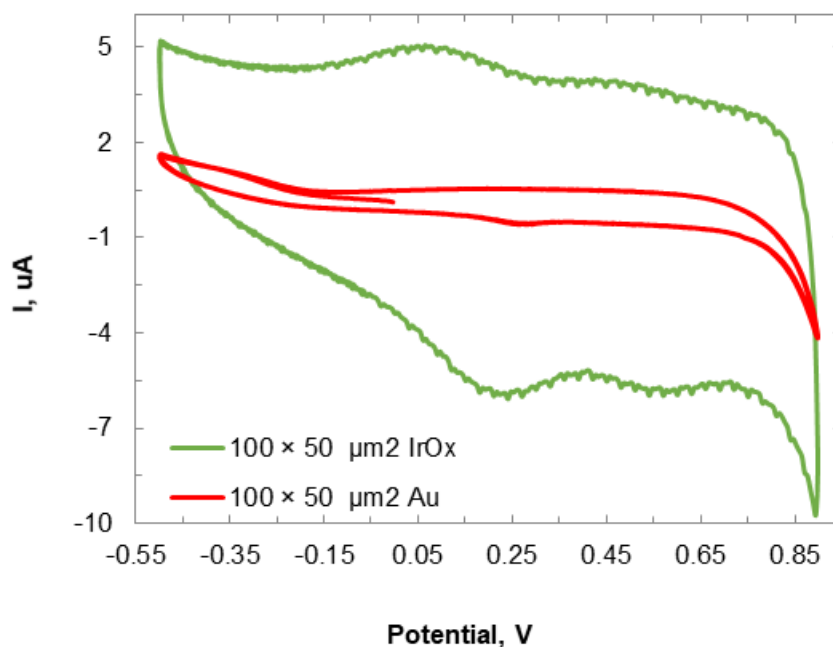
Figure 3- 6. CV plots of an Au electrode and an IrOx electrode with a size of 100 × 50 µm2 in PBS at 300 mV/s.

3.3.2.4. CV Experiment for Tiltration Test

Titration tests were conducted with the cyclic voltammetry. Figure 3-7 shows the CV traces for the IrOx sensor before adding lactate (curve #1) and with 8 successive accessions of lactate (curves #2 – #9). Each time, 80 µL lactate stock solution was applied, which led to concentrations of lactate in the beaker increased from 2 mM to 16 mM. The oxidation peak current

at the bias of approximately –0.05 V increased with respect to each addition of lactate, due to the generation of H2O2 in the enzymatic reaction. The reduction peak at approximately 0.15 V also increased, which was caused by the consequential electrocatalytic reduction of H2O2 [40]. This phenomenon was only observed on the electrode with LOx enzymes, which indicates the successful chemical reaction catalyzed by the lactate enzyme.
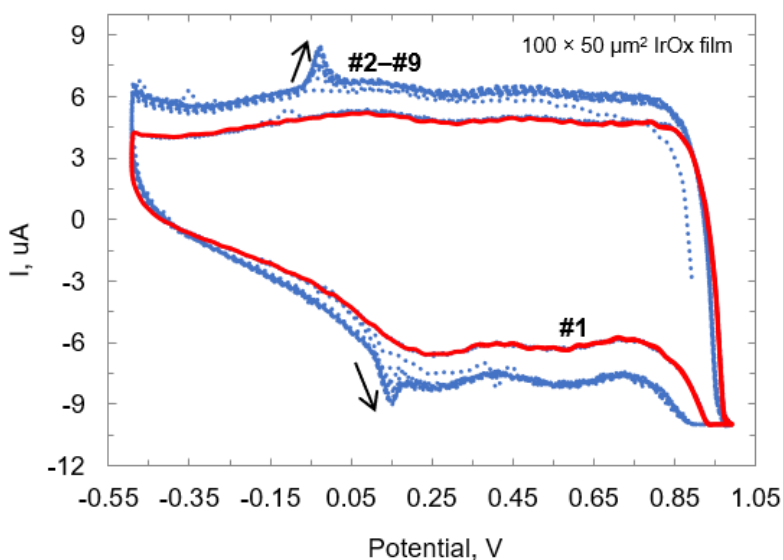
Figure 3- 7. CV plots of the IrOx electrode in PBS at 300 mV/s. Curve #1 was the CV curve before the adding of lactate. Curves #2–#9 were respective results after eight successive additions of lactate.

3.3.3. Chronoamperometry Experiments

Chronoamperometry of titration test was first conducted by the Au sensor with a size of 1000 × 1000 µm2. The performance of the sensors is shown in Figure 3-8. Successive additions of 80-µL lactate led to corresponding stepwise increases of electrical currents. After 11 additions, a shot of 320-µL lactate was added to the beaker to ensure that the current increases were from the lactate additions. Then, another 11 additions of 80-µL lactate were added successively. The increased currents produced at the Au anode in the H2O2 oxidation process were proportional to the lactate concentrations. During lactate additions, the lactate mixture was dripped closely near the gold sensing surface, and then defused into the buffer solution. The lactate concentrations at the certain dipping time points were much higher until they were diluted in the solution. Hence overshoots of signals were observed when the lactate was first added.

To make it consistent, we define the performance of the lactate sensor in Figure 3-9. The current overshoot (I') was defined as the difference between the peak current value and 90% of the saturated current value. The overshoots ranged from 0.6 nA to 1.5 nA in different additions of
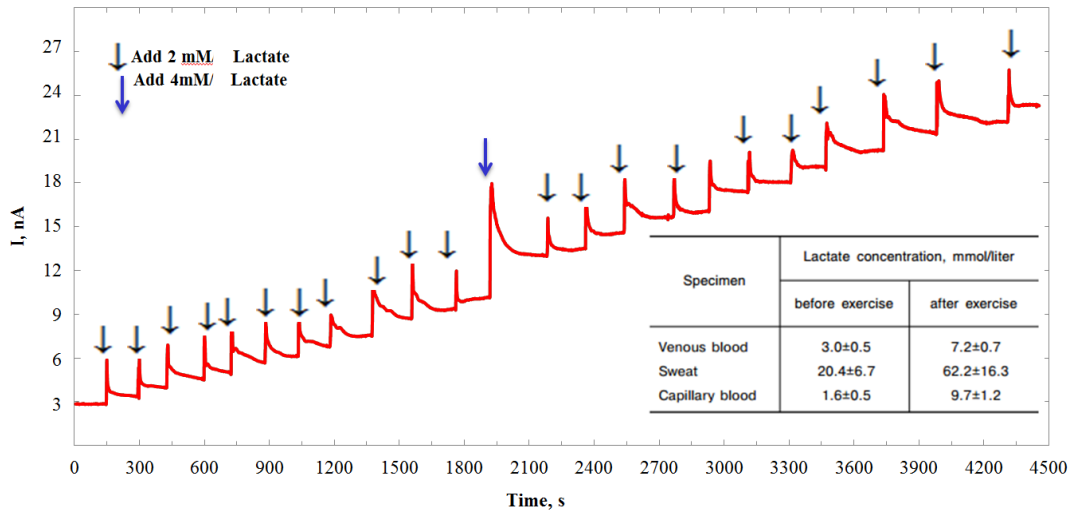
Figure 3- 8 Time-current plot for the enzyme coated Au electrode in 1X PBS with the response to lactate addition. The arrows indicate additions of lactate solution.
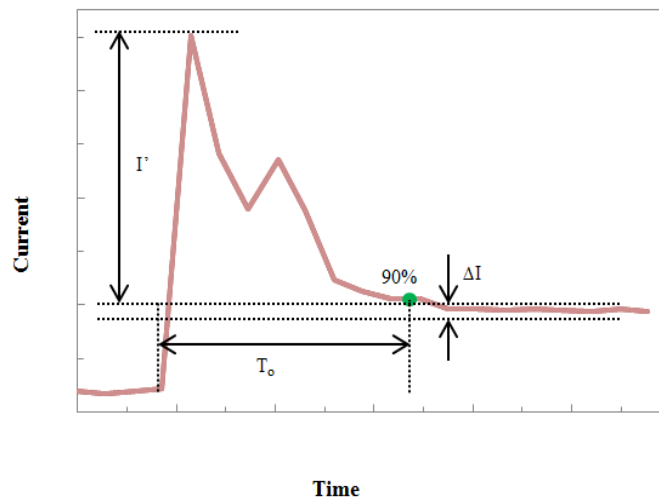
Figure 3- 9. Definition for current overshoot (I'), current fluctuation (ΔI), and transition time (To).

lactate. The current fluctuation (ΔI) was defined as the current variation range after the sensor reached a stable condition. The current fluctuation may be caused by the system noises such as the electrical noises, electromagnetic interferences, vibration of the testing instrument and liquid dynamics. The current fluctuation was typically less than 0.15 nA. The transition time (To) was defined as the time period from the beginning of the current overshoot until the current reach to 90% of the saturated current value.

3.3.4. Study of Responsivity

Measured current results were plotted at different time points after each addition of lactate to investigate the transition time. Figure 3-10 shows the currents became stabilized after the 100th s measurement points as the data points overlapped after 100th s. Thus, our lactate sensor has a responding time of 100 seconds.

3.3.5. Study of Sensitivity

The currents measured at 100th s after the overshoots were evaluated for the sensitivity.
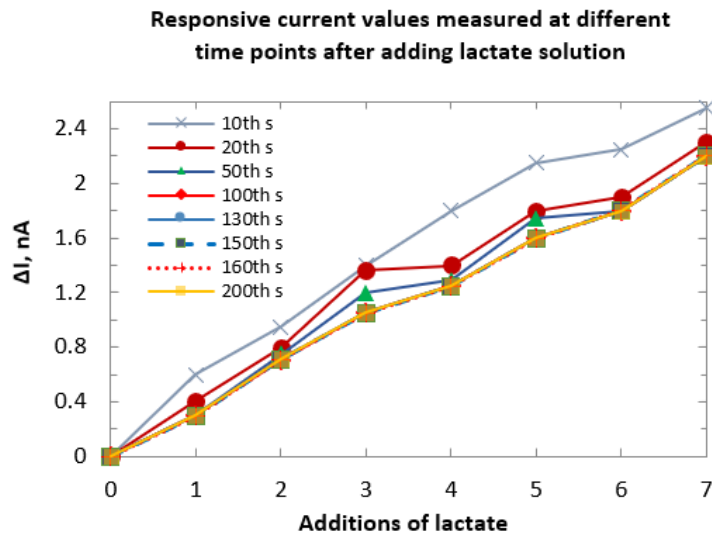
Figure 3- 10. Responsive current values at different time points after adding lactate solution.

The titration test showed a sensitivity of 129.6 pA/mM for the Au electrode with the size of 1000 × 1000 µm2. The titration test was also conducted on the 100 × 50 µm2 Au electrode to investigate the sensitivity for different sensing area sizes. Figure 3-11 shows the sensitivity comparison between the 1000 × 1000 µm2 and 100 × 50 µm2 Au electrodes. The sensitivity decreased from 129.6 pA/mM to 47.5 pA/mM. Hence larger sensing area size provides higher sensitivity.

However, the increased size was not proportional to the increased sensitivity. This may be due to the surface tension from the enzyme stock solution on the electrodes. The enzyme mixture was a suspension in which the LOx biomacromolecules were not evenly distributed. After the air-dry process, the proteins most likely located on either the center or the boundary of the solution drop. For the smaller sensing pad, relatively more in percentage of the proteins were accumulated on the metal. Thus, more current density was produced in a smaller area. This issue may be able to resolve with robotic suspension to apply the enzyme, which is commonly performed in pharmaceutical practice.

Same titration test was conducted on the iridium oxide lactate sensor. Figure 3-12 shows the sensitivity comparison between Au electrode and IrOx sensor with the electrode sizes of 100 × 50 µm2 and 1000 × 1000 µm2. After applying IrOx to the electrode, the sensitivity increased from 47.5 pA/mM (Au-based sensor) to 462.5 pA/mM (IrOx-based sensor) for the sensors with the size of 100 × 50 µm2. For the sensor with a size of 1000 × 1000 µm2, the sensitivity increased from 129.6 pA/mM (Au-based sensor) to 1125 pA/mM (IrOx-based sensor). The results showed IrOx increased the sensitivity by around 10 times for the same sensing size.

However, for the IrOx-based electrode the increase in sensitivity is still not proportional to the increase in size. The surface tension issue of enzyme coating remained a problem for the IrOx-based electrode and yet to be solved in the future.
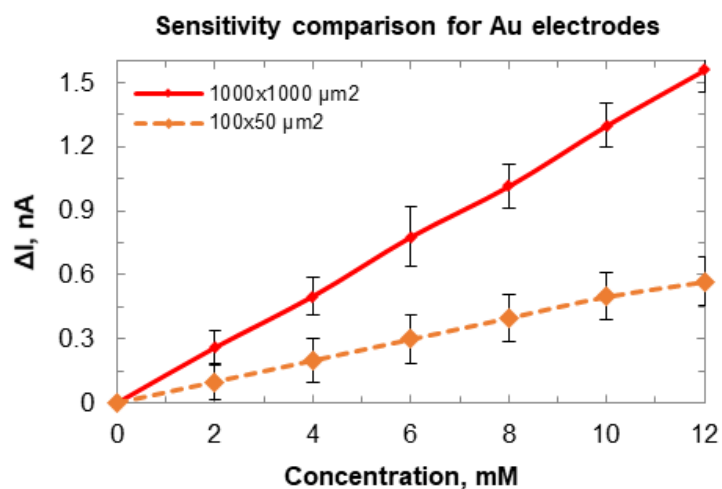
Figure 3- 11. Sensitivity comparison for Au electrodes with sensing areas of 1000 × 1000 μm^2 and 100 × 50 μm^2.
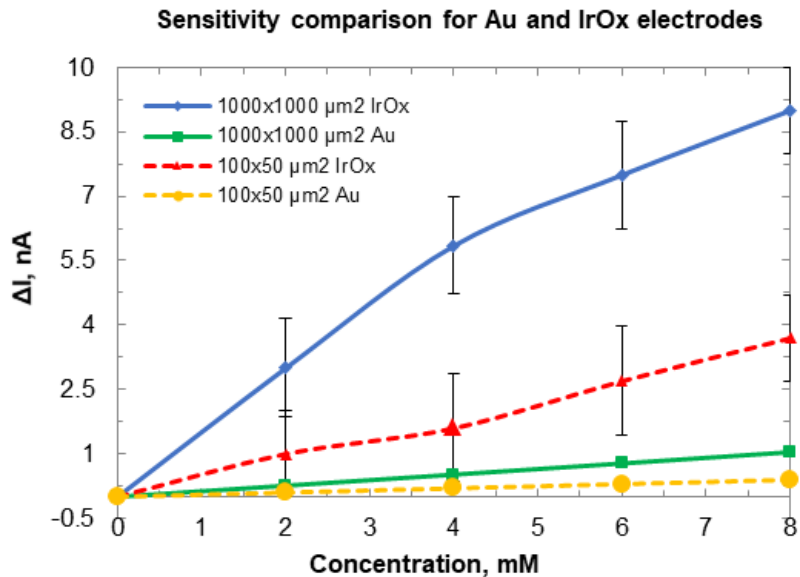
Figure 3- 12. Sensitivity comparison for Au- and IrOx -based electrodes with the sizes of 500 × 500 μm^2 and 1000 × 1000 μm^2.

3.3.6. Study of Selectivity

Glutamate and dopamine were used as the interference bio-molecules. They were applied to the Au lactate sensor individually. Figure 3-13 shows the sensor current responses to lactate, glutamate and dopamine. 50-µL Glu and 10-µL DA were added in turns after 3 accessions of 80-µL lactate. The baseline currents were different for the WE (with LOx) and SE (without LOx) because the loaded enzyme changed the impedance of the WE. The baseline currents were recalibrated. Then the SE values were subtracted from those of WE to remove the interference effects which were more noticeable for the DA (on the right side of the red dotted curve). The net values (blue curve) showed that the sensor had no responses to Glu and DA.

The sensor was then removed from the beaker and cleaned by 1X PBS solution. The second and third experiments were conducted separately with respect to Glu and DA. Figure 3-14 (a) shows the sensor responses to the additions of lactate and glutamate. The LOx enzyme modified WE had corresponding responses to lactate while the bare Au SE showed no response. Both WE and SE showed no responses to Glu since it was not an electrode reactive component. The two overshoot signals from the SE were induced by the electron turbulence when the Glu was first added to the beaker. The noises in WE were noticeable compared with those in SE. The reason may due to the interference induced by the chemical reaction conducted on the sensing film.

Figure 3-14 (b) shows the sensor response to dopamine. Both WE and SE showed similar responses caused by the oxidation potential of DA on electrodes. The subtracted values (green dotted curve) showed little response to DA. However, some overshoot and disturbance signals were observed. This was due to the different time delays in the WE electrodes, with or without LOx, because it was difficult to add the DA solution at the exactly equal distances to the two electrodes. The results showed the self-referencing technique can eliminate the interference caused by DA. The selectivity test demonstrated that the sensor probe was responsive only to the additions of lactate.

The selectivity test was also conducted for the IrOx-based lactate sensor. Figure 3-15 shows the current values for a 1000 × 1000 µm2 IrOx sensor. Similar to the Au sensor, the IrOx modified sensor showed corresponding stepwise increased currents with respect to the additions of lactate, and no response with respect to the additions of glutamate and dopamine.

Figure 3-15 (a) shows the response to lactate, Figure 3-15 (b) shows the response to glutamate and dopamine. The green line indicates the response of the working electrode. The blue line indicates the response of the self-reference electrode. The red line indicates the response of the calibrated result by the self-referencing technique.

From Figure 3-15 (a) we can see that the IrOx-based lactate sensor is responding to the additions of lactate with a step-increase. The current increase is higher than that of the Au-based electrode. From Figure 3-15 (b) we can see that the IrOx-based lactate sensor is not influenced by the glutamate, however it is influenced by the dopamine. After calibration, the calibrated result (subtraction) shows step-response to lactate additions only.
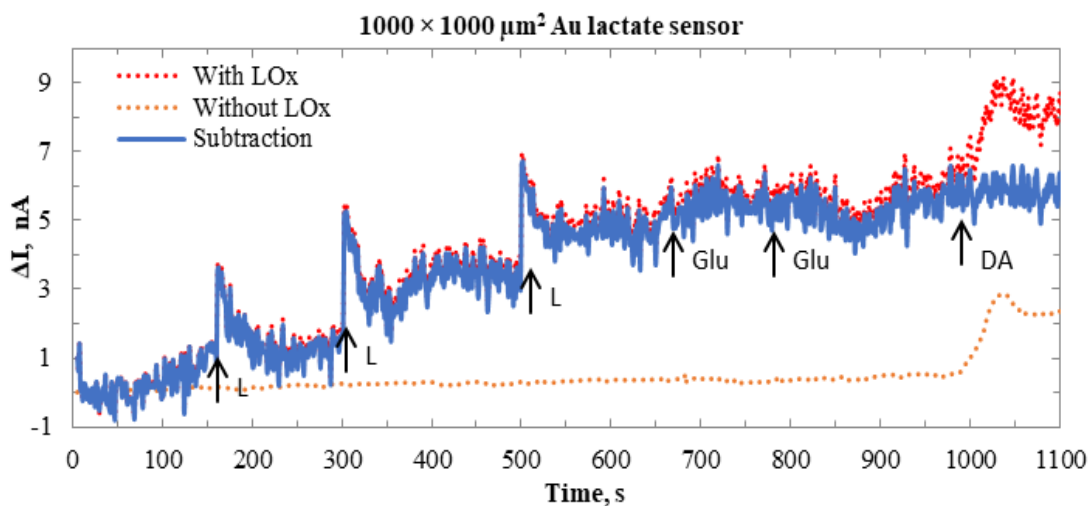
Figure 3- 13. Time-current plots for WE (with LO$_x$) and SE (without LO$_x$) in 1X PBS with responses to lactate, glutamate, and dopamine.
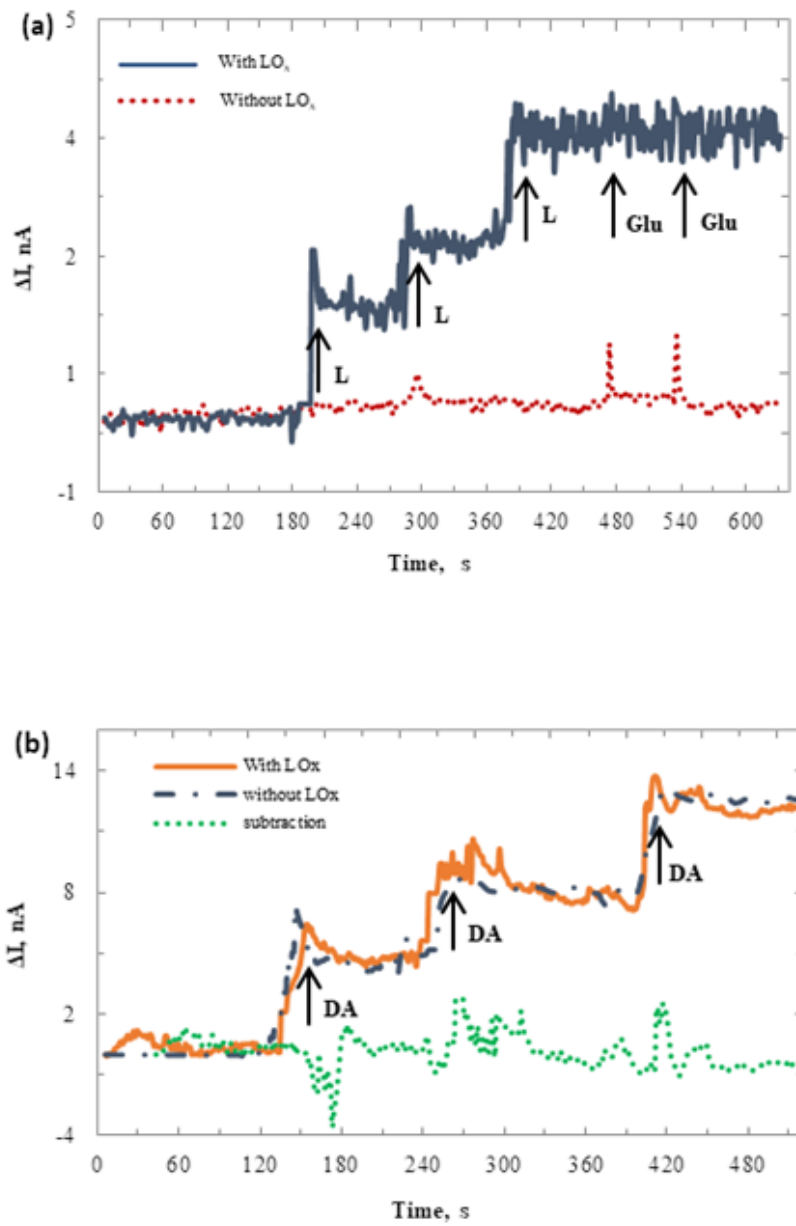
Figure 3- 14. Time-current plots for Au based WE (with LOx) and SE (without LOx) in 1X PBS with responses to (a) lactate and glutamate; (b) dopamine only.
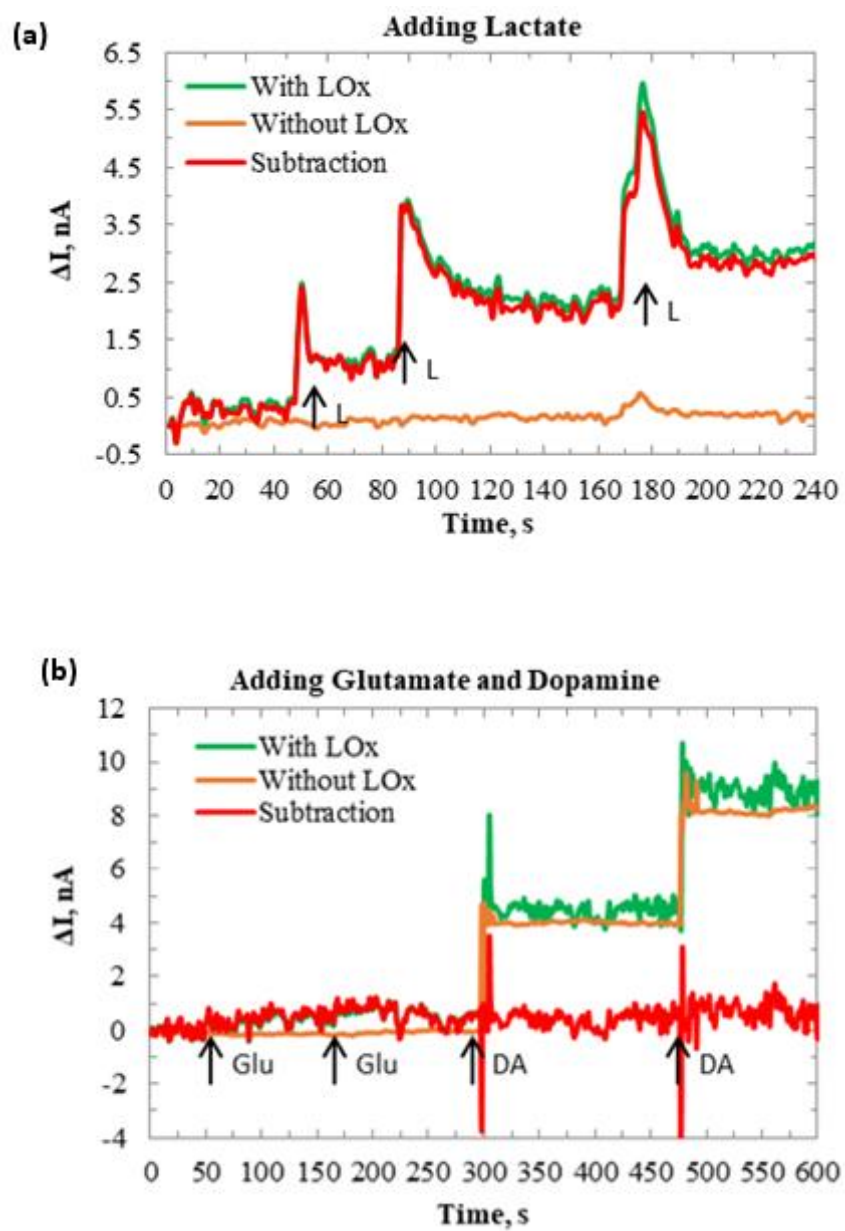
Figure 3- 15. Time-current plots for IrOx based WE (with LOx) and SE (without LOx) in 1X PBS with responses to (a) lactate; (b) glutamate and dopamine.

3.3.7. Study of Longevity

After a few days of uses, the Au sensor showed decayed performance. The sensor eventually stopped responding to lactate. This may be due to the loss of weakly-bonded enzymes, the inactivation of the enzyme, or the damage of the sensing film surface. To examine the electrode lifetime in a dry condition, the sensor was first tested in one beaker with 4 additions of lactate, and then sealed in a container for a week at the room temperature. The same experiment was conducted and repeated every week. In this case the sensor showed responses to lactate for 4 continuous weeks. At the 5th week, the sensor started to show a degraded response with less sensitivity. Scanning electron microscopy (SEM) was conducted to check the enzyme quantity and sensing surface quality before and after the sensor was used.

3.3.7.1. Scanning Electron Microscopy Analysis (SEM)

SEM analysis was conducted for both the Au-based and IrOx-based lactate sensor. Before usage, the quantity of the loaded enzyme was checked. After being used for three weeks and over a month, the quantity of the loaded enzyme was checked again respectively. The condition of the Au film and iridium oxide film were also checked before loaded with enzyme and after being used for 3 weeks and over a month. Figure 3-16 shows the SEM photos of the Au sensing film. Before loaded with enzyme, the Au film is flat. Figure 3-16 (b) shows the condition of the loaded enzyme before use. It clearly shows the protein crystals were evenly distributed on the film. After being used for 3 weeks, the quantity of the enzyme greatly reduced as shown in figure Figure 3-16 (c). After being used for over a month, the enzyme crystals were gone and bumpy Au surface was observed as shown in figure Figure 3-16 (d). This was likely that after several tests some of the protein particles were washed away by the buffer solution along with the attached Au film, which left micro-scale pores on the metal layer. The buffer solution leaked through the pores and went under the film to create the bumps. Thus, the sensing pad was damaged.

Figure 3-17 shows the SEM photos of the iridium oxide sensing film. Before loaded with enzyme, the IrOx film is flat. Figure 3-17 (b) shows the condition of the loaded enzyme before use. It clearly shows the quantity of the protein crystals were much more than that on the Au-film. The rougher surface of the IrOx makes more room for the enzymes to be loaded. After being used for 3 weeks, the quantity of the enzyme reduced as shown in Figure 3-17 (c), yet it still more enzymes were preserved than on the Au film. After being used for over a month, the enzyme crystals were gone but the surface was still flat as shown in Figure 3-17 (d). The rough surface of IrOx allowed better loading of enzyme and could possibly eliminate gas evolution from the reaction that caused metal corrosion.
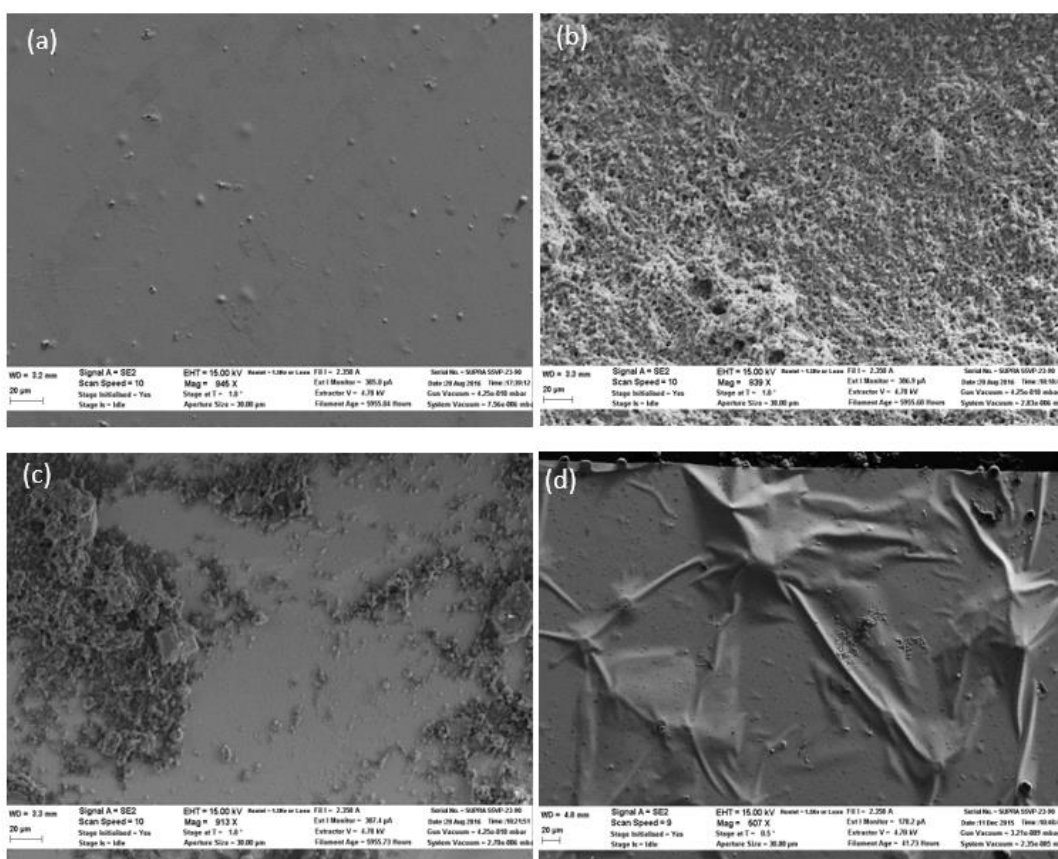
Figure 3- 16. SEM photos of the Au film (a) before and (b) after loaded with enzymes; and the Au-based sensor after being used for (c) 3 weeks and (d) over one month.
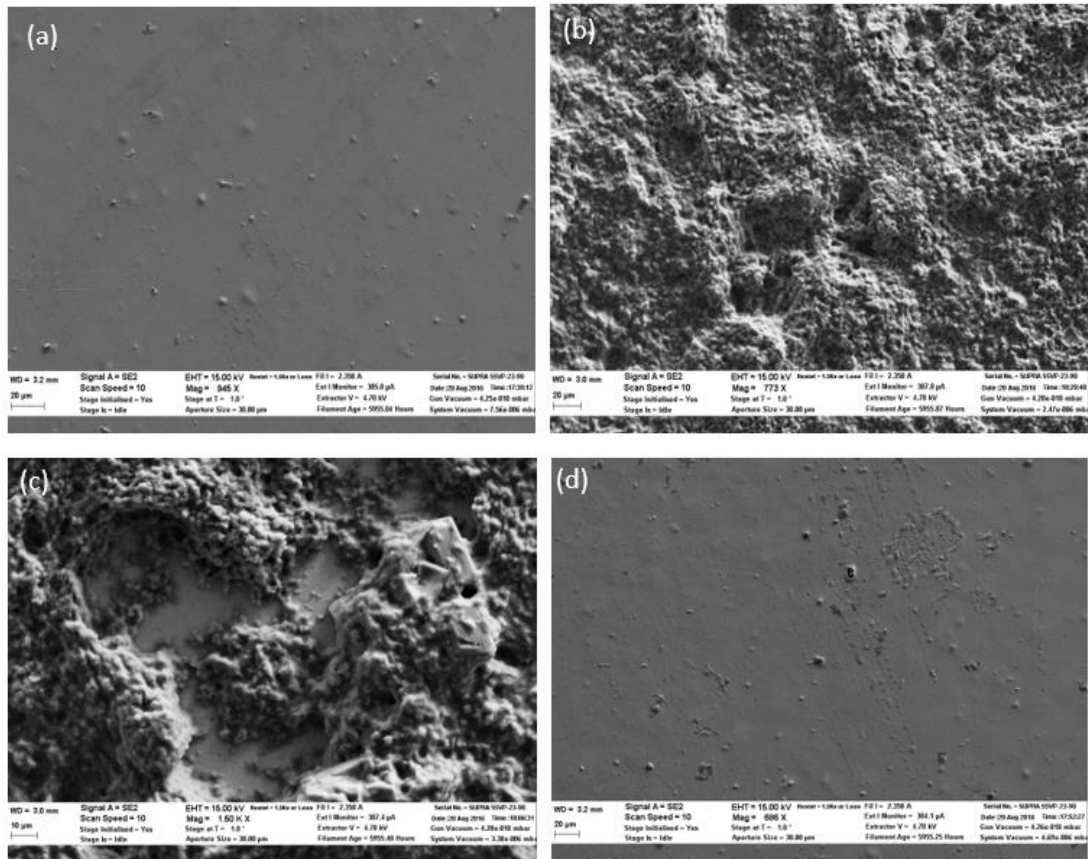
Figure 3- 17. SEM photo of the iridium oxide film (a) before loaded with enzymes; (b) after loaded with enzymes; (c) after being used for 3 weeks; and (d) after being used for over one month.

3.3.8. Study of Flexibility

The IrO_x lactate sensors are designed suitable for wearables and implants owing to the flexibility of the substrate. The sensitivity was tested on a 1000 × 1000 µm2 IrO_x sensor in flat and bent conditions. As shown in Figure 3-18(a), the polyimide substrate supporting the electrodes was bent with a curvature radius of 2 mm. A cotton wire was used to tie the probe shaft to keep the sensor in the bent condition. Figure 3-18 (b) shows the comparison between the sensor in the bent and flat conditions. The result demonstrated that the sensibility was not affected when the sensor was deformed to a curvature radius of 2 mm. A longer response time was observed during

experiments. This was likely due to that the sensing electrode was facing inwards in the bent probe; hence the applied lactate was not directly touching onto the electrode. Time for diffusion was needed before reaction occurred.
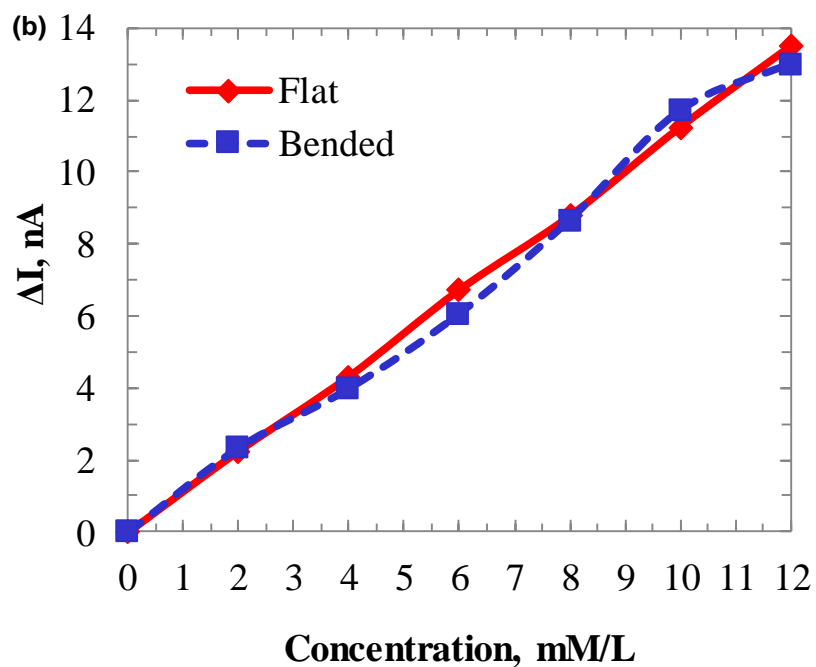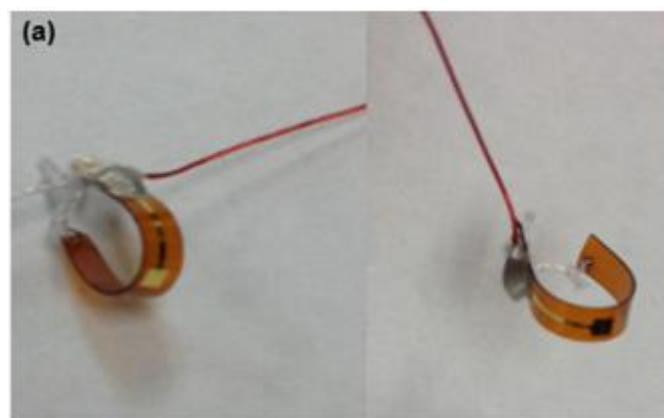
Figure 3- 18. (a) Photo of an electrode in deformed condition. (b) Sensitivity comparison between the IrO_x lactate sensor in the flat condition and when it was bent.

3.4. Conclusions

In this chapter, an iridium oxide based flexible lactate sensor was developed for the purpose of wearable or implantable sensing. Two types of the bio-compatible electrode: gold and IrOx, have been demonstrated and compared. Sensors with different sizes and materials were investigated for the sensitivity, selectivity, stability, and durability. The rough surface of IrOx provides a noticeable improvement in sensitivity comparing with the Au based sensor. The self-reference technique reduces the interference and noises, hence improved the selectivity. The simple fabrication method without high thermal budgets provides potentially cost-efficient sensors. The flexible polyimide substrate along with the IrOx being inert enable the device better biocompatibility for animal and human use. The good performance of the sensing electrodes and the simple fabrication method make affordable device possible for variety of practical applications. Disposable devices could be achieved for clinical medicine, food processing, athlete training and other lactate-detection related bio-applications.

3.5. Future Works

3.5.1. Utilization of IrOx Nanotubes

To further increase the sensitivity, we could use IrOx nanotubes instead of IrOx thin film to increase the surface area. A 550-µm thick p-type silicon wafer can be used as the substrate. First, the silicon wafer is cleaned with buffered HF solution. Then a 500-nm thick silicon dioxide layer is grown by a wet-thermal oxidation process as electrical insulation layer. Then, a layer of 2.2-µm thick NR-9 photoresist (Futurrex) is spin-coated and patterned to create the bases of microelectrodes and connection lines. The following metal deposition process included layers of aluminum, gold and titanium. Titanium and gold layers are deposited by electron beam evaporation with the thickness of 10-nm and 150-nm respectively. The aluminum layer is sputtered with the thickness of 900-nm. Then the sacrificial photoresist layer is removed by the lift-off process. Then, a thick SU-8 (MicroChem) is patterned as a passivation layer.

To grow the IrOx nanotubes, a supportive nano-porous aluminum oxide (AAO) template is needed. The AAO template is formed by the anodization process conducted with 0.23-M oxalic acid solution (Ricca Chemical). Then, the phosphoric acid 10 wt% solution (EM Science) is dripped onto the AAO template for a period of time to widen the pore size and remove the aluminum oxide barrier layer at the bottom. The IrOx is then anodically electrodeposited into the nano-porous structures. The sacrificial AAO template is dissolved in 0.1 M potassium hydroxide (EM Science) for 2 hours afterwards. Finally, the enzyme stock solution is dropped on the free-standing IrOx nanotubes and air dried.

3.5.2. Advanced Enzyme Bonding Method

To increase the stability of the enzyme on the sensing film, different banding methods can be applied to the sensor. Method 1 is using the cross-link material as shown in Figure 3-19 (a). The cross-link material is synthesized by dissolving 0.01 g of BSA into 1000 µL DI water. Manual agitation is needed to avoid foam. Then 5 µL of glutaraldehyde (Glut) is added to the mixture. Keep the mixture in still for 20 minutes until the link is formed inside the solution. Then
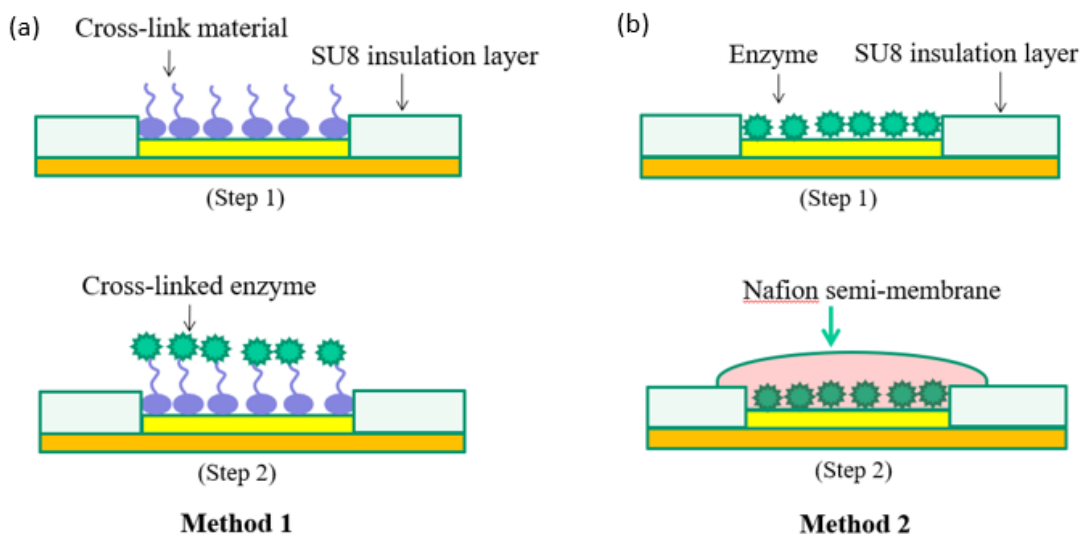
Figure 3- 19. Bonding methods of applying (a) cross-link material and (b) Nafion membrane to improve the enzyme stability.

transfer 10 µL of the BSA/Glut mixture and mix it with the alquoted 20 µL lactate oxidase stock

solution. The solution is genteelly agitated by pipette until completely mixed.

Method 2 is using Nafion solution as shown in Figure 3-19 (b). After coating enzyme on

the electrode, the probe is soaked in the Nafion solution and then heated at 65 °C for 5 minutes.

A Nafion semi-membrane is formed which allowed oxygen, ions and H2O to path through. The

disadvantage of using Nafion is that it is fragile and could be peeled off from the probe, which

decreases the deformability.

3.5.3. Development of a Multi-Functional Sensing System

To further functionalize the sensor, we design the multi-functional sensor array. Several

electrodes with different functions are fabricated on one probe. This probe will not only be lactate

sensitive, but also be glucose and dopamine sensitive. The embedded IrOx electrode served as

the self-reference electrode.

First, we pattern gold on the flexible substrate and fabricate the IrOx reference electrode.

As described before, the negative photoresist SU8-100 is spin-coated on the gold film as mask,

leaving only one opening window for sol-gel deposition. After dip coating and heat drying, the

photoresist layer is peeled off. The following thermal treatment process formed the IrOx film only
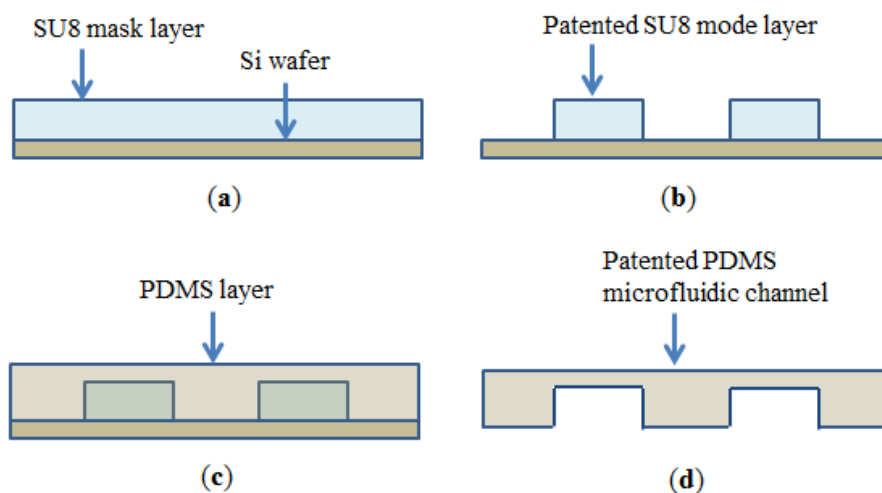
Figure 3- 20. Fabrication procedures of the PDMS microfluidic channel

on the desired electrode. The negative photoresist SU8-25 is then patterned on the film as insulation layer. The cooper wire is connected with the connection points by silver epoxy as described before.

The next step is electrodes functionalization. Here we use the microfluidic channel to coat enzymes. Figure 3-20 (a) to (d) shows the steps to form a PDMS microfluidic channel. First SU8-100 is spin-coated on a silicon wafer and then patterned. The patterned SU8 layer served as the mode for the PDMS layer. The thickness of the SU8 determines the height of the microfluidic channel. Here 200 μm is desired. The film is stick on the bottom of a culture plate and the PDMS liquid is poured into the culture plate. The volume of PDMS liquid is calculated a head of time to control the thickness of the cured PDMS layer. After heating up and standing for 24 hours, the PDMS layer is cured and could be peeled off from the mode.

Then the PDMS microfluidic channel is placed on top of the probe as shown in Figure 3-21 (a). The wells of the PDMS are aligned with the desired electrodes. The enzyme stock solutions are injected through the microfluidic channels and stocked in the wells on top of the electrodes as shown in Figure 3-21 (b).
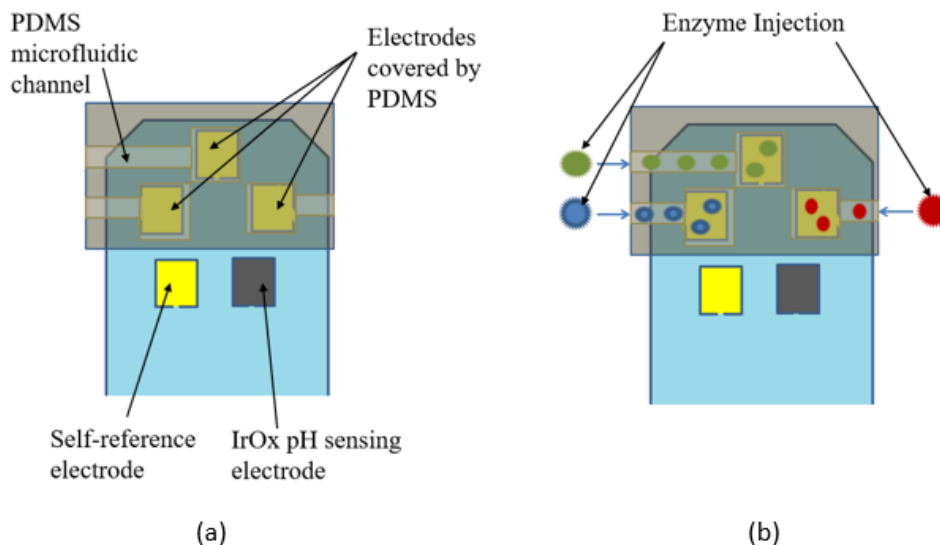
Figure 3- 21. Illustrations of (a) the PDMS microfluidic channel on top of the electrodes and (b) the enzyme injection process.

The surface tension of PDMS and photoresist makes them stick together which avoid liquid leakage. Hence different enzyme solutions stayed in the wells independently without mixture and contamination. This made it possible to reduce the distance between each electrode, therefore reduce the size of the probe. Through controlling the thickness and size of the SU8 layer, we could control the volume of the PDMS wells, which quantified the quantity of enzymes applied each time. The PDMS layer is placed on the substrate until the enzyme solution is completely dried and then peeled off. This could take a while since the enzymes are sealed in the PDMS wells. Low temperature heating is preferred to accelerate the moisture evaporation. The applied heat should be kept bellow 45 °C to maintain the enzyme activity. The cross-link material or Nafion solution could also be used here to increase the stability of the enzymes as described before. The multi-function sensing system will be targeted at multi-biomarkers detection.

Chapter 4

IRIDIUM OXIDE BASED SENSOR FOR pH SENSING

4.1. Introduction

Nowadays, pH measurements have been widely applied in chemical laboratories and factories, pharmaceutical industries, produce processes and agricultures. Since many biological and chemical reactions are pH dependent, measuring pH variances can give insights about the processing and status. Hence, a responsive pH sensor adaptable to various mechanical environments is desired. Conventional glass-rod pH sensor, although provides superb performance, has disadvantages in its bulky configuration, which makes it unsuitable for in-vivo or in-situ biomedical and food monitoring in real time. [4.1]

Therefore, certain types of pH sensors with smaller sizes have been reported, including optical fiber pH sensors [2], hydrogel pH sensors, and ion-sensitive field effect transistor (iSFET) pH sensors. Many of them have been used in commercial applications. However, in specific applications that require high deformability or conformability, passive sensing and wireless signal transmission, the aforementioned pH sensors still have technical limitations. During operation, optical fiber pH sensor and iSFET require external power supplies making it difficult for passive sensing [4.2]. The fabrication procedures of the hydrogel film pH sensors could be complex and costly as they require polymers that may not be reliable for a wide range of environments [4.3].

The solid-state metal-oxide pH sensor could be a solution to this type of technical challenges. It has the advantage of mechanical strength and electrochemical stability [4.4]. Moreover, the metal-oxide sensing film can be integrated passively with electrical circuit for signal transduction. The fabrication procedures can be cost effective and simple. In our previous works, we have demonstrated pH sensors based on iridium oxide (IrOx) sensing film [4.5] by inexpensive processes of sol-gel coating and thermal oxidation on flexible polyimide substrates. The pH sensor showed satisfied performance and reliability.

In this chapter, we further conducted the in-depth study of the performance of the iridium oxide pH sensor. We investigated several factors which could influence the performance of the pH sensor. Different deposition techniques to prepare the iridium oxide sensing film have been tried and evaluated. The influence of the materials for the metal substrate have been investigated. Various pH sensors have been made with different metal substrates, including nickel, aluminum, and gold. Various adhesion layers were applied to these metals respectively to improve the adhesiveness. Scanning electron microscopy analysis and electron dispersive analysis were conducted to evaluate the physical condition of the metal substrate and the quality of the iridium oxide sensing film on top. The sensors made by different types of metal substrate were tested for sensitivity and repeatability to evaluate the performance. The silver/ silver chloride reference electrode has also been investigated. In our previously study, a commercial silver/ silver chloride reference electrode was used to guarantee the performance of the pH sensor. Here, we proposed a flexible silver/ silver chloride reference electrode with the same size of the iridium oxide working electrode. Different fabrication techniques were used to fabricate the silver/ silver chloride electrode, including the electroplating technique and the printing technique. The silver/ silver chloride electrodes were tests against one iridium oxide working electrode to evaluate the performance.

The hysteresis error was investigated. Hysteresis error commonly exist in the field of pH sensing yet there is no answer to solve this problem. In this chapter, we investigated the adempts to reduce the hysteresis error. The pH sensors with different substrate metals and different sizes were fabricated and tested. The pH measurements were also conducted with different testing sequences. The hysteresis error has been minimized and the optimum performance of the pH sensor has been achieved the.

Another commonly existing pH sensing error is the interference effect. Since the pH measurement is usually conducted in the environment with the existence of various of metal ions, the interference effect is not neglectable. In this chapter, we investigated the interference error

generated by two commonly exist metal ions: potassium ion and sodium ion. The pH mismatch generated by different concentrations of the two types of ions was investigated. Knowing the interference effect of the pH sensor gives us the opportunity to calibrate the pH sensor before use, hence an accurate pH measurement can be achieved.

Other than the aforementioned attempts to improve the sensor performance, comparing with our previous work, the fabrication procedures of the pH sensor have been simplified and the flexibility of the pH sensor has been improved. The accuracy and stability of the pH sensor have also been greatly improved.

4.2. pH Sensing Mechanism of Iridium Oxide

Three are five possible pH sensing mechanisms for the metal oxides, as described below:

- Similar as the glass electrode, the ion exchange process happening on the sensing film which contains the OH^- group.

- The redox equilibrium generated between the two different solid phases. Such as in between of the lower and higher valence of an oxide, or in between of a pure metal phase and its oxide phase.

- The solid intercalation reaction. By passing through a current on the metal electrode, the hydrogen content in the testing solution varied continuously.

- Similar as the solid intercalation reaction, an interaction involving oxygen could be described.

- A steady state corrosion of the metal electrode can also create a pH dependent potential.

The sensing film of the iridium oxide pH sensor contains two oxidation states of the iridium oxide. When the H^- ions are introduced, the pH dependent redox equilibrium between the two oxidation states could be described in three possible mechanisms [4.6], as described in the following three equations:

$$Ir_2O_3 + 6H^+ + 6e^- \leftrightarrow 2Ir + 3H_2O \qquad (1)$$

$$IrO_2 + 4H^+ + 4e^- \leftrightarrow Ir + 2H_2O \qquad (2)$$

$$2IrO_2 + 2H^+ + 2e^- \leftrightarrow Ir_2O_3 + H_2O \qquad (3)$$
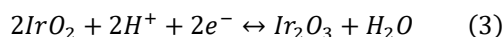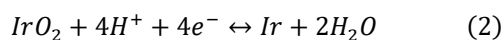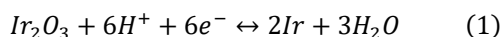
The potential generated between the working electrode and the reference electrode is given by the Nernst equation, as described below:

$$E = E^0 - 2.303 \frac{RT}{F} pH = E^0 \pm 0.05916\, pH \qquad (4)$$

Here, E^0 is the standard electrode potential, which depends on the choice of the reference electrode. In our study we use the silver chloride electrode as the reference and the standard electrode potential is 577 mV. F is the faraday's constant, which is $96487\ ^C/_{eq}$. R is the gas constant, which is $8.314\ ^J/_{deg}$. The experiments are conducted at the room temperature which is controlled at 25°C, which result the value of $\frac{RT}{F}$ around 25.69. Ideally, the Nernst response will result in a pH potential sensitivity of $-|-59|\ ^{mV}/_{pH}$ [4.7-4.9].

There are several factors which will affect the theoretical value of the pH potential. For instance, E^0 varies for different electrodes because of the variation in the stoichiometry of the oxide compound and the difference of the oxidation state of the iridium oxide [4.7]. The pH response could also be influenced by the ion exchange which happens on the surface containing OH⁻ groups [4.10]. The equilibrium for the proton exchange is described below [4.11]:

$$[-Ir^{IV} - (OH)_x - Ir^{IV} -]_n + 2ne^- + 3nH^+ \leftrightarrow [-Ir^{III} - (OH)_{x-3} \cdot 3H_2O - -Ir^{III} -]_n \qquad (5)$$

$$Ir_2O(OH)_3O^{3-}{}_3 + 3H^+ + 2e^- \leftrightarrow 2Ir(OH)_2O^- + H_2O \qquad (6)$$
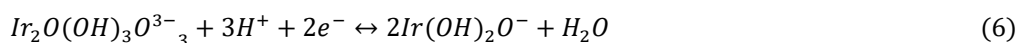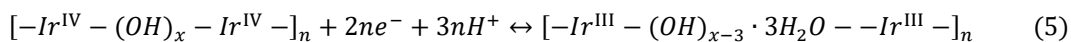
Equation (6) indicates the theoretical possibility of the sensitivity could be higher than $|-59|\ ^{mV}/_{pH}$, which is demonstrated in our experiments.

4.3. Performance of the pH Sensor with Different Iridium Oxide Deposition Techniques

The fabrication techniques of the iridium oxide involving sputtering deposition, thermal oxidation, sol-gel deposition, electrochemical deposition, and electro-deposition. As described in Chapter 2, the sputtering deposition technique provides a distinctive rutile pattern, however the

fabrication process is time consuming and costly; the thermal oxidation technique provides a thick sensing film, however a high process temperature is required; the sol-gel deposition technique has the advantage of cost effectiveness and simple fabrication process; the electrochemical deposition technique provides the iridium oxide film with unique porous structure, which makes it suitable to transport water, protons and other ions, however the applied potentials and current need to be controlled precisely during fabrication; the electro-deposition technique is cost effective, however the crystalline structure of the iridium oxide is not as good.

Our goal is to achieve a pH sensor suitable for bio-applications. According to the needs, we are looking for a disposable pH sensor with good conformity to the testing surface such as skin. The pH sensor should have the physical properties such as flexible, low costs, simple fabrication processes, and reliable device performance. To achieve these goals, we fabricate our pH sensor on a flexible polymer substrate. According to the requirement of the polymer substrate a low process temperature is preferred. Among the above-mentioned fabrication techniques, the sol-gel deposition and electro-deposition have a low process temperature, which is suitable for our purpose. These two fabrication techniques also have the advantages of low cost and easy to operate. In addition, the quality of the outcoming iridium oxide sensing film is controllable. In this section, an in-depth study is conducted to compare these two fabrication techniques. pH sensors with the same configuration are fabricated with these two deposition techniques and tested respectively. The performance of the pH sensors fabricated by these two deposition techniques are evaluated and compared.

4.3.1. Sol-Gel Deposition Technique

4.3.1.1. Coating Agent

First, one gram of the anhydrous iridium chloride (IrCl4) is dissolved in 42 ml ethanol (C2H5OH). Then, 10 ml of the 80% acetic acid (CH3COOH) is added to the mixture [4.12]. The solution is stirred constantly with a magnetic rod for 2 hours before use. The storage temperature for the solution is 4 °C. The purpose of adding the acetic acid is to maintain the solution at a low pH level to avoid chemical reaction which could happen during the mixing procedure. The dip-coating process is conducted after the solution is prepared.

4.3.1.2. Dip-Coating Process

The dip-coating process is suitable for the agents with high evaporation property. It contains 5 steps: immersion, start-up, deposition, drainage, and evaporation, as described in Figure 4-1 [4.16]. The thickness of the deposited film depends on the withdraw angle and rate. We prefer thicker film since it has higher charge density. Based on our previous study, a withdraw rate of 10 centimeter per minute is desired [4.17].

In this section, the sol-gel deposition is conducted on a sensor probe fabricated on a 125-μm thick flexible polyimide film with 200-nm thick gold. A 50-nm thick chromium is used as the adhesion layer for gold. The electrode is patterned by laser cutting with the size of $1 \times 10 \; mm^2$.

4.3.1.3. Annealing Process

After the electrode is coated with the sol-gel solution, a sequence of thermal treatment is conducted. It starts with the soft-bake. First, the electrode is placed on a hot plate set at 75°C for 20 minutes to remove the moisture. Then, the electrode is removed from the hot plate and cooled down to the room temperature. Afterwards, a thermal treatment was conducted to oxidize the iridium chloride with a heating profile from 25°C to 325°C in a 3-hours period. Then the temperature was maintained at 325°C for 4 hours. Finally, the electrode is cooled down in a 7-hours period. Here, we set the oxidation temperature at 325°C instead of a higher temperature to avoid cracks formed on the iridium oxide film. The cracks deteriorate the performance of the

sensor as discussed in the previous section. The chemical reaction took place in the thermal oxidation process is described below:

$$2IrCl_4 + 3H_2O \xrightarrow{300\ °C} Ir_2O_3 + 6HCl + Cl_2 \qquad (7)$$
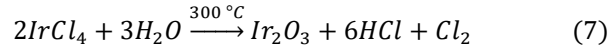
4.3.2.Electro-Chemical Deposition Technique

4.3.2.1. Coating Agent

The soluble iridium precursor is prepared by dissolving 0.075 g powder of the 99.9% $IrCl_4 \cdot H_2O$ into 40 ml DI water. The solution is stirred by a magnetic rod for 30 minutes. Then, 0.5 ml of the 30% H_2O_2 and 10 ml of the $H_2C_2O_4 \cdot 2H_2O$ are added to the mixture and the solution is stirred for another 10 minutes. The color of the solution will change from dark purple to light yellow-green once the solution is successfully made. At this stage the pH level of the solution is around pH 1.5. Finally, K_2CO_3 powder is added to the solution to adjust the pH level to the pH10.5. The solution is rest for 4 days before use.
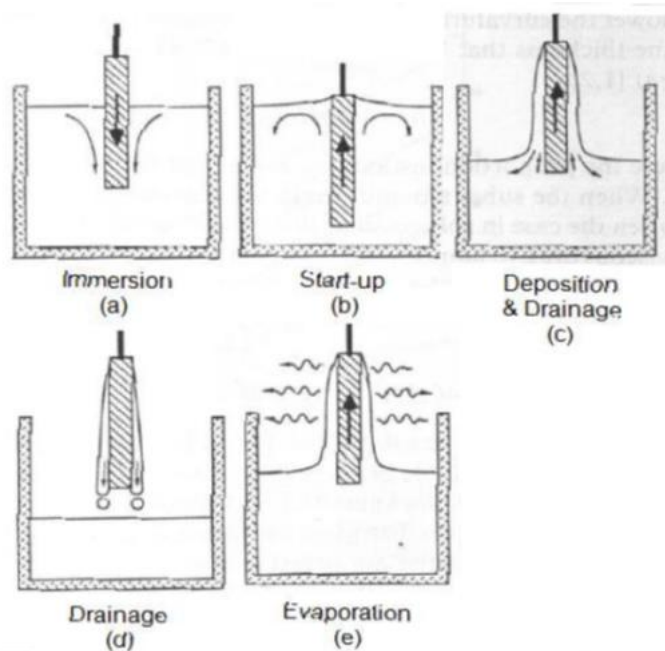
Figure 4- 1. (a) - (e): Five stages of the dip coating process [4.18].

4.3.2.2. Electroplating Process

Same as for the sol-gel process, the electroplating deposition is conducted on a sensor probe fabricated on a 125-μm thick flexible polyimide film with 200-nm thick gold. A 50-nm thick chromium is used as the adhesion layer for gold. The electrode is patterned by laser cutting with the size of $1 \times 10 \ mm^2$.

A potentiostat (Model 700E, CH Instruments) is used for the cyclic voltammetry deposition. A commercial Ag/AgCl electrode (MW-2021, Bioanalytical Systems Inc.) and a platinum (Pt) wire counter electrode are deployed to perform the CV process. The coating parameters are 50 mV/s ramps between $-0.8 \ V$ - $0.7 \ V$ for 100-200 cycles.

The set-up of the electrodeposition [4.19] and the CV process is shown in Figure 4-2. The deposition current output shown in Figure 4-2 (b) was obtained from a single $1 \times 10 \ mm^2$ Au electrode which was deposited for 150 cycles. The increasing output current indicates the growth of the IrOx film thickness. The current density reaches its peak value in the range of $55 - (-88) \ mA/_{mm^2}$.
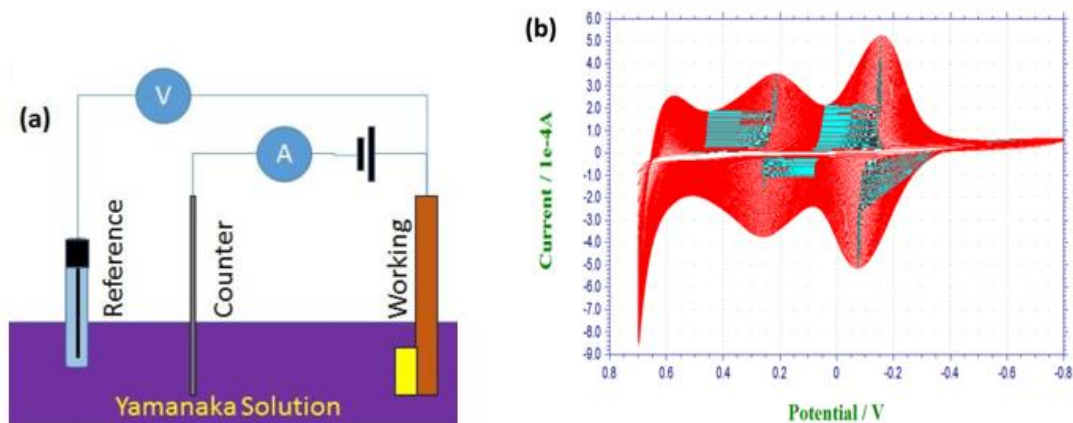
Figure 4- 2. (a) Electrodeposition setup [4.21]. (b) The CV process output obtained from our experiment.

4.3.3. Measurement Results and Discussions

The pH sensor consists of two electrodes: the iridium oxide working electrode and the silver chloride reference electrode. The pH value is indicated by the potential difference generated between the working and reference electrodes. The iridium oxide working electrodes are made by the sol-gel deposition or the electrodeposition. The silver chloride reference electrode is made by printing the AgCl paste. Both the working and reference electrodes were made on a flexible polyimide film and patterned by laser cutting. Electrical wires were attached to the working and reference electrode stripes by silver epoxy. Standard buffer solutions (pH= 4, 7, and 10) were used for testing. A data acquisition (NI DAQ-609) card was used for measurements of the potential difference between the working and reference electrodes. A LabVIEW-based program was used to record the real-time potentials with the sampling rate of 7.5 samples per second. The iridium oxide electrodes fabricated by the two deposition techniques are tested and compared for the major pH sensing parameters: sensitivity, hysteresis, reversibility, and lifetime.

Figure 4-3 shows the performance of the electrode prepared by the sol-gel deposition. Three electrodes were tested to demonstrate the consistency of the pH sensor. The sensors are tested in the order of pH = 4 to 10 first. The sensitivity is in the range of $54.6 \, {mV}/{pH}$ to $56.9 \, {mV}/{pH}$. The average sensitivity is $55.57 \, {mV}/{pH}$. The electrodes show a highly Nernstian response with an R2 value of around 0.9981. Then the test is repeated with the reversed order from pH = 10 to 4. The average sensitivity is $51.36 \, {mV}/{pH}$. The pH response is fast and consistent, with an R2 value of around 0.9917. The average hysteresis value is 16.4 mV. The general lifetime of the sol-gel deposited pH sensor is 3 months.

Various sweeping cycles (50, 100, 150, and 200 cycles) have been tried to deposit the iridium oxide films. The electrodes with different sweeping cycles are tested to compare the performance. By increasing the sweeping cycles, the thickness of the iridium oxide film increases [4.20]. Elsen mentioned that the thickness changes the life time of the probe [4.21]. We also

demonstrated that with thicker iridium oxide film, the electrode last longer. However, the trade-off is that the sensitivity decreases and the hysteresis error increases when the sweeping cycle increases. The performance related parameters of the electrodes deposited with different sweeping cycles is shown in Table 4-1.

The sensitivity and reversibility of the electrode with 100 sweeping cycles is shown in Figure 4-4. The electrode is tested in the order of pH = 4 to 10 first. The sensitivity is $62.1\ ^{mV}/_{pH}$. The electrode shows a highly Nernstian response with an R2 value of 0.9996. Then the test is repeated with the reversed order from pH = 10 to 4. The sensitivity is $60.7\ ^{mV}/_{pH}$. The pH
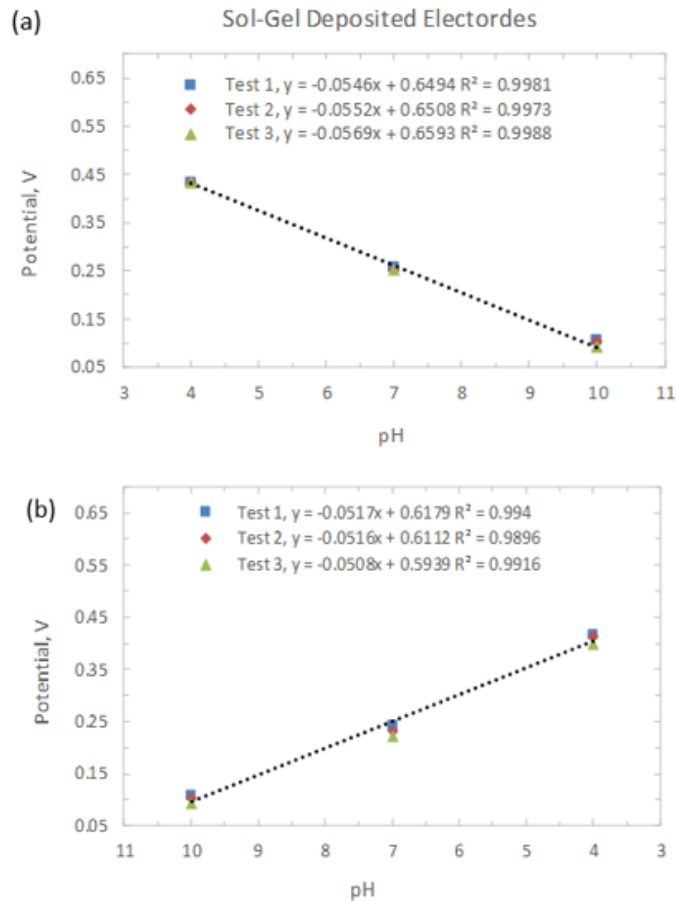
Figure 4- 3. The pH sensitivity of the IrOx thin film deposited by the sol-gel technique tested from (a) pH = 4 to 10, and (b) pH= pH = 10 to 4 buffer solutions.

response is fast and consistent, with an R2 value of around 0.999. The average hysteresis error

is 7.7 mV.

Table 4- 1. The performance of the electrodes deposited with different sweeping cycles.

	Sensitivity	Hysteresis	Lifetime
50 Sweeping Cycles	66.7 mV/pH	45.92 mV	1 week
100 Sweeping Cycles	62.1 mV/pH	7.7 mV	2-3 weeks
150 Sweeping Cycles	66.4 mV/pH	21.4 mV	1 month
200 Sweeping Cycles	51.2 mV/pH	19.65 mV	1.5 months
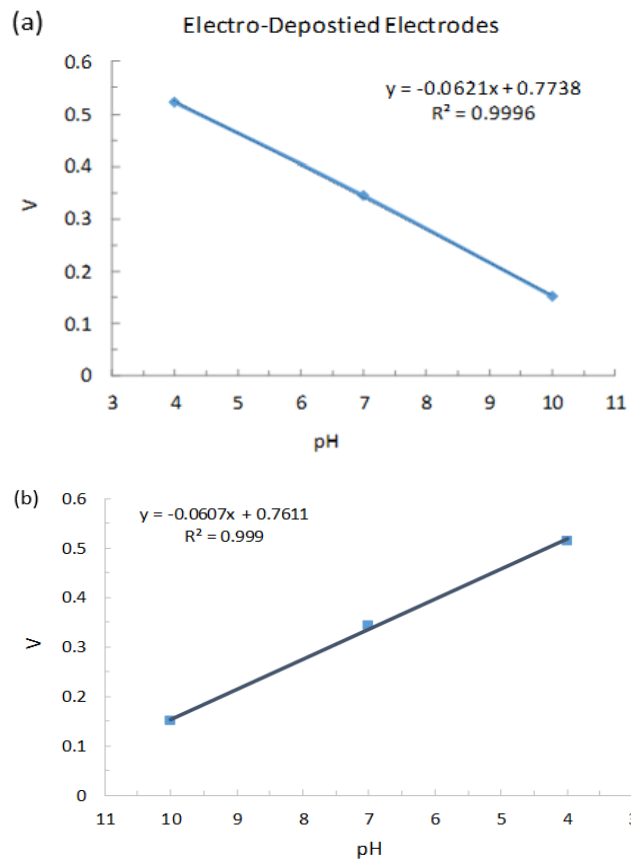
Figure 4- 4. The pH sensitivity of the IrOx thin film deposited by the electrodeposition technique tested from (a) pH = 4 to 10, and (b) pH= pH = 10 to 4 buffer solutions.

50

Over all, the electrodeposited iridium oxide pH sensor shows higher sensitivity comparing with the so-gel deposited ones. However, the lifetime of the so-gel deposited electrode is much longer than the electrodeposited ones. Comparing the two deposition techniques, more parameters need to be controlled for the electrodeposition process in order to achieve better performance, such as the solution temperature, solution pH level, applied potential range, number of sweeping cycles, and the condition of the substrate material. To better serve our goal of fabricating low-cost and reliable pH sensor for bio-applications, we choose to apply the sol-gel technique to fabricate the pH sensors due to the simple fabrication process and the durable electrode performance. The pH sensors used in Chapter 5 are all made by the sol-gel technique.

4.4. Performance of the pH Sensor with Different Metal Substrates

Au is the most commonly used metal for pH sensing applications owing to its unique property as a noble metal. Au is stable and rarely reacts with the reagents in the testing solutions. It is also resistive to highly acidic and alkaline solutions, which makes it superior material for pH sensor fabrication. With an adhesion layer of chrome, Au can be easily deposit on a flexible polyimide substrate with excellent durability [4.22]. A sensitivity of 77 mV/pH has been reported for the Cr-Au based pH sensor on a flexible substrate with iridium oxide as the sensing film [4.23].

Platinum has been used to fabricate the pH sensor with iridium oxide as the sensing film [4.24, 4.25]. The pH sensor is fabricated on a rigid glass substrate with a thin film of Ti as the adhesion layer. A sensitivity of 77.6 mV/pH is reported. However, when platinum is used to fabricate the pH sensor on a flexible substrate the sensitivity decreases [4.26]. As discussed in the previous section, the Nernst response is affected by the formation of the iridium oxide film, which is influenced by the condition of the metal substrate.

Etched metal substrates have been investigated to fabricate the pH sensor with iridium oxide as the sensing film, including titanium, silver, copper, nickel, and so on [4.27]. A good sensitivity of around 73 mV/pH is reported. However, there is no experiments to support that the etched metal substrates are suitable for flexible device fabrication which requires a metallic thin

51

film on the flexible substrate. The iridium oxide formation is likely to change for the metallic thin film, which affects the sensitivity.

Other materials used for pH sensors based on iridium oxide are reviewed by Kakooei [4.28], including tin-doped indium oxide (ITO), wolfram, zirconium, cobalt, stainless steel, and tin dioxide coated glass. The sensitivity of these sensors is in the range of 68 to 75 mV/pH [4.28]. Various fabrication techniques have been used and the fabrication process is complicated and costly.

Nowadays, disposable devices are desired in most of the cases for the bio-medical applications. Hence, minimizing the cost of the pH sensor is a practical attempt. To achieve our goal of pH sensing for biomedical applications, we need to reduce the fabrication cost yet maintain the performance of the pH sensor. Hence, we propose to use low-cost metals instead of gold to fabricate the pH sensor with the simple sol-gel technique. The electrodes are fabricated on the flexible substrate.

In this section, pH sensors with identical configuration are fabricated with nickel and aluminum. Different adhesion layers are used for the given metal to achieve reliable performance. The effectiveness of the pH sensors is evaluated. The quality of the iridium oxide sensing film formed on top of the metal film is checked by the scanning electron microscopy (SEM) analysis and electron dispersive analysis (EDAX). The pH sensors are tested with standard pH buffer solutions to investigate the sensitivity, reversibility, and repeatability.

4.4.1. Ni-based Electrode

4.4.1.1. Fabrication Process

The Fabrication process of the Ni-based electrode is shown in Figure 4-5. First, A 125-micron thick Kapton film is cleaned with acetone and alcohol. Then, a layer of photoresist is spin on the Kapton film and patterned to form the sacrificial layer for metal deposition as shown in Figure 4-5 (a). To deposit the Ni film, Ni pellets with a purity of 99.95 % is used. The Ni is deposited through the e-beam evaporation at a deposition rate of $1 - 1.5\,\text{Å}/s$. The thickness of the Ni film

is 200 nm. The deposited Ni on the substrate and photoresist is shown in Figure 4-5 (b). After Ni

deposition, the photoresist sacrificial layer is removed by acetone. The Ni electrode is achieved.

Then, a layer of SU-8-100 photoresist is coated on the film as the sacrificial layer for the sol-gel

process as shown in Figure 4-5 (c). After dip-coating, the film is slightly heated on a hot plate to

remove the moisture. Then the SU-8-100 sacrificial layer is peeled off. A thermal treat is

conducted on the Ni electrode with the sol-gel solution to form the iridium oxide sensing film as

shown in Figure 4-5 (d). Finally, a layer of SU-8-5 photoresist is patterned on the electrode as the

insulation layer as shown in Figure 4-5 (e). The sideview of the completed electrode is shown in

Figure 4-5 (e) and the top view of the electrode is shown in Figure 4-5 (f). The dish line indicates

the metal underneath the SU-8-5 insulation layer.

Figure 4- 5. Illustration of the (a) photolithography process; (b) metal deposition process; (c) and (d) sol-gel deposition process. (e) shows the sideview of the electrode. (f) shows the top view of the elctrode.

Besides the pure Ni electrode, we also fabricated electrodes with chromium and titanium as the adhesion layer. The fabrication process for the Ni electrodes with adhesion layers are pretty much the same as described above, except for the metal deposition process. For the Ni electrode with chromium adhesion layer (Cr-Ni electrode), during the metal deposition process a thin layer of Cr (50 nm) is deposited on the Kapton film through e-beam deposition, following by the deposition of 200 nm Ni. For the Ni electrode with titanium adhesion layer (Ti-Ni electrode), during the metal deposition process a thin layer of Ti (50 nm) is deposited on the Kapton film through e-beam deposition, following by the deposition of 200 nm Ni. The deposition rate is $1 - 1.5 \, \text{Å}/s$.

4.4.1.2. Scanning Electron Microscopy Analysis

SEM analysis is conducted to check the condition of the iridium oxide sensing film and the quality of the nickel-based metal films. The analysis is first conducted on the electrode before use to check the initial condition. Then the analysis is conducted on the electrodes being tested with moderate acidic and alkaline buffer solutions (pH 4 and 10) and highly acidic and alkaline buffer solutions (pH 2 and 12) to evaluate the anti-corrosion ability. The results of the SEM analysis are shown in Figure 4-6.

From the SEM images we can see cracks on the Ni based films with or without adhesion layer, especially for the Ni and Ti-Ni electrodes. The sensing film is rough on the edge of the electrode. The cracks are formed during the sol-gel deposition process. Due to the pour adhesiveness of the e-beam deposited Ni on the Kapton film, during the sol-gel process the acidic solution affects the smoothness of the Ni film and further influenced the formation of the iridium oxide film. Adding the adhesion layer of Ti the adhesiveness between the metal and the polyamide substrate improved, thus the deposited IrOx film becomes smoother. With the Cr adhesion layer, the surface uniformity is much better. This is likely because the linear temperature expansion coefficient of Cr ($(6-7) \cdot 10^{-6} \, {}^m/_{mK}$)) is closer to the temperature expansion coefficient of iridium ($6.4 \cdot 10^{-6} \, {}^m/_{mK}$)) than that of Ti ($8.5-9) \cdot 10^{-6} \, {}^m/_{mK}$) and Ni

$(13.0 \cdot 10^{-6} \, {}^{m}/_{mK})$. With the close temperature expansion coefficient, the iridium oxide forms with better crystalline structure during the thermal oxidation process. With better iridium oxide film, the condition of the electrode is not likely to be affected by the acidic or alkaline pH buffer solutions.

From Figure 4-6 (b) and (e) we can see that the part of the sensing surface of the Ni and Ti-Ni electrode with cracks got eroded or etched away after tested with pH 4 and 10 buffer solutions. After tested with stronger acidic or alkaline pH buffer solutions this phenomenon is even severer as shown in Figure 4-6 (c) and (f). However, for the Ni electrode with Cr adhesion layer, the IrOx film is not affected by the moderate acidic or alkaline pH buffer solutions as shown in

Figure 4- 6. SEM images of the (a) Ni electrode before use and (b) Ni electrode tested with pH 4 and 10 buffer solutions and (c) Ni electrode tested with pH 2 and 12 buffer solutions; (d) Ti-Ni electrode before use and (e) Ti-Ni electrode tested with pH 4 and 10 buffer solutions and (f) Ti-Ni electrode tested with pH 2 and 12 buffer solutions; (g) Cr-Ni electrode before use and (h) Cr-Ni electrode tested with pH 4 and 10 buffer solutions and (i) Cr-Ni electrode tested with pH 2 and 12 buffer solutions.

Figure 4-6 (h). After tested with strong acidic or alkaline pH buffer solutions the surface becomes less smooth, yet the sensing surface is not eroded or etched away. Hence adding the adhesion layer of Cr the durability of the Ni electrode could be improved in the acidic or alkaline testing environment. Due to the damage of the iridium oxide sensing film in the strong acidic or alkaline pH buffer solutions, the pH sensor made with Ni-based materials are tested in the range of pH 4-7 in the next section.

4.4.1.3. Electron Dispersive Analysis (EDAX)

To investigate the quantity of the iridium oxide film deposited on top of the Ni-based electrodes after sol-gel deposition, we conducted the energy dispersive X-ray spectroscopy to check the surface composition of the sensing area. The samples are checked with the EDAX 4000 system in a Zeiss Supra 55 VP scanning electron microscope system. The EDAX analysis result of the iridium oxide film on the Cr-Ni electrode is shown in Figure 4-7. Except for the peaks indicating Ni, Cr, and Ir, some small amounts of elements detected were probably due to the contamination from the solution and the device carrier under the sensor in the SEM chamber. The proportion of the iridium oxide on the electrode before use and after being used in moderate and strong acidic or alkaline pH buffer solutions are shown in Table 4-2. After being used in pH 4
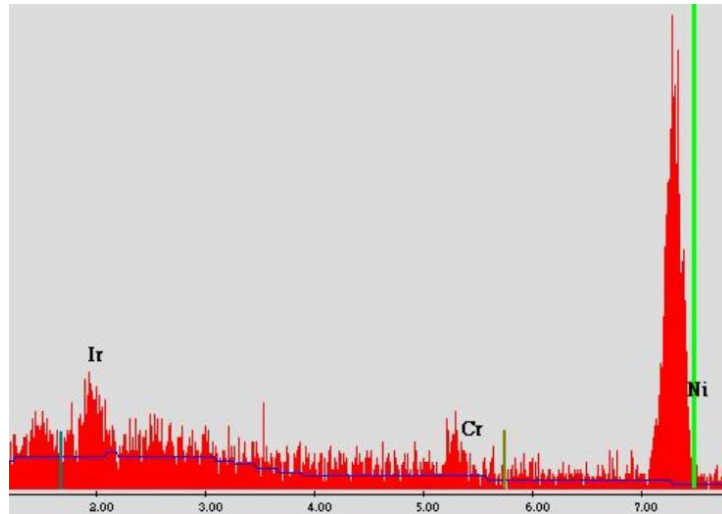
Figure 4- 7. Energy dispersive x-ray analysis result of the sol-gel iridium oxide film on the Cr-Ni electrode.

Table 4- 2. The proportion of the IrOx on the Ni-based electrodes before and after use.

Electrode Type	Before Test Wt%	Tested with PH 4-10 Wt%	Tested with PH 2-12 Wt%
Ni	88.53	87.31	60.80
Ti-Ni	91.76	89.74	57.23
Cr-Ni	87.43	85.40	63.60

and 10 buffer solutions, the amount of the iridium oxide slightly decreased for the Ni-based electrodes with or without adhesion layers. After being used in pH 2 and 12 buffer solutions, the amount of the iridium oxide significantly decreased for the Ni electrode without adhesion layer and the one with Ti adhesion layer. More iridium oxide is preserved on the electrode with Cr adhesion layer. The EDAX result is coherent with the SEM observations.

4.4.1.4. Measurement Results

The Ni-based IrOx working electrode is tested in the standard pH buffer solutions with a commercial Ag/AgCl reference electrode (MW-2021, Bioanalytical Systems Inc.) inside a beaker as shown in Figure 4-8.

Figure 4- 8. The pH measurement set up. [4.31]

The potential between the working and reference electrodes is measured by the National Instruments Data Acquisition card (NI DAQ - 6009). A lab view program is used to record the real-time potential with a sampling rate of 7 data points per second. The pH measurement is first conducted in the sequence from pH = 4 to pH = 10, then continued with a reversed order test from pH = 10 to pH = 4. For each electrode the experiment is repeated 3 times to check the consistency. The sensitivity, repeatability, and reversibility of the electrode are investigated. The measurement results of the Ni-based electrodes are shown in Figure 4-9.

The sensitivity for the Ni electrode is in the range of $57 - 65 \ ^{mV}/_{pH}$, with an average sensitivity of $59.19 \ ^{mV}/_{pH}$. The pH response is rapid and constant. The reversed order test shows good reversibility. After calculation, the electrode shows an average hysteresis error of 0.07 pH. The average pH discrepancy from the repeated test is 0.25 pH. The pH fluctuation is 0.27 pH.

The sensitivity for the Cr-Ni electrode is in the range of $54 - 57 \ ^{mV}/_{pH}$, with an average sensitivity of $55.99 \ ^{mV}/_{pH}$. The pH response is rapid and constant. The reversed order test shows good reversibility. After calculation, the electrode shows an average hysteresis error of 0.09 pH. The average pH discrepancy from the repeated test is 0.22 pH. The pH fluctuation is 0.44 pH.

The sensitivity for the Ti-Ni electrode is in the range of $54 - 55 \ ^{mV}/_{pH}$, with an average sensitivity of $53.67 \ ^{mV}/_{pH}$. The pH response is rapid and constant. The reversed order test shows good reversibility. After calculation, the electrode shows an average hysteresis error of 0.045 pH. The average pH discrepancy from the repeated test is 0.216 pH. The pH fluctuation is 0.32 pH.
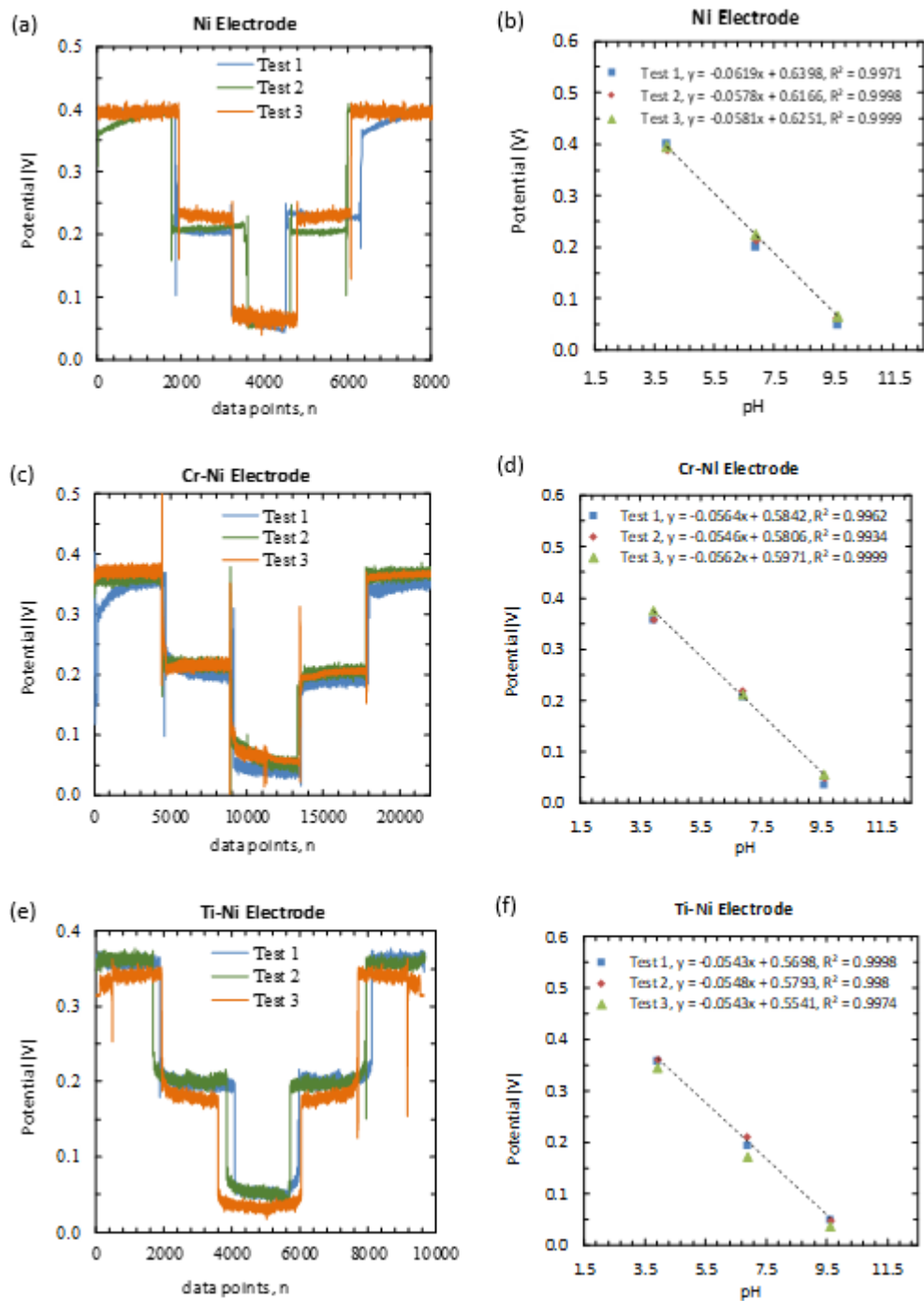
Figure 4- 9. The (a), (c), (e) repeated tests for the Ni-based electrodes and the (b), (d), (f) corresponding sensitivities.

4.4.2. Al-based Electrode

4.4.2.1. Fabrication Process

The fabrication process of the aluminum electrode is similar with the nickel electrode. The Fabrication process of the Al-based electrode is shown in Figure 4-5. First, A 125-micron thick Kapton film is cleaned with acetone and alcohol. Then, a layer of photoresist is spin on the Kapton film and patterned to form the sacrificial layer for metal deposition as shown in Figure 4-5 (a). To deposit the aluminum film, aluminum pellets with a purity of 99.99 % is used. The aluminum is deposited through the e-beam evaporation at a deposition rate of $1 - 1.5\,\text{Å}/s$. The thickness of the aluminum film is 200 nm. The deposited aluminum on the substrate and photoresist is shown in Figure 4-5 (b). After aluminum deposition, the photoresist sacrificial layer is removed by acetone. The aluminum electrode is achieved. Then, a layer of SU-8-100 photoresist is coated on the film as the sacrificial layer for the sol-gel process as shown in Figure 4-5 (c). After dip-coating, the film is slightly heated on a hot plate to remove the moisture. Then the SU-8-100 sacrificial layer is peeled off. A thermal treat is conducted on the aluminum electrode with the sol-gel solution to form the iridium oxide sensing film as shown in Figure 4-5 (d). Finally, a layer of SU-8-5 photoresist is patterned on the electrode as the insulation layer as shown in Figure 4-5 (e). The sideview of the completed electrode is shown in Figure 4-5 (e) and the top view of the electrode is shown in Figure 4-5 (f). The dish line indicates the metal underneath the SU-8-5 insulation layer.
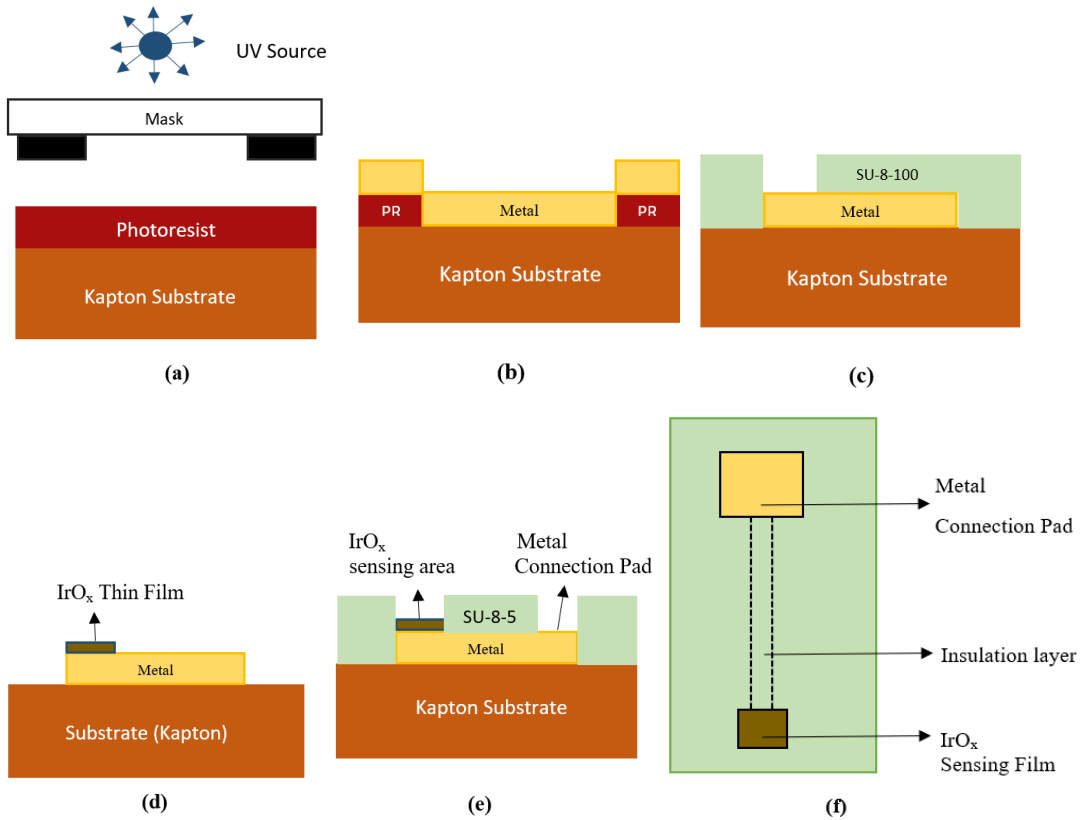
Besides the pure aluminum electrode, we also fabricated aluminum electrode with titanium as the adhesion layer. The fabrication process for the aluminum electrode with titanium adhesion layer is pretty much the same as described above, except for the metal deposition process. For the aluminum electrode with titanium adhesion layer (Ti-Al electrode), during the metal deposition process a thin layer of Ti (50 nm) is deposited on the Kapton film through e-beam deposition, following by the deposition of 200 nm Al. The deposition rate is $1 - 1.5\,\text{Å}/s$.

4.4.2.2. Scanning Electron Microscopy Analysis

SEM analysis is conducted to check the condition of the iridium oxide sensing film and the quality of the aluminum-based metal films. The analysis is first conducted on the electrode before use to check the initial condition. Then the analysis is conducted on the electrodes being tested with moderate acidic and alkaline buffer solutions (pH 4 and 10) and highly acidic and alkaline buffer solutions (pH 2 and 12) to evaluate the anti-corrosion ability. The results of the SEM analysis are shown in Figure 4-10.

From the SEM images we can see bumps on the Al film without adhesion layer. The rough surface is generated during the sol-gel deposition process. Due to the pour adhesiveness of the e-beam deposited Al on the Kapton film, during the sol-gel process the acidic solution affects the smoothness of the Al film and further influenced the formation of the iridium oxide film. By adding the adhesion layer of Ti the adhesiveness between the metal film and the polyimide substrate improved. The metal film will not be damaged by the sol-gel solution, hence the film
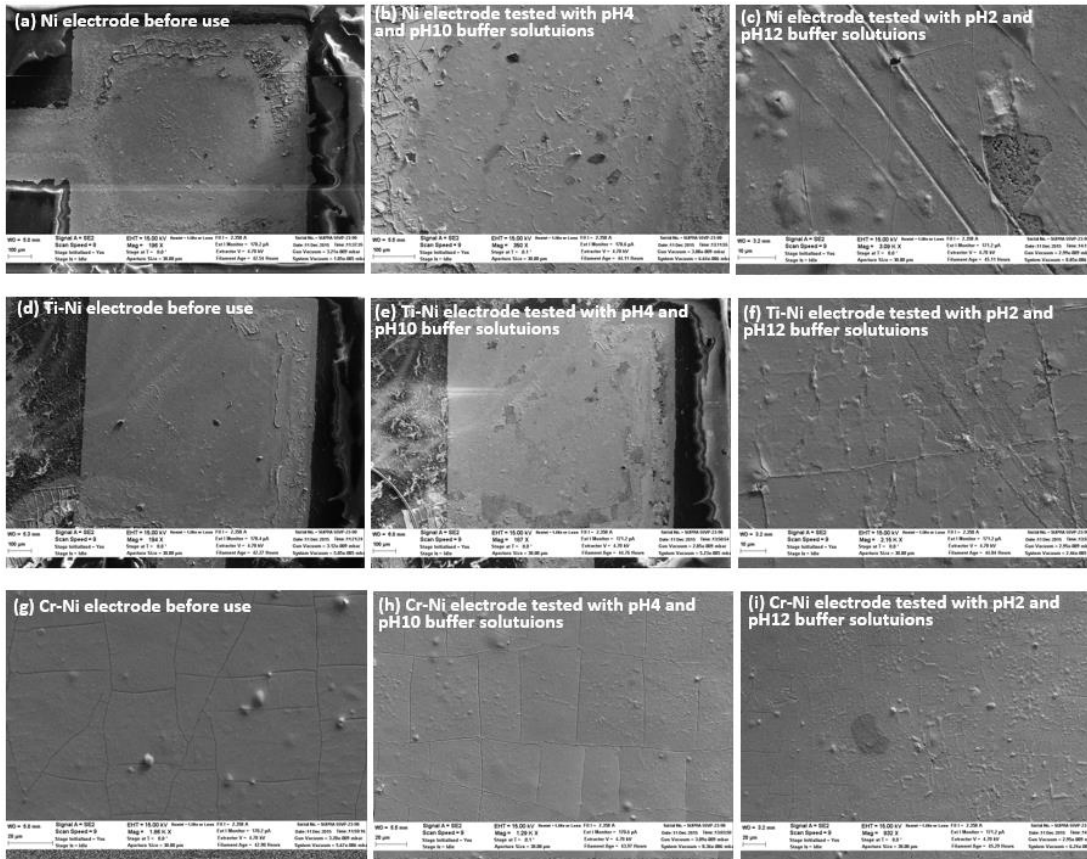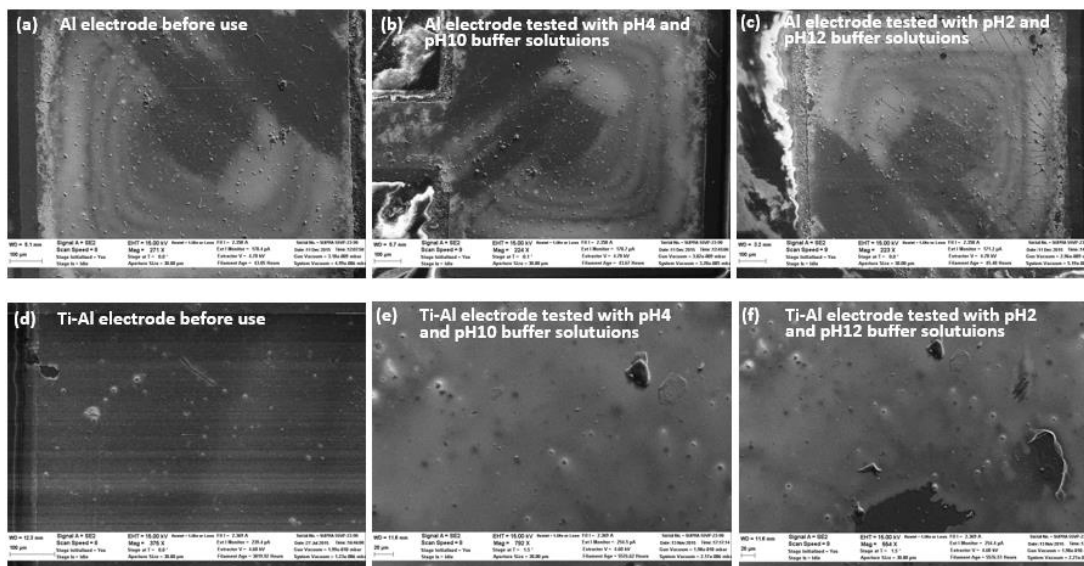

Figure 4- 10. SEM images of the (a) Al electrode before use and (b) Al electrode tested with pH 4 and 10 buffer solutions and (c) Al electrode tested with pH 2 and 12 buffer solutions; (d) Ti-Al electrode before use and (e) Ti-Al electrode tested with pH 4 and 10 buffer solutions and (f) Ti-Al electrode tested with pH 2 and 12 buffer solutions.

becomes smoother. In addition, the linear temperature expansion coefficient of Ti $((8.5 - 9) \cdot 10^{-6} \ {}^{m}/_{mK})$) is closer to the temperature expansion coefficient of iridium ($6.4 \cdot 10^{-6} \ {}^{m}/_{mK}$)) than that of Al $(21 - 24) \cdot 10^{-6} \ {}^{m}/_{mK}$). With the similar temperature expansion coefficient, the iridium oxide forms better crystalline structure during the thermal oxidation process on the Ti-Al electrode. With better iridium oxide film, the electrode is not likely to be influenced by the acidic or alkaline pH buffer solutions.

After tested with moderate pH buffer solutions we observed no damage on the sensing surface from as shown in Figure 4-10 (b) and (e). After tested with stronger acidic or alkaline pH buffer solutions, cracks were observed on the Al electrode, and the sensing film on the edges got eroded or etched away as shown in Figure 4-10 (c). For the Al electrode with Ti adhesion layer no cracks were observed, yet some parts of the IrOx was etched away, as shown in Figure 4-10 (f). Hence adding the adhesion layer of Ti could improve the durability of the Al electrode in the extremes of acidic or alkaline testing environment. The Al-based pH sensor are successfully tested in the range of pH 2-12 in the next section.

4.4.2.3. Electron Dispersive Analysis (EDAX)

To investigate the quantity of the iridium oxide film deposited on top of the Al-based electrodes after sol-gel deposition, we conducted the energy dispersive X-ray spectroscopy to check the surface composition of the sensing area. The samples are checked with the EDAX 4000 system in a Zeiss Supra 55 VP scanning electron microscope system. The EDAX analysis result of the iridium oxide film on the Cr-Ni electrode is shown in Figure 4-11. The peaks indicating the existence of Al, Cr, and Ir. The proportion of the iridium oxide on the electrode before use and after being used in moderate and strong acidic or alkaline pH buffer solutions are shown in Table 4-3. After being used in pH 4 and 10 buffer solutions, the amount of the iridium oxide slightly decreased for the Al-based electrodes with or without adhesion layers. After being used in pH 2 and 12 buffer solutions, the amount of the iridium oxide decreased furthermore. The EDAX result is coherent with the SEM observations.
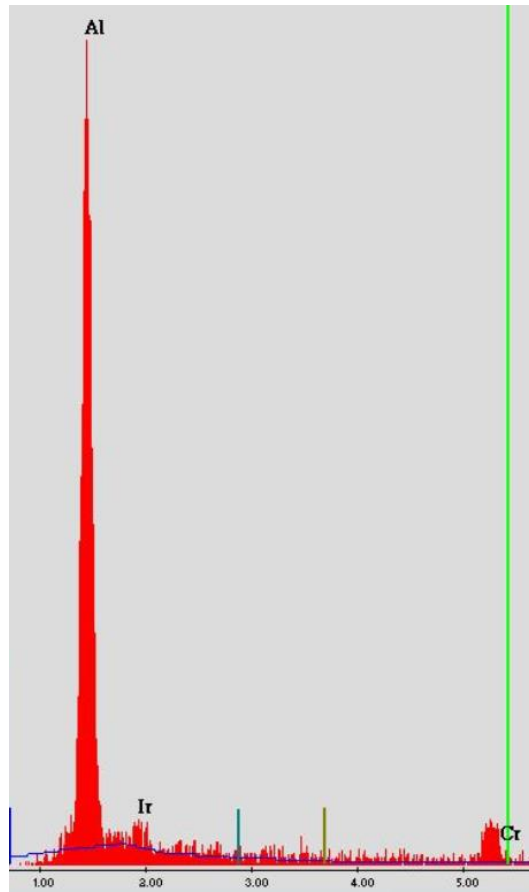
Figure 4- 11. Energy dispersive x-ray analysis result of the sol-gel iridium oxide film on the Ti-Al electrode.

Table 4- 3. The proportion of the iridium oxide on the Al-based electrode before and after use.

Electrode Type	Before Test Wt%	Tested with PH 4-10 Wt%	Tested with PH 2-12 Wt%
Al	73.04	69.95	67.62
Ti-Al	75.38	71.56	69.79

4.4.2.4. Measurement Results

Same as the experiments for the Ni-based electrode, the Al-based IrOx working electrode is tested in the standard pH buffer solutions with a commercial Ag/AgCl reference electrode (MW-2021, Bioanalytical Systems Inc.) inside a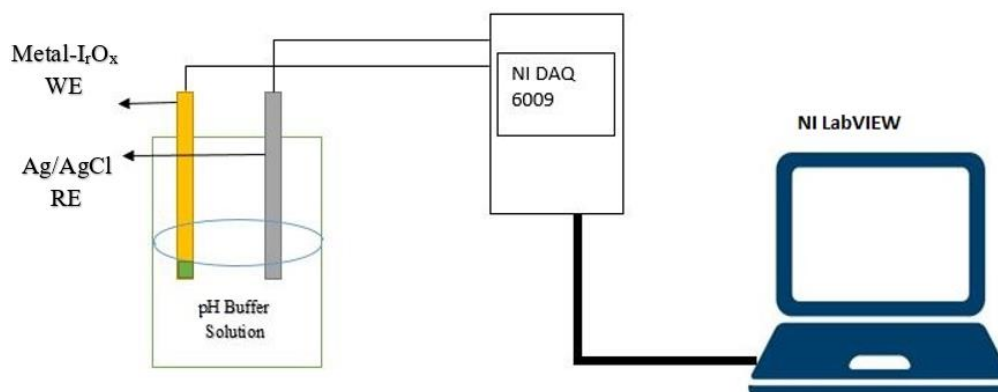 beaker as shown in Figure 4-8. The potential between the working and reference electrodes is measured by the National Instruments Data Acquisition card (NI DAQ - 6009). A lab view program is used to record the real-time potential with a sampling rate of 7 data points per second. The pH measurement is first conducted in the sequence from pH = 2 to pH = 12, then continued with a reversed order test from pH = 12 to pH = 2. For each electrode the experiment is repeated 3 times to check the consistency. The sensitivity,
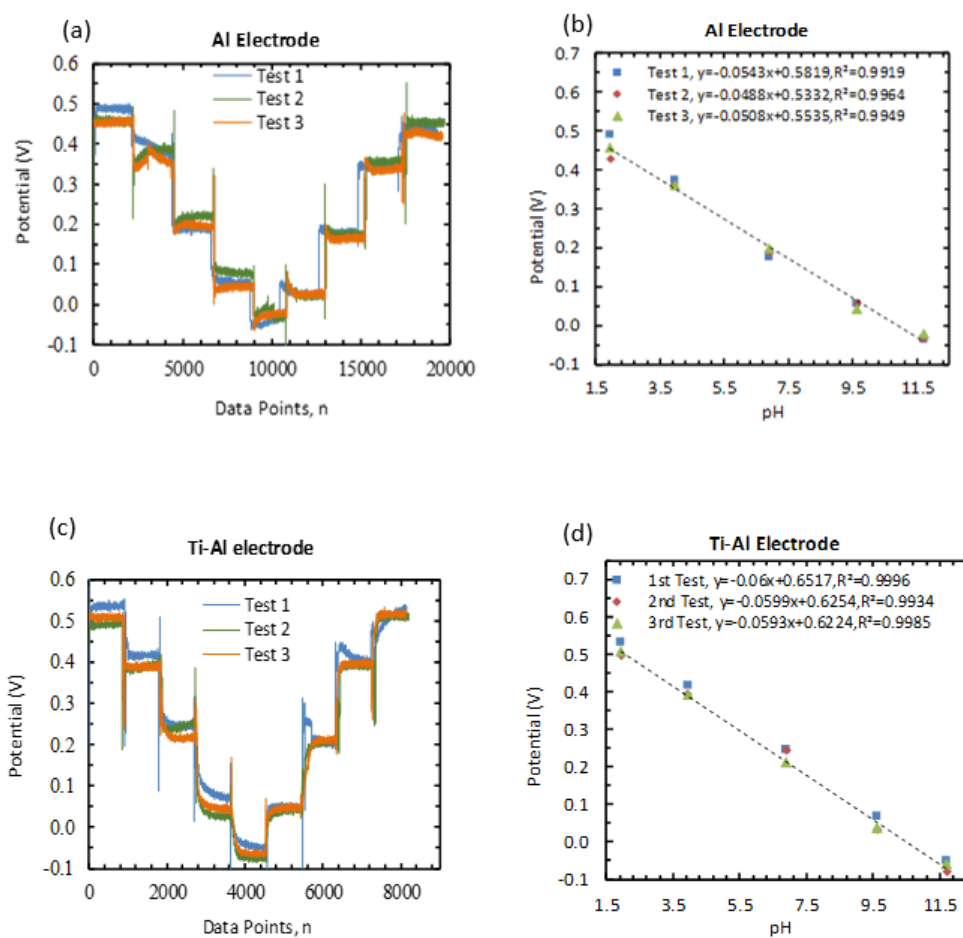
Figure 4- 12. The (a), (c) repeated test and the (b), (d) sensitivity for the Al-based

repeatability, and reversibility of the electrode are investigated. The measurement results of the Al-based electrodes are shown in Figure 4-12.

The sensitivity for the Al electrode is in the range of $48 - 55 \ {mV}/{pH}$, with an average sensitivity of $50.87 \ {mV}/{pH}$. The pH response is rapid but with slight fluctuation. A noticeable hysteresis error is observed from the reversed order test. After calculation, the electrode shows an average hysteresis error of 0.58 pH. The average pH discrepancy from the repeated test is 0.37 pH. The pH fluctuation is 0.51 pH.

The sensitivity for the Ti-Al electrode is in the range of $59 - 61 \ {mV}/{pH}$, with an average sensitivity of $60.03 \ {mV}/{pH}$. The pH response is rapid but with slight fluctuation. A noticeable hysteresis error is observed from the reversed order test. After calculation, the electrode shows an average hysteresis error of 0.42 pH. The average pH discrepancy from the repeated test is 0.38 pH. The pH fluctuation is 0.4 pH.

### 4.4.3.Discussions and Conclusions

To consistently evaluate the performance of the electrodes made with different metals, we defined the performance related parameters as shown in Figure 4-13 [4.23]. The potential fluctuation (ΔV) is the non-random voltage fluctuating range after the potential become stabilized. The potential deviation (δV) is defined as the potential difference among tests within the same solution for the same electrode. The potential drift (V') is defined as the difference between the peak potential and 90% of the equilibrium potential. The hysteresis error (dV) is defined as the difference of the potential for the same solution during the cyclic pH testing. The potential fluctuation is related to the accuracy of the pH sensor. Minimize the potential fluctuation will improve the detection accuracy. The potential deviation is related to the repeatability of the pH sensor. Minimize the potential deviation will improve the repeatability, hence achieve a pH senor with stable performance. The potential drift is related to the responsivity of the pH sensor. The smaller the potential drift, the faster the pH sensor could reach to the equilibrium potential, which

means less responding time is needed for the pH sensor. The hysteresis is related to the reversibility of the pH sensor. Minimize the hysteresis will improve the reversibility of the pH sensor. The performance of the iridium oxide pH sensor with different metal types is shown in Table 4-4.
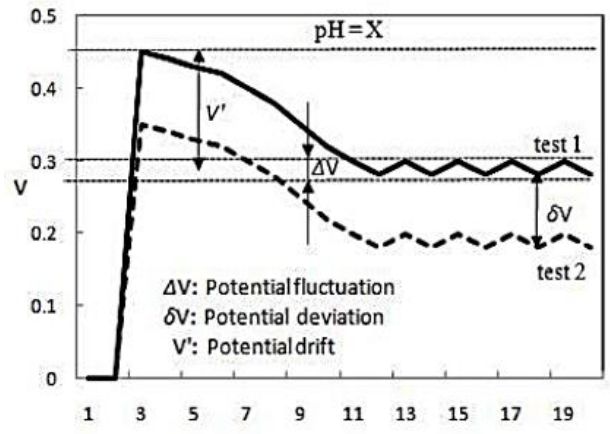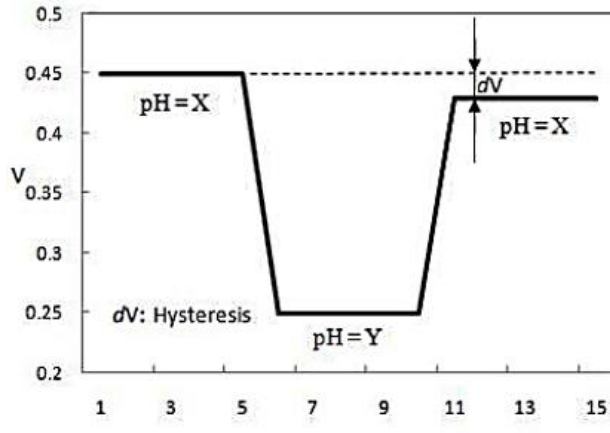
Figure 4- 13. Illustrations of the (a) potential drift, fluctuation and deviation, and (b) hysteresis error. [4.23]

Table 4- 4. The performance of the iridium oxide pH sensor with different metal types.

Type of Eelctrode	pH Range	Sensitivity	Average Hysteresis (dV)	Average Potential Fluctuation (ΔV)	Average Potential Deviation (δ V)	Average Potential Drift (V')
Ni Electrode	4 to 10	59.17 mV/pH	4.1 mV	16.2 mV	12.25 mV	14.96 mV
Cr-Ni Electrode	4 to 10	55.9 mV/pH	5.02 mV	24.73 mV	12.22 mV	12.44 mV
Ti-Ni Electrode	4 to 10	53.67 mV/pH	2.42 mV	17 mV	12.77 mV	11.64 mV
Al Electrode	2 to 12	50.87 mV/pH	29.69 mV	25.8 mV	18.595 mV	23.062 mV
Ti-Al Electrode	2 to 12	60.03 mV/pH	25.396 mV	24.147 mV	22.964 mV	25.414 mV
Cr-Au Electrode	2 to 12	54.6 mV/pH	4.42 mV	6.28 mV	10.2 mV	8.5 mV

In general, the Ni-based sensors have lower potential fluctuation and lower potential deviation than the Al-based sensors, which means less surface charge variation is caused in the measurement. The potential drift and the hysteresis of the Ni-based electrodes are also lower than that of the Al-based electrodes. However, the pH measurement range of the Ni-based electrodes is narrow. The Al-based electrodes have a longer testing range from strong acid to alkaline. Comparing with the regular Cr-Au electrode (discussed in the previous section), the Ni-based electrode has the advantages of lower cost and lower hysteresis. The disadvantages of the Ni-based electrode are the narrow testing range, poor stability, and longer response time. The Al-based sensors has the same testing range as the Cr-Au electrode, higher sensitivity, and lower

fabrication cost; however, the other performance parameters are not compatible with the Cr-Au electrode. In conclusion, to make a pH sensor suitable for bio applications which requires good stability, accuracy and wide pH measurement range, with current fabrication techniques the Cr-Au electrode is the best choice. In the future, research will be conducted to improve the performance of the Ni-based and Al-based IrOx electrodes. Better metal deposition technique and suitable iridium oxide deposition technique will be investigated.

4.5. Study of the Hysteresis Effect

4.5.1. Literature Review of Hysteresis Effect

Hysteresis is one of the mechanism limitations that affects the response of the pH sensor. The hysteresis is defined as the potential mismatch for the same testing solution when the same device is tested in a complete pH cycle which is from acid to alkaline and then back to acid, or in the reversed order. Due to the significant influence on the accuracy of pH sensing, there are many investigations on the hysteresis phenomenon and attempts to minimize the hysteresis value [4.30-4.32]. Bousse reported that the hysteresis behavior depends on the nature of the electrolyte solution. The presence of a high concentration of OH^- or F^- ions leads to a large hysteresis due to the delay of the pH response [4.35]. Tsai and Bousse [4.34, 4.35] reported the hysteresis can be reduced by testing the pH in a certain sequence due to the different diffusion rate of the hydrogen ion and the hydroxonium ion. For the electrode with sensing area less than $2 \times 2 \ mm^2$ a smaller hysteresis can be achieved by testing the sensor in the acid-first pH cycle (pH 7-4-7-10-7). While when the sensing area is larger than $2 \times 2 \ mm^2$, a smaller hysteresis can be achieved by testing the sensor in the alkali-first pH cycle (pH 7-10-7-4-7). However, in the real-life pH measurement the ion composition of the target solution is usually unknown and the feasibility of testing the pH in such an order is very low.

The factors that could cause the hysteresis phenomenon for the IrOx or other metal oxide films are also investigated. Yao reported the hysteresis is related to the oxidation state of the sensing material [4.7]. Kwon improved the stability of the pH sensor by modifying the sensing

material with the heat treatment [4.33]. Olthuis reported the hysteresis is related to the degree of hydration of the sensing material [4.11]. Due to the new equilibrium established in the redox reaction, the electrochemical potential could be changed in the reversible reaction.

In this section, we investigated the hysteresis of the pH sensor made with different metal types and different sensing areas. As discussed in the previous section, the formation of the iridium oxide sensing film is affected by the underneath metal film on the electrode. And the quality of the IrOx film varies for the same type of metal electrode with or without adhesion layers. First, we compared the hysteresis of the Ni, Al, and Au based electrodes with or without the adhesion layers in the acid, neutral, and alkaline environment. Then, we compared the hysteresis of the Cr-Au electrode with different sensing areas in the acid, neutral, and alkaline environment. The causal relationship between the hysteresis and the metal type, the electrode size, and the pH of the testing environment is established for the iridium oxide pH sensor.

4.5.2. Hysteresis of the pH Sensors Made with Different Metals

4.5.2.1. Sensor Design and Fabrication

The Ni-based IrOx electrodes are fabricated in the following steps. First, the 125 μm thick flexible Kapton film with the size of $8 \times 8\ cm^2$ is cleaned by methanol, alcohol and DI water to strip off the dust particles from the surface. Then the Kapton film is loaded into the pre-cleaned E-Beam evaporator chamber. Three depositions were conducted respectively: 200 nm of Ni; 50 nm of Cr followed by 200 nm of Ni; and 50 nm of Ti followed by 200 nm of Ni. The deposition rate is maintained at $1 - 1.5\ \text{Å}/s$. In addition to Cr and Ti, amorphous carbon is also used as the adhesion layer. The amorphous carbon is deposited on the Kapton film by sputtering using a carbon target, then the film is loaded into the E-Beam evaporator chamber to deposit 200 nm of Ni. After the metal deposition process, the metal film is cut into stripes with the size of $1 \times 10\ mm^2$. The sol-gel process is then conducted to deposit the iridium oxide sensing film on the metal stripe. After the dip-coating and thermal treatment, the iridium oxide sensing film is successfully deposited on the electrode. Finally, a coper wire is attached to the electrode with the silver epoxy.

The Al-based IrOx electrodes are fabricated in the following steps. First, the 125 µm thick flexible Kapton film with the size of $8 \times 8 \ cm^2$ is cleaned by methanol, alcohol and DI water to strip off the dust particles from the surface. Then the Kapton film is loaded into the pre-cleaned E-Beam evaporator chamber. Two depositions were conducted respectively: 200 nm of Al; and 50 nm of Ti followed by 200 nm of Al. The deposition rate is maintained at $1 - 1.5 \ Å/s$. After the metal deposition process, the metal film is cut into stripes with the size of $1 \times 10 \ mm^2$. The sol-gel process is then conducted to deposit the iridium oxide sensing film on the metal stripe. After the dip-coating and thermal treatment, the iridium oxide sensing film is successfully deposited on the electrode. Finally, a coper wire is attached to the electrode with the silver epoxy.

The Au-based IrOx electrodes are fabricated in the following steps. First the 125 µm thick flexible Kapton film with the size of $8 \times 8 \ cm^2$ is cleaned by methanol, alcohol and DI water to strip off the dust particles from the surface. Then the Kapton film is loaded into the pre-cleaned E-Beam evaporator chamber. Three depositions were conducted respectively: 50 nm of Cr followed by 200 nm of Au; 50 nm of Cu followed by 200 nm of Au; and 30 nm of Cr followed 50 nm of Cu and 200 nm of Au. The deposition rate for Cu is maintained at $0.5 \ Å/s$, for Cr is maintained at $1.5 \ Å/s$, and for Au is maintained at $3.2 \ Å/s$. After metal deposition the film is cut into stripes with the size of $1 \times 10 \ mm^2$. The sol-gel process is then conducted to deposit the iridium oxide sensing film on the metal stripe. After the dip-coating and thermal treatment, the iridium oxide sensing film is successfully deposited on the electrode. Finally, a coper wire is attached to the electrode with the silver epoxy.

The reference electrode is fabricated by printing the AgCl paste on the Kapton film. The Kapton strip with the same size of the IrOx electrode ($1 \times 10 \ mm^2$) is first cleaned by acetone and dried by pressurized air. Then appropriate amount of the AgCl paste (CH Instruments, Inc.) is printed over the Kapton strip and heated at 125°C for 15 minutes for stabilization. Finally, a coper wire is attached to the reference electrode with silver epoxy.

4.5.2.2. Measurement Procedures

The pH sensor is tested with standard pH buffer solutions. The potential difference between the IrOx working electrode and the AgCl reference electrode is measured by the data acquisition (NI DAQ-609) card. The real-time potential is recorded by a LabVIEW-based program with a sampling rate of 7.5 samples per second. The pH circle of pH 4-7-10-7-4 is designed to carry out the hysteresis experiment. As shown in Figure 4-14, two continuous loop circles are conducted for each pH sensor. The hysteresis in the acid environment is obtained by measuring the potential difference of the pH = 4 buffer solution during the cyclic pH testing in circle 1. The hysteresis in the neutral environment is obtained by measuring the potential difference of the pH = 7 buffer solution during the cyclic pH testing in circle 1. The hysteresis in the alkaline environment is obtained by measuring the potential difference of the pH = 10 buffer solution in circle 1 and circle 2. The hysteresis of the pH sensors made with different metals and adhesion layers are evaluated.
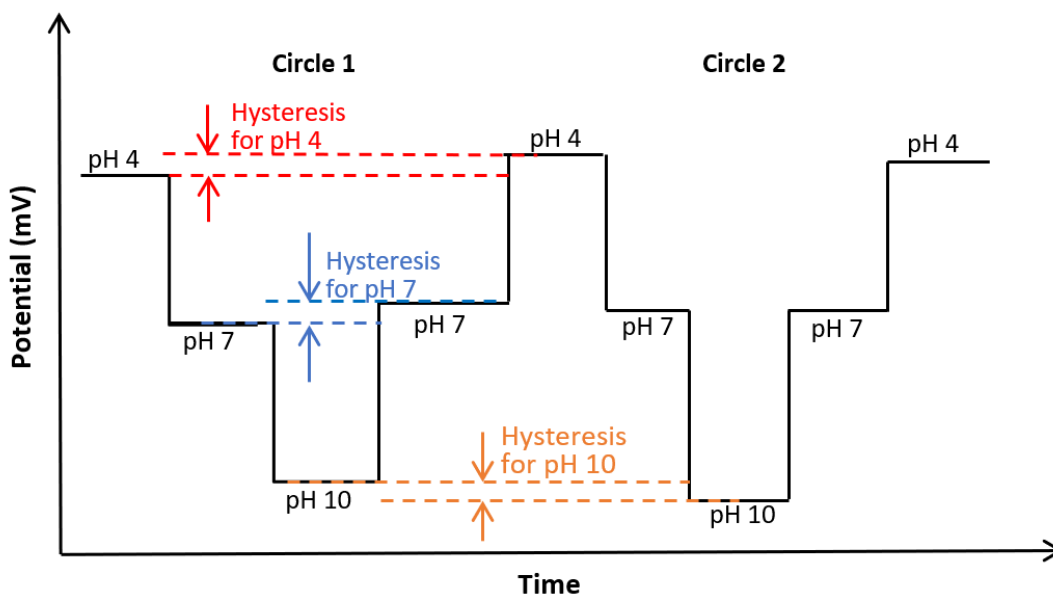
Figure 4- 14. Demonstration of the 2 continuous loop circles pH 4-7-10-7-4.

4.5.2.3. Results and Discussions

The performance of the Ni-based electrode is shown in Figure 4-15 (a). The hysteresis of the pure Ni electrode in pH = 4 buffer solution is 9.7 mV/pH, which presents ΔpH = 0.16; in pH = 7 buffer solution is 25.3 mV/pH, which presents ΔpH = 0.43; in pH = 10 buffer solution is 22.4 mV/pH, which presents ΔpH = 0.38. After adding Cr as the adhesion layer, the hysteresis reduced for all the three pH levels. The hysteresis of the Cr-Ni electrode in pH = 4 buffer solution is 7.3 mV/pH, which presents ΔpH = 0.13; in pH = 7 buffer solution is 4.1 mV/pH, which presents ΔpH = 0.07; in pH = 10 buffer solution is 9.3 mV/pH, which presents ΔpH = 0.17. After adding Ti as the adhesion layer, the hysteresis reduced for pH = 7 and 10 buffer solutions, however it increased for pH = 4 buffer solution. The hysteresis of the Ti-Ni electrode in pH = 4 buffer solution is 14.1 mV/pH, which presents ΔpH = 0.26; in pH = 7 buffer solution is 14.1 mV/pH, which presents ΔpH = 0.26; in pH = 10 buffer solution is 12.1 mV/pH, which presents ΔpH = 0.23. Amorphous carbon is also used to modify the Ni electrode. After adding a layer of C the hysteresis greatly reduced for the pH = 10 buffer solution, and slightly reduced for pH = 4 and 7 buffer solutions. The hysteresis of the C-Ni electrode in pH = 4 buffer solution is 19.9 mV/pH, which presents ΔpH = 0.43; in pH = 7 buffer solution is 14.5 mV/pH, which presents ΔpH = 0.32; in pH = 10 buffer solution is 3.6 mV/pH, which presents ΔpH = 0.08. The average hysteresis of the Ni-based electrodes in potential is shown in Figure 4-15(b), in ΔpH is shown in Figure 4-15(c). We can see that after adding the adhesion layers the hysteresis decreased. The Cr-Ni electrode presented the lowest hysteresis phenomenon. Though the C-Ni electrode has lower hysteresis in potential than the Ti-Ni electrode, after converting to ΔpH it shows higher hysteresis, due to the relatively lower sensitivity.

The performance of the Al-based electrode is shown in Figure 4-16 (a). The hysteresis of the pure Al electrode in pH = 4 buffer solution is 39.2 mV/pH, which presents ΔpH = 0.77; in pH = 7 buffer solution is 18.3 mV/pH, which presents ΔpH = 0.36; in pH = 10 buffer solution is 35 mV/pH, which presents ΔpH = 0.69. After adding Ti as the adhesion layer, the hysteresis reduced
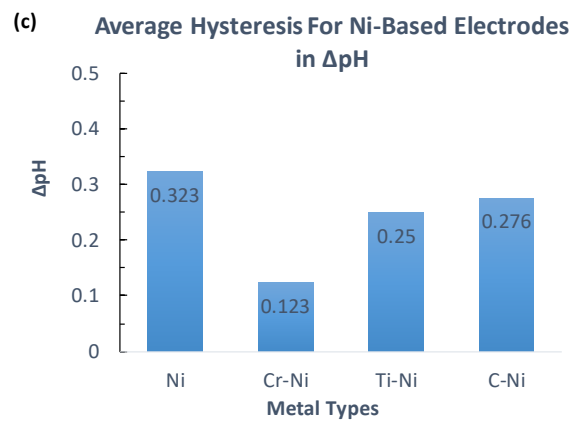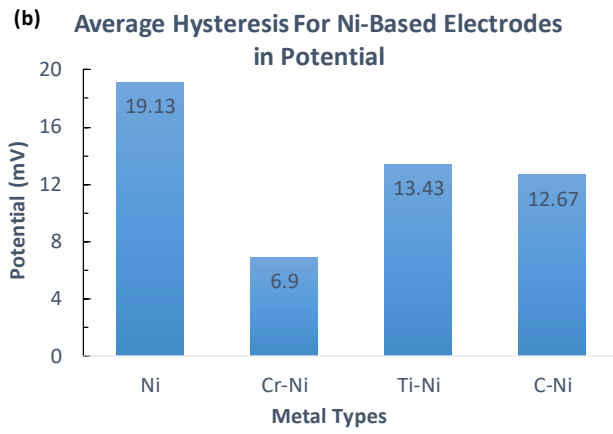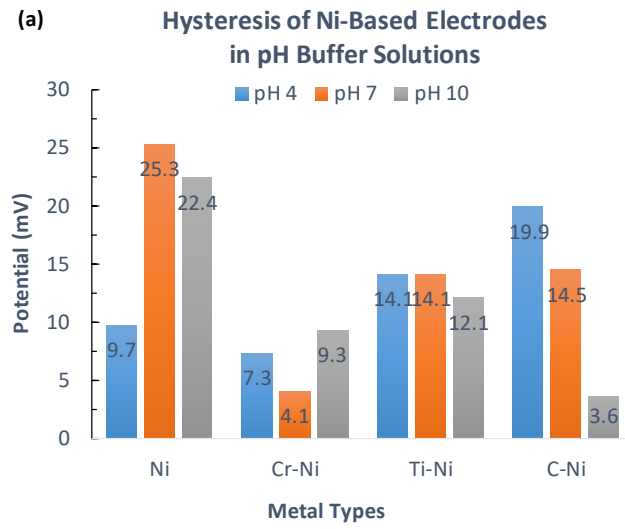
Figure 4- 15. Graphs of (a) hysteresis of the Ni-based electrodes in pH = 4, 7, and 10 buffer solutions; (b) average hysteresis in terms of potential; and (c) average hysteresis in terms of pH.

for pH = 4 buffer solution, however it increased for pH =7 buffer solution and maintained the same for pH = 10 buffer solution. The hysteresis of the Ti-Al electrode in pH = 4 buffer solution is 17.5 mV/pH, which presents ΔpH = 0.29; in pH = 7 buffer solution is 33.2 mV/pH, which presents ΔpH = 0.55; in pH = 10 buffer solution is 35 mV/pH, which presents ΔpH = 0.58. The average hysteresis of the Al-based electrodes in potential is shown in Figure 4-16 (b), in ΔpH is shown in Figure 4-16 (c). We can see that after adding the adhesion layer the hysteresis decreased in the acidic testing environment, however it became worse for the natural environment and maintain the same for the alkaline environment.

The performance of the Au-based electrode is shown in Figure 4-17 (a). The hysteresis of the Cr-Au electrode in pH = 4 buffer solution is 0.1 mV/pH, which presents ΔpH = 0.002; in pH = 7 buffer solution is 6.7 mV/pH, which presents ΔpH = 0.11; in pH = 10 buffer solution is 14.2 mV/pH, which presents ΔpH = 0.24. The hysteresis of the Cu-Al electrode in pH = 4 buffer solution is 3.4 mV/pH, which presents ΔpH = 0.06; in pH = 7 buffer solution is 10.9 mV/pH, which presents ΔpH = 0.198; in pH = 10 buffer solution is 14.7 mV/pH, which presents ΔpH = 0.27. After adding Cr as the adhesion layer for the Cu-Au electrode, the hysteresis reduced for all the three pH buffer solutions. The hysteresis of the Cr-Cu-Au electrode in pH = 4 buffer solution is 3.4 mV/pH, which presents ΔpH = 0.59; in pH = 7 buffer solution is 2.6 mV/pH, which presents ΔpH = 0.045; in pH = 10 buffer solution is 2.9 mV/pH, which presents ΔpH = 0.05. The average hysteresis of the Au-based electrodes in potential is shown in Figure 4-17 (b), in ΔpH is shown in Figure 4-17 (c). We can see that with two adhesion layers: Cr and Cu, the electrode shows lowest hysteresis.

The comparison of all the electrodes are shown in Figure 4-18. In conclusion, the Au-based electrodes have the lowest hysteresis, the Al-based electrodes has the highest hysteresis. In general, by adding the adhesion layers the hysteresis reduced. Because adding the adhesion layer improved the conformity of the metal layer, hence improved the formation of the IrOx sensing film. The hysteresis in the alkaline condition is normally severe than that in the acid condition, due to the different diffusion speed of the hydrogen ion and the hydroxonium ion. In acid, the primary
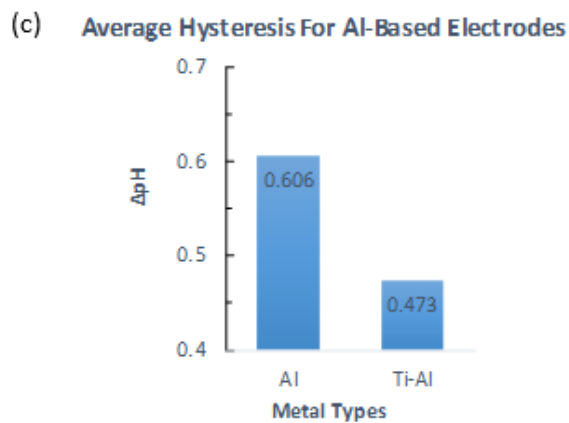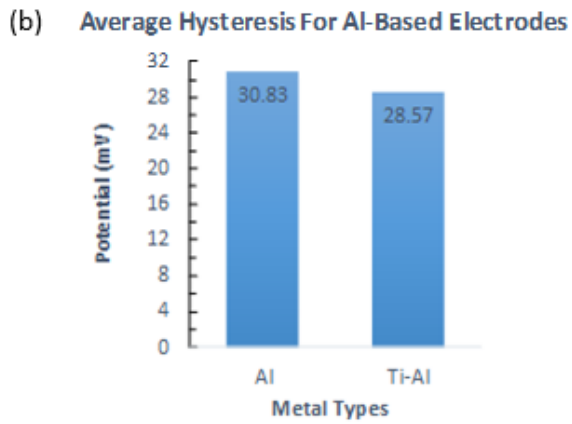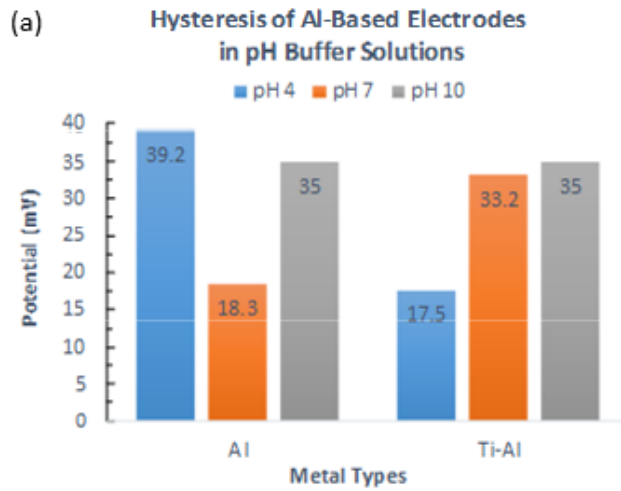
Figure 4- 16. Graphs of (a) hysteresis of the Al-based electrodes in pH = 4, 7, and 10 buffer solutions; (b) average hysteresis in terms of potential; and (c) average hysteresis in terms of pH.
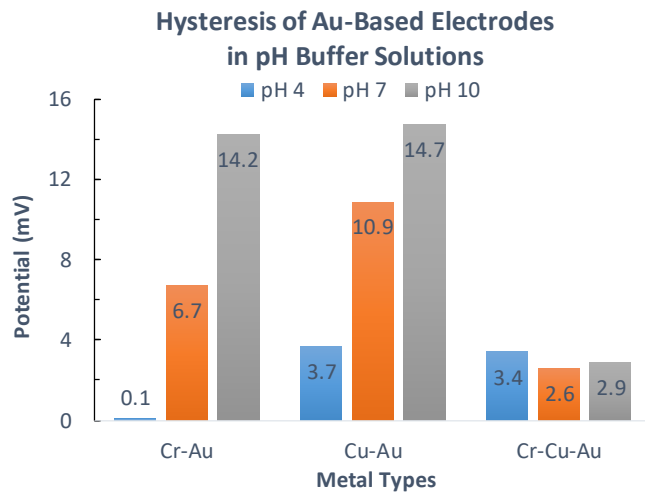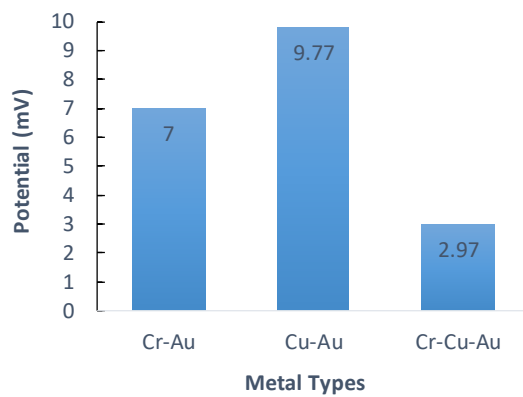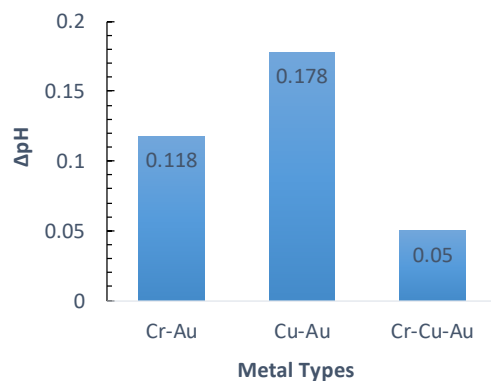
Figure 4- 17. Graphs of (a) hysteresis of the Au-based electrodes in pH = 4, 7, and 10 buffer solutions; (b) average hysteresis in terms of potential; and (c) average hysteresis in terms of pH.

(a)

Hysteresis of Electrode with Different Metals in pH Buffer Solutions

(b)

Average Hysteresis for Electrodes with Different Metals in Potential

(c)

Average Hysteresis for Electrodes with Different Metals in pH
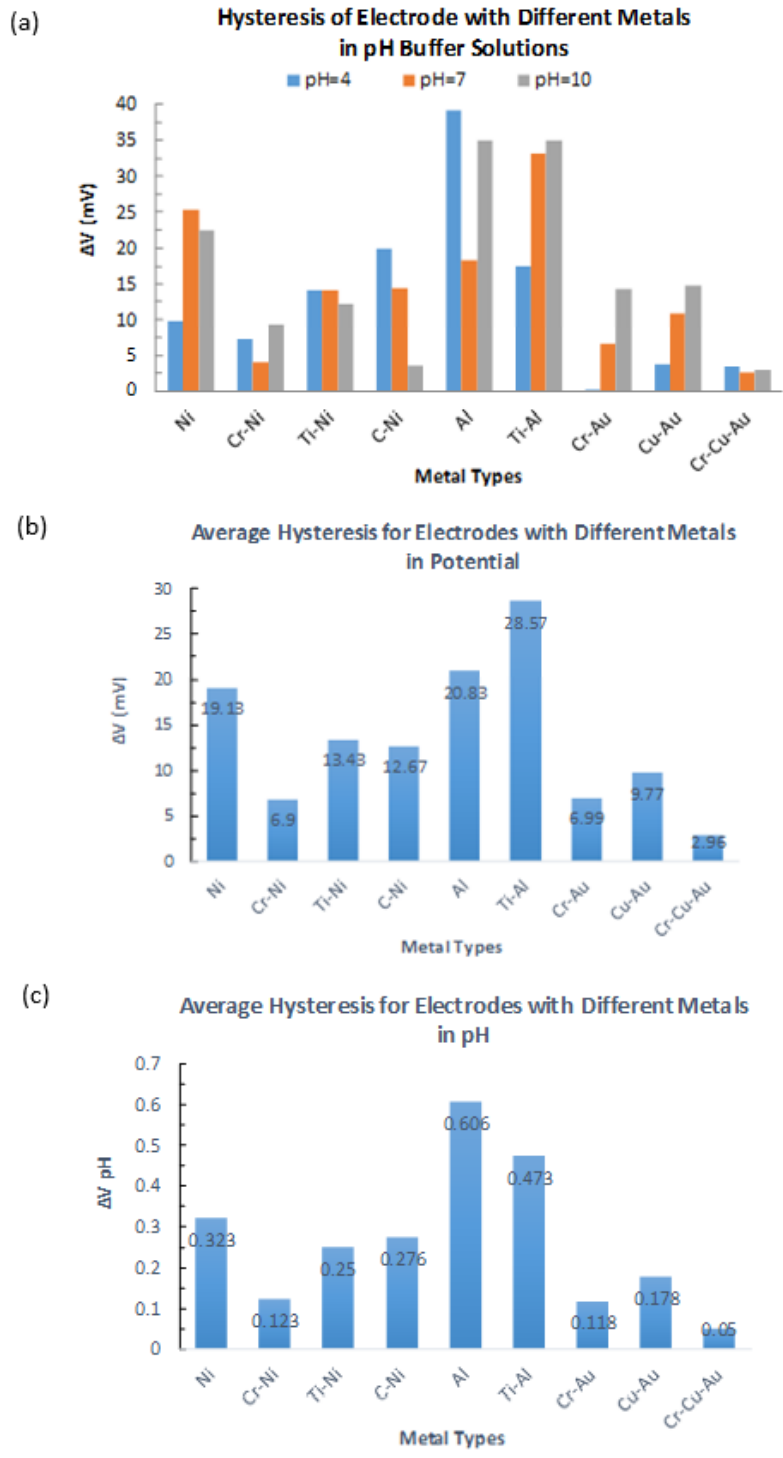
Figure 4- 18. Graphs of (a) hysteresis of the electrodes with different metals in pH = 4, 7, and 10 buffer solutions; (b) average hysteresis in terms of potential; and (c) average hysteresis in terms of pH.

proton reacting with sensing film is hydrogen ion while in alkali it's hydroxonium ion. Hydrogen ion diffuses faster than the hydroxonium ion, the presence of a high concentration of OH^- leads to a large hysteresis due to the delay of the pH response.

4.5.3. Hysteresis of the pH Sensors with Different Sensing Areas

4.5.3.1. Sensor Design and Fabrication

The Cr-Au electrode with different sizes are fabricated for the study of the relationship between the hysteresis and the sensing area. The fabrication process is similar as the previous section. First, the flexible Kapton film is deposited with 50 nm of Cr and 200 nm of Au by the e-beam evaporation. Then the film is cut into stripes with the size of $1 \times 10 \ mm^2$ (small), $2 \times 10 \ mm^2$ (medium), and $4 \times 10 \ mm^2$ (large) respectively. The sol-gel process is then conducted to deposit the iridium oxide sensing film on the stripes. Finally, a coper wire is attached to the electrode with silver epoxy.

The reference electrodes with the size of $1 \times 10 \ mm^2$, $2 \times 10 \ mm^2$, and $4 \times 10 \ mm^2$ are fabricated by printing the AgCl paste on the Kapton film. The Kapton strips with different sizes are first cleaned by acetone and dried by pressurized air. Then appropriate amount of the AgCl paste (CH Instruments, Inc.) is printed over the Kapton strips and heated at 125°C for 15 minutes for stabilization. Finally, a coper wire is attached to the reference electrode with silver epoxy.

4.5.3.2. Measurement Procedures

The pH sensor is tested with standard pH buffer solutions. The potential difference between the IrOx working electrode and the AgCl reference electrode with the identical size is measured by the data acquisition (NI DAQ-609) card. The real-time potential is recorded by a LabVIEW-based program with a sampling rate of 7.5 samples per second. The pH loop circle of pH 1-4-7-10-13-10-7-4-1 is designed to carry out the hysteresis experiment.

As shown in Figure 4-19, two continuous loop circles are conducted for each pH measurement. The hysteresis in the strong acid environment is obtained by measuring the potential difference of the pH = 1 buffer solution during the cyclic pH testing in circle 1. The

78

hysteresis in the mild acidic environment is obtained by measuring the potential difference of the pH = 4 buffer solution during the cyclic pH testing in circle 1. The hysteresis in the neutral environment is obtained by measuring the potential difference of the pH = 7 buffer solution during the cyclic pH testing in circle 1. The hysteresis in the mild alkaline environment is obtained by measuring the potential difference of the pH = 10 buffer solution during the cyclic pH testing in circle 1. The hysteresis in the strong alkaline environment is obtained by measuring the potential difference of the pH = 13 buffer solution in circle 1 and circle 2. For each sensor size three electrodes are tested to calculate the standard deviation. The hysteresis of the pH sensors with different sensing areas are evaluated.
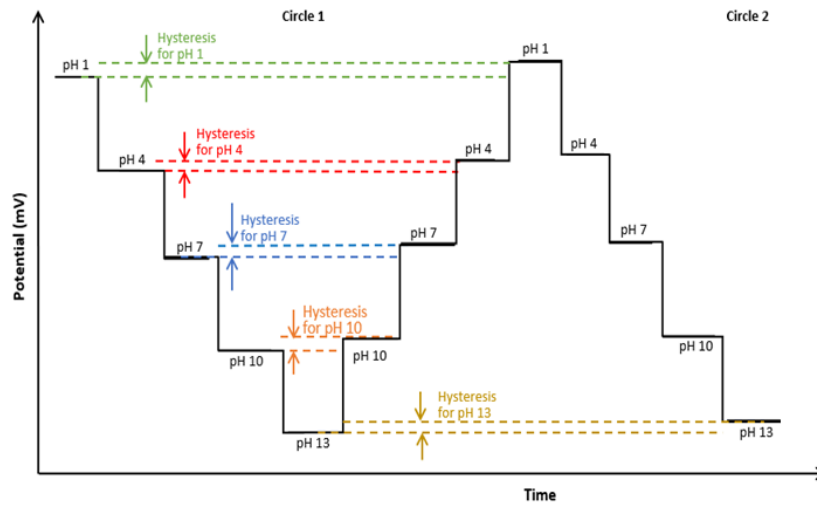
Figure 4- 19. Demonstration of the 2 continuous loop circles pH 1-4-7-10-13-10-7-4-1.

4.5.3.3. Measurement Results and Discussions

The performance of the Cr-Au electrode with different sizes is shown in Figure 4-20 (a) and (b). For each size the electrode is tested three time to check the repeatability. Standard deviation is calculated. The hysteresis of the small Cr-Au electrode in pH = 1 buffer solution is
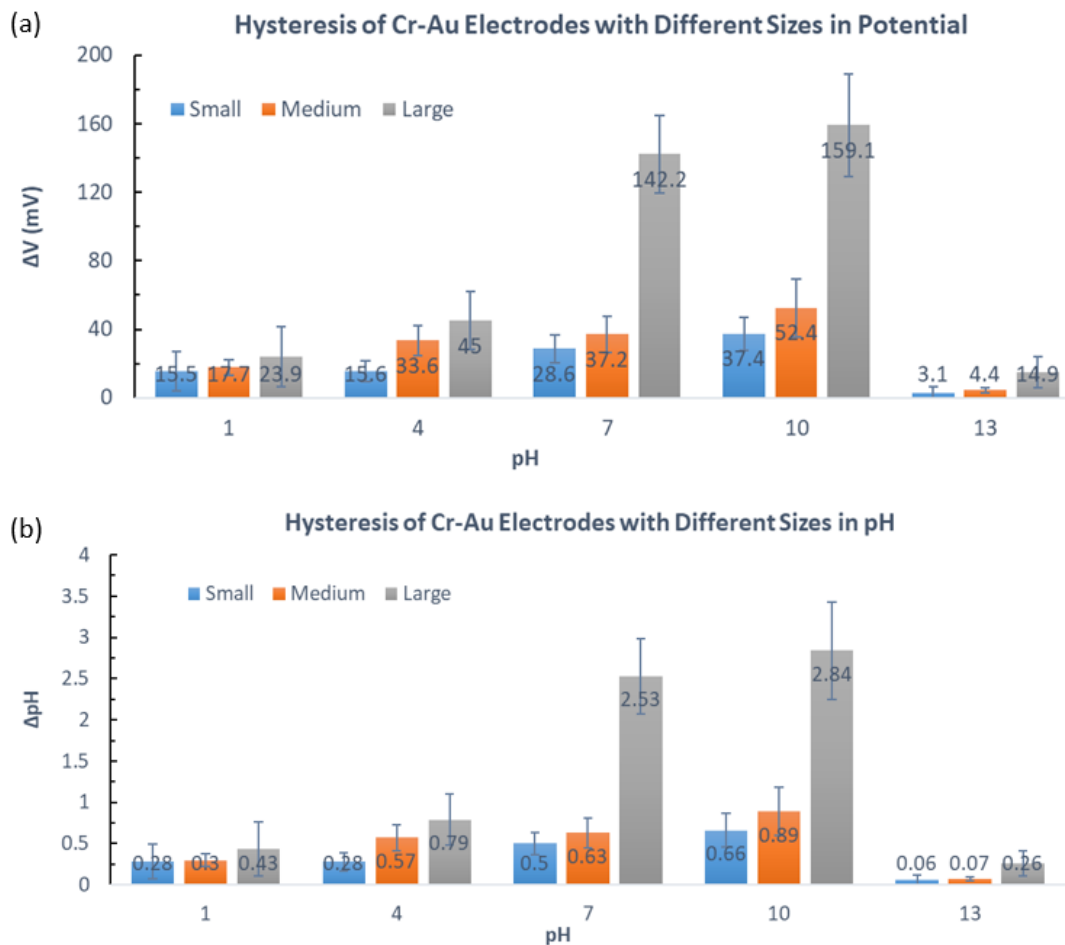
Figure 4- 20. Graphs of the hysteresis of the Cr-Au electrodes in pH = 1,4, 7, 10, and 13 buffer solutions in terms of (a) potential and (b) pH.

15.5 mV/pH with a standard deviation of 11.23 mV, which presents ΔpH = 0.28 with a standard deviation of 0.21; in pH = 4 buffer solution is 15.6 mV/pH with a standard deviation of 5.89, which presents ΔpH = 0.28 with a standard deviation of 0.11; in pH = 7 buffer solution is 28.6 mV/pH with a standard deviation of 8.15 mV, which presents ΔpH = 0.5 with a standard deviation of 0.13; in pH = 10 buffer solution is 34.7 mV/pH with a standard deviation of 9.83 mV, which presents ΔpH = 0.66 with a standard deviation of 0.21; in pH = 13 buffer solution is 3.1 mV/pH with a standard deviation of 3.26mV, which presents ΔpH = 0.06, with a standard deviation of 0.06.

The hysteresis of the medium Cr-Au electrode in pH = 1 buffer solution is 17.7 mV/pH with a standard deviation of 4.58 mV mV, which presents ΔpH = 0.3 with a standard deviation of 0.08; in pH = 4 buffer solution is 33.6 mV/pH with a standard deviation of 8.78, which presents ΔpH = 0.57 with a standard deviation of 0.16; in pH = 7 buffer solution is 37.2 mV/pH with a standard deviation of 10.66 mV, which presents ΔpH = 0.63 with a standard deviation of 0.18; in pH = 10 buffer solution is 52.4 mV/pH with a standard deviation of 17.01 mV, which presents ΔpH = 0.89 with a standard deviation of 0.29; in pH = 13 buffer solution is 4.4 mV/pH with a standard deviation of 1.57 mV, which presents ΔpH = 0.07, with a standard deviation of 0.03.

The hysteresis of the large Cr-Au electrode in pH = 1 buffer solution is 23.9 mV/pH with a standard deviation of 17.66 mV mV, which presents ΔpH = 0.43 with a standard deviation of 0.33; in pH = 4 buffer solution is 45 mV/pH with a standard deviation of 17.00, which presents ΔpH = 0.79 with a standard deviation of 0.31; in pH = 7 buffer solution is 142.2 mV/pH with a standard deviation of 22.62 mV, which presents ΔpH = 2.53 with a standard deviation of 0.46; in pH = 10 buffer solution is 159.1 mV/pH with a standard deviation of 29.76 mV, which presents ΔpH = 2.84 with a standard deviation of 0.59; in pH = 13 buffer solution is 14.9 mV/pH with a standard deviation of 8.87 mV, which presents ΔpH = 0.26, with a standard deviation of 0.15.

In conclusion, the electrodes with small sensing area shows the lowest hysteresis for all the pH levels. The Hysteresis increases when the sensing area increases, especially in the alkaline environment. The hypothesis is that the micro-structure of the IrOx on the small electrode surface is better than that of the large electrode since the IrCl4 solution distributed more evenly on a small area in the dip-coating process. Hence with the current fabrication technique, to achieve a pH sensor with low hysteresis a small sensor size is preferred. Similar as the previous section, the hysteresis in the alkaline environment is larger than that in the acidic environment, the presence of a high concentration of OH^-. However, the hysteresis in pH = 13 is lower than that in the acidic condition, this phenomenon is yet to be investigated in the future.

4.6. Study of the Interference Effect: Integrated pH and Sodium Sensor Array

4.6.1. Introduction

Nowadays, with the increasing needs of pH related detections, the study on the performance of various types of pH sensors has been wildly investigated, including the conventional glass-rod pH sensor and the ion-sensitive field effect transistor pH sensors [4.23]. Many of them have been used in commercial applications, such as biological and water quality monitoring, food processing, and chemistry detection. However, in such applications neutral salts usually exist in the environments, which lead to non-negligible influence on the accuracy of pH detection, as investigated in [4.36]. Based on the study, the effect of the neutral salt is a function of the ionic strength inside the solution. These sensors then have technical limitations in overcoming the interferences issue for pH measurements. Hence, solving the interference issue is one of the key tasks to guarantee the reliability of pH measurement.

Several attempts have been tried to solve the interference issues. The studies on the calibrations of the pH glass-rod electrode, ISE electrodes, and buffers have been reported [4.37]. The pH glass electrode has a limitation that it absorbs or reacts with the ions at high concentrations. Some reported such pH sensors need to be calibrated at least 2 points close to the expected pH of the sample every 2-3 hours. This makes the sensors unsuitable for commercial applications as it would be difficult to judge the expected sodium concentrations ahead of time. It is inconvenient to calibrate the sensors with accurate pH buffers frequently before the measurements.

Another attempt is applying adequate methodologies to determine the concentrations of the interferences inside the solution [4.38]. In this section, we proposed a three-channel detection and calibration system based on iridium oxide sensing film. A sensor array consisting of an iridium oxide pH sensor, a membrane-based sodium sensor and printed silver chloride reference electrodes was designed and fabricated. Iridium oxide is an attractive material for sensing electrodes since it provides stable responses [4.39] and biocompatibility. The high sensitivity and

low temperature coefficient make it a suitable material for ion-selective electrodes. We demonstrate that the sodium sensor can be used to calibrate the pH sensor simultaneously during pH measurement. The interference issue was greatly reduced by real-time in-situ calibration.

4.6.2. Fabrication and Measurements

4.6.2.1. Fabrication of the IrOx pH Sensing Electrode

The iridium oxide pH sensing electrode was fabricated with the sol-gel technique as described in section 4.3. Briefly, an ultra-flexible 25-μm thick polyimide film coated with 900-Å gold was used as the substrate. This substrate provides a working temperature up to 400°C, which makes it suitable for the thermal process. The flexibility of the substrate can be found in section 5.1. The ultra-flexible Au film was cut to 1×10 mm^2 strips.

The sol-gel solution was prepared by mixing 1-g iridium (IV) chloride powder (Sigma) with 42-mL 200 Proof Ethyl Alcohol (Decon Labs Inc.) and 10-ml 80% acetic acid (Sigma). The mixture was stirred for 2 hours before use. After preparing the sol-gel solution, a dip-coating process was conducted on the ultra-flexible Au strips. Then a thermal treatment was conducted to transform the iridium-based compound in the precursor to crystalline iridium oxide. The coated strips were baked on the hot-plate from 25°C to 325°C in 3 hours, maintained at 325°C for 4 hours, and then cooled down to the room temperature.

Compared with our previous work, the Au film was patterned before conducting the sol-gel and thermal processes. By processing the electrode individually, the uniformity of the sensing film was improved hence providing a better pH sensitivity.

4.6.2.2. Fabrication of the Sodium Ion Sensing Electrode

The fabrication of the sodium ion sensing electrode is based on the IrOx film. A sodium selective membrane is coated on the sensing surface of the aforementioned IrOx electrode. To fabricate the sodium ion sensing membrane, we choose to use the sodium ionophore VI (B12C4) as the ion selective material. The advantage of the B12C4 over other materials is that it contains 12 carbon atoms which attract Na +. The distance between the 2 rings of the B12C4 equals the

size of a sodium ion, which makes it selective to Na+. Also, the B12C4 is stable and can be kept in room temperature. The molecular structure of the B12C4 is shown in Figure 4-21 (a). Figure 4-21 (b) shows a sodium ion being captured by B12C4. The lipophilic salt used here is Na-TFBD. The colloid we used to form the membrane is poly carboxylate (PVC-COOH) and bis (2-ethylhexyl) sebacate (DOS).

To prepare the sodium ion selective membrane, 550-mg poly carboxylate (PVC-COOH) was mixed with 8-mL tetrahydrofuran and ultrasonicated for 30 minutes; 1.2-mL bis (2-ethylhexyl) sebacate (DOS) was added to the mixture and ultrasonicated for 10 minutes; and finally 50-mg sodium ionophore VI (B12C4) and 167-mg lipophilic salt (Na-TFBD) were added to the mixture and ultrasonicated for another 30 minutes. The mixture was then absorbed onto the sensing surface of the IrOx electrode and rested for 24 hours at the room temperature for stabilization [4.40]. All of the mentioned materials in this section were purchased from Sigma. The side view of the sodium ion sensing electrode is shown in Figure 4-22.
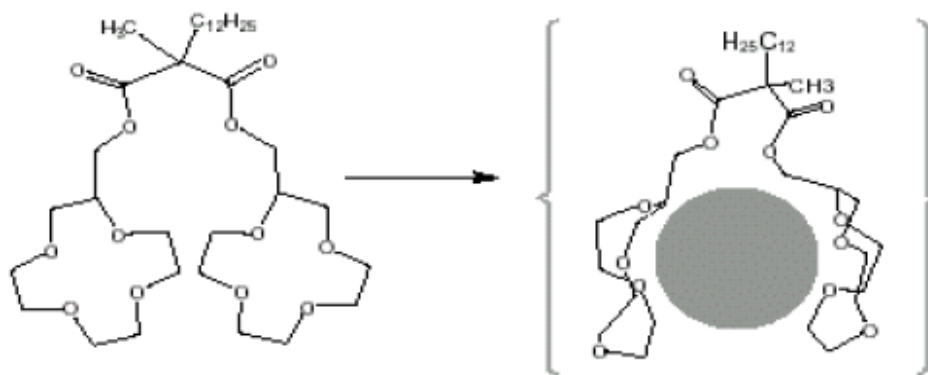
Figure 4- 21. Graphs of (a) the molecular structure of the B12C4, and (b) the sodium ion being captured by B12C4

84
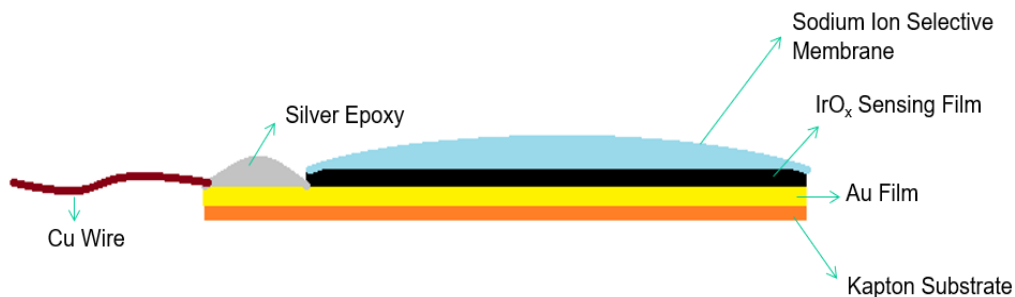
Figure 4- 22. The side view of the sodium ion sensing electrode

4.6.2.3. Fabrication of the AgCl Reference Electrode

Printed silver chloride electrode is used as the reference electrode. An ultra-flexible Au strip with the same size of the IrOx electrode is cleaned by acetone and dried by pressurized air. Appropriate amount of the AgCl paste (CH Instruments, Inc.) is printed over the Au strip and then heated at 125°C for 15 minutes for stabilization.

4.6.2.4. Working Mechanism and Measurement Procedures

As shown in Figure 4-23, the electrode array was fabricated by integrating one IrOx pH - sensing electrode, one sodium membrane modified sodium-sensing electrode, and two AgCl electrodes on a polyimide substrate with an equal distance of 2 mm. Copper wires were connected to the electrodes by silver epoxy. AgCl electrode #1 was used as the common reference electrode for both the IrOx and sodium-sensing working electrodes. AgCl electrode #2 was tested against the AgCl electrode #1 to cancel the noise signals. A three-channel detection system was built in the following way:

- Channel 1 functioned as the pH detecting system, which collected the potentials generated between the IrOx working electrode and the AgCl electrode #1 reference electrode.

- Channel 2 functioned as the sodium detecting system, which collected the potentials generated between the sodium working and the AgCl #1 reference electrodes.

- Channel 3 functioned as the noise cancelation system, which collected the signals generated between the AgCl electrodes #1 and #2.
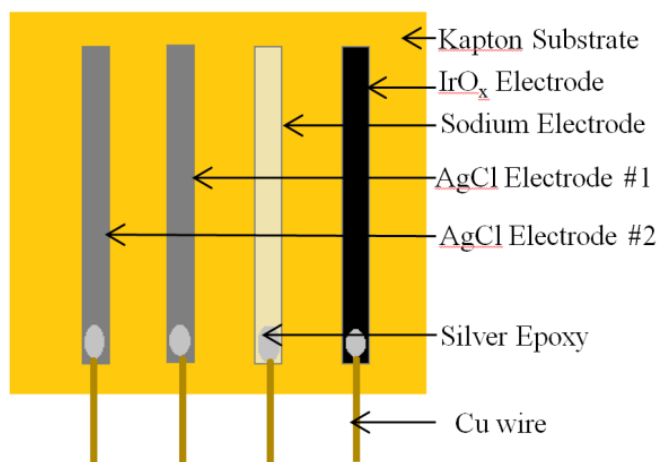
Figure 4- 23. Configuration of the pH sensing electrode, sodium-sensing electrode, and the AgCl reference electrode array.

Standard pH buffer solutions (pH = 4, 7 and 10) were tested for the 3-channel system. Then sodium was added to the standard pH buffer solutions to increase the sodium concentration from 0.1 to 1 M. The 3 channels were tested with the pH buffer solutions containing different sodium concentrations simultaneously. A data acquisition card (NI DAQ-609) with a LabVIEW-based program were used to record the real-time potentials at a 7.5 S/s sampling rate. The data obtained from the channel 1 revealed the performance of the pH sensor and the influence from the existing ion interference. Data obtained from the channel 2 was to detect the sodium ion concentration inside the pH buffer solutions with different pH levels. The pH-sensing result obtained from the channel 1 was calibrated by the data obtained from the channel 2 and the results were compared with those from commercialized pH sensor.

4.6.3. Results and Discussions

4.6.3.1. Performance of the IrOx pH Sensor

The results from the channel 1 indicated the performance of the IrOx electrode. The sensor was tested with standard pH buffer solutions (pH = 4, 7, and 10) with added sodium ion with concentration from 0.1 to 1 M respectively. As shown in Figure 4-24 (a), (b) and (c), the potential increased correspondingly in pH 4, 7, and 10 buffer solutions. The constant step-increase of the potential indicated that the output of the IrOx working electrode was considerably influenced by the existence of sodium ion. Increasing the sodium ion concentration from 0.1 to 1 M, the potentials are increased by 93.8 mV, 105.3 mV, and 67.2 mV for pH = 4, 7, and 10
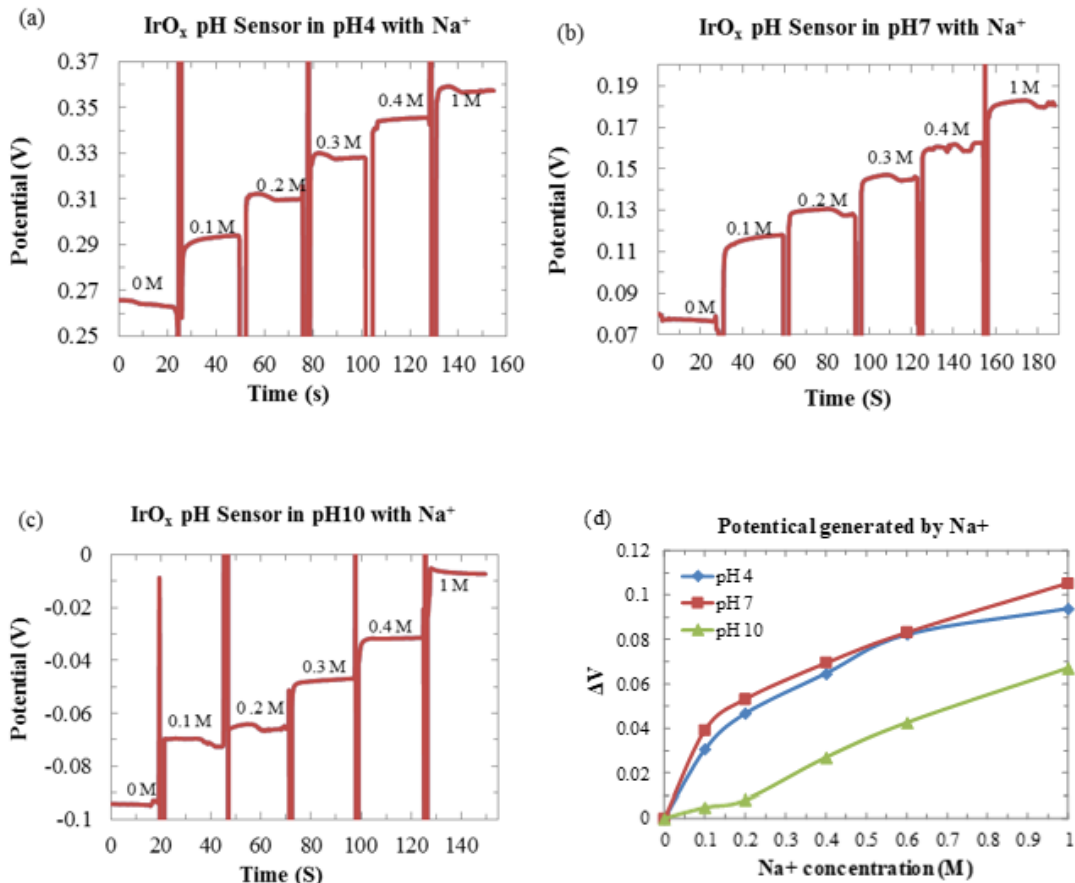
Figure 4- 24. Potential increases of the IrOx electrode generated by increasing the concentration of sodium ion in pH = (a) 4, (b) 7, and (c) 10 buffer solutions. (d) Comparison of the potential increases in pH =4, 7 and 10 buffer solutions.

respectively. The results show the influence of the sodium ion is not uniform or linear, and becomes more severe in the acid and neutral solutions than in the alkaline solution, as shown in Figure 4-24 (d).

The pH sensitivities of the IrOx electrode with different concentrations of sodium are shown in Figure 4-25. Apart from the potential drifts due to sodium ion, the sensor shows linearity with no obvious sensitivity change. The sensitivities are 59.6, 60.5, 62.7, 62.5, 62.8 and 60.7 mV/pH for the sodium ion concentrations of 0, 0.1, 0.2, 0.4, 0.6 and 1 M, respectively.

A commercialized pH sensor (AI312, Apera Instruments) as shown in Figure 4-26 (d) was used with the same pH buffer solutions for comparison. The commercialized pH sensor showed pH discrepancies of –0.51, –0.63, and –0.36 for pH = 4, 7, and 10 when the sodium ion concentration increases from 0 to 1 mM, as shown in Figure 4-26 (a), (b) and (c). Since the discrepancies of pH values varied, it was expected the sensitivity slopes changed. By comparison, the IrOx electrode sensitivity was not influenced by sodium ion but only with potential drifts, so a calibration for the sodium ion existence would be needed to achieve accurate pH detection.
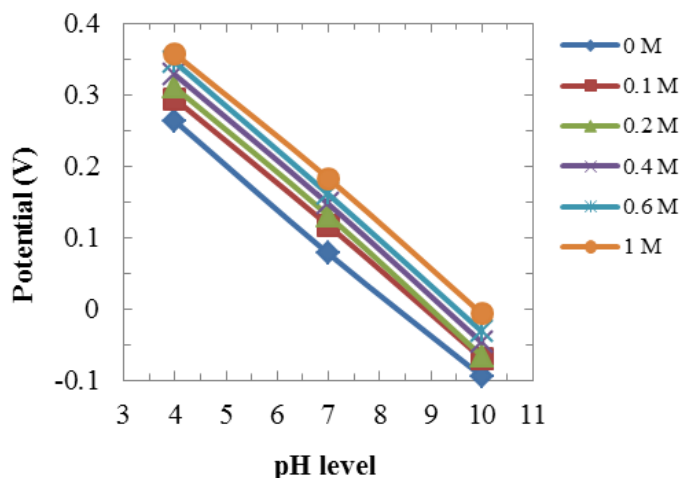
Figure 4- 25. Sensitivity of the IrO$_x$ electrode with different concentrations of sodium ion in the pH buffer solutions.
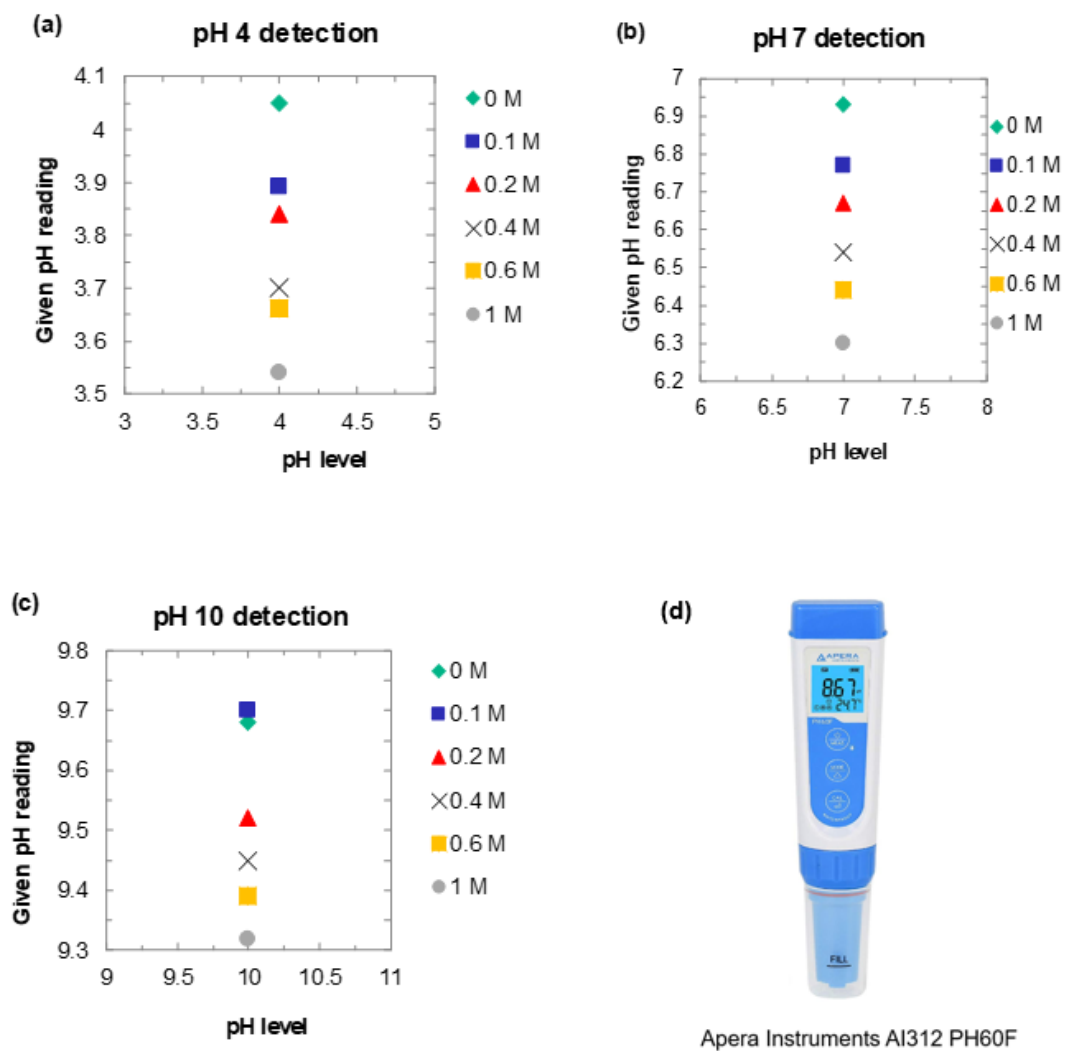
Figure 4- 26. pH reading of the commercial pH sensor as shown in (d) with different concentrations of sodium in pH = (a) 4, (b) 7, and (c) 10 buffer solutions.

4.6.3.2. Performance of the Sodium Ion Sensor

The sodium ion sensor was tested simultaneously with the IrOx pH sensor in the standard pH buffer solutions with or without the addition of sodium ion. The results of the sodium ion sensor are shown in Figure 4-27. By increasing the sodium ion concentration from 0 to 1 M, the sensor shows consistent potential increases of 113.2, 107.5, and 71.4 mV for pH = 4, 7, and 10, respectively. Figure 4-28 shows the performance of the sodium ion sensor in pH = 4, 7, and 10

conditions at different sodium ion concentrations. Comparing with Figure 4-25, the sodium ion sensor shows no response to pH variations when no sodium ion was in the solutions.

In acid or neutral conditions, the sensitivities were higher than that in alkaline. The sensitivity of Na+ in pH =4 buffer solution is 98.6 mV/M; in pH =7 buffer solution is 92.2 mV/M; and in pH =10 buffer solution is 64.8 mV/M. The potential difference for 1-M sodium ion between pH 4 and 7 was 7 mV. The potential difference for 1-M sodium ion between 4 and 10 was 42.1 mV; while they were 1.3 mV and 0.3 mV, respectively, for 0 M. The potential differences between different pH levels with respect to different Na+ concentrations are shown in Table 4-5.
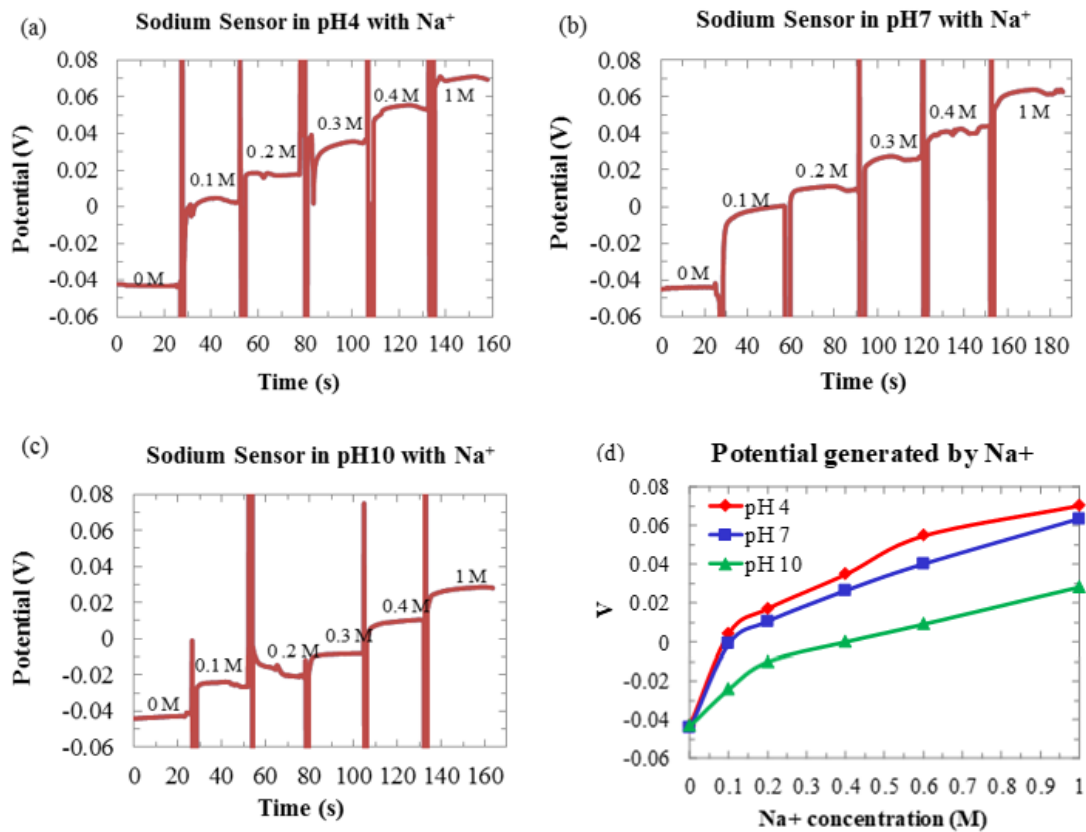
Figure 4- 27. Potential increases of the sodium ion sensor generated by changing the concentrations of sodium ion in pH = (a) 4, (b) 7, and (c) 10 buffer solutions. (d) Comparison of the potential increases in pH =4, 7 and 10 buffer solutions.

Basically, the sodium ion sensor is not pH sensitive. The potential increases after with different concentrations of sodium ion may be caused by the different amount of preexisting Na+ in the pH buffer solutions.
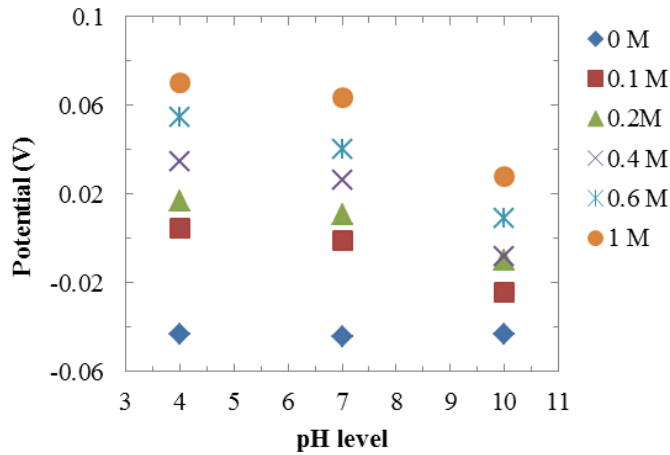
Figure 4- 28. Performance of the sodium ion sensor in pH = 4, 7, 10 buffer solutions.

Table 4- 5. The potential differences between different pH levels with respect to different sodium ion concentrations.

	0M	0.1M	0.2M	0.4M	0.6M	1M
ΔV between pH4 and pH7	1.3 mV	5.4 mV	6.6 mV	8.5 mV	14.7mV	7 mV
ΔV between pH4 and pH10	0.3 mV	28.5mV	27.1mV	43.1mV	45.6mV	42.1mV
ΔV between pH7 and pH10	1 mV	23.1mV	20.5mV	34.6mV	30.9mV	35.1mV

The average responding time of the sodium ion sensor is around 4 seconds. As shown in Figure 4-29, the responding time was defined as the time period from the beginning of the measurement until the potential reach to 90% of the saturated voltage value.
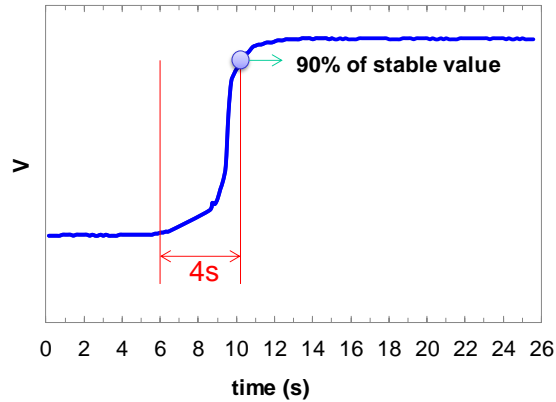
Figure 4- 29. Demonstration of the responding time of the sodium sensor.

A commercialized sodium ion sensor (HORIBA B-721 Compact Salt Meter) was used with the same pH buffer solutions for comparison. Photo of the commercial sodium ion sensor is shown in Figure 4-30 (b). The commercialized sodium ion sensor showed severe sodium ion concentration discrepancies in acidic and alkaline conditions when the sodium ion concentration increases from 0 to 1 M, as shown in Figure 4-30 (a).
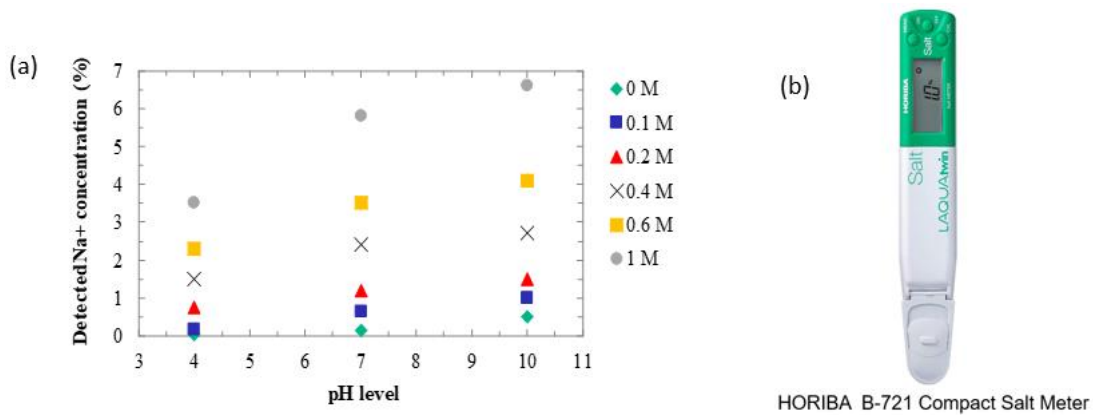
Figure 4- 30. (a) Sodium concentration reading of the commercial sodium sensor with different concentrations of sodium ion in pH = 4, 7, and 10 buffer solutions. (b) Photo of the commercial sodium sensor.

4.6.3.3. Performance of the AgCl Electrode

The potential between the two AgCl electrodes are recorded simultaneously with the IrOx pH sensor. The result of the AgCl electrodes is shown in Figure 4-31. By increasing the sodium ion concentration from 0 to 1 M, the electrodes show no potential increases in the pH buffer solutions. The result indicates the AgCl electrode is not influenced by the existence of sodium ion. The AgCl electrode is not influenced by different pH levels either. Hence, the AgCl electrode can be used as a reliable reference electrode in the pH or sodium ion measurement.
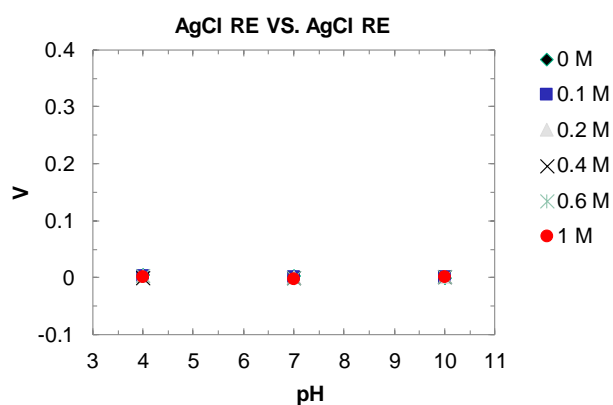
Figure 4- 31. Potential between the two AgCl electrodes with different concentrations of sodium ion in pH = 4, 7, and 10 buffer solutions.

4.6.3.4. Calibration Results of the Sensor Array

The channel 3 recorded the electrical noises induced by electromagnetic coupling in the conductive solution. The noises were eliminated from the channels 1 and 2 by subtracting the signals from the channel 3.

As described, the data obtained from the sodium ion sensor are used to calibrate the results of the IrOx pH sensor. For pH = 4, to obtain the calibrated potential with 0.1-M sodium ion, first the potential difference of the sodium ion sensor between 0 and 0.1 M was extracted. Then the potential difference was subtracted from the signal of the IrOx electrode with the sodium ion concentration of 0.1 M. The calibrated result of pH = 4 was obtained by repeating the extract-

subtract procedure for 0.2, 0.4, 0.6, and 1 M. The same method was done for pH = 7 and 10 signals.

Figure 4-32 shows the calibrated result of the IrOx sensor. Comparing with Figure 4-25, the interference issue was greatly reduced. The calibrated result shows constant potential for each pH level with little influence from sodium ion. The potential variances between 0-M and 1-M sodium ion for pH = 4 buffer solution is reduced from 93.8 mV to 20.1 mV; for pH = 7 buffer solution is reduced from 105.3 mV to 2.2 mV; for pH = 10 buffer solution is reduced from 67.2 mV to 15.8 mV. Thus, the pH values can be more accurately mapped from the produced potentials.
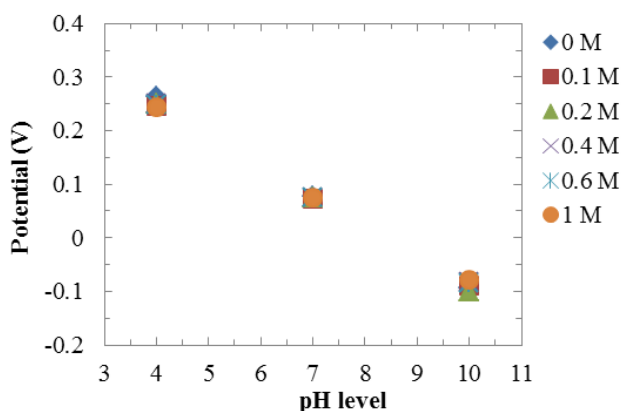
Figure 4- 32. Calibration result of the IrO$_x$ electrode in pH = 4, 7, 10 with the existence of differenct concentrations of sodium ion.

4.6.4. Conclusions

In this section, we have developed a sensor array consisting of an iridium oxide electrode for pH measurement, an IrOx-based ion-selective sensor for sodium ion detection, and two silver chloride reference electrodes. The planar sensor array was fabricated on a flexible substrate with simple fabrication processes. The iridium oxide sensing film was synthesized by the sol-gel process. The sodium ion sensor was fabricated by deposition of a sodium-selective membrane on the iridium oxide film. The silver chloride reference electrodes were made by printing.

The sensor array was tested in standard pH buffer solutions with or without the existence of sodium ion. In both scenarios, a promising sensitivity of 61.46 mV/pH in the pH ranges from acid to alkaline at the room temperature was achieved. The sensor array was tested with standard pH buffer solutions with different sodium concentrations and the interference issue was investigated. The potential increases induced by the sodium ion interference were calibrated by the sodium ion sensor. The three-channel design and calibration procedures greatly reduced the interference effect and showed excellent pH responses.

The fabrication is based on the planar sol-gel technique, which provides the advantages of low cost and reliable device performance. The flexibility of the sensor array also makes it suitable for the applications requiring high conformability such skin or tissue monitoring. The pH and sodium ion sensor-array demonstrates a unique capability to provide accurate pH detection in the environment containing sodium ion interference.

4.6.5. Future Works

4.6.5.1. Interference Effect for Potassium Ion

A Cr-Au IrOx electrode is fabricated to investigate the influence of the potassium ion on the iridium oxide pH sensor. The pH sensor is tested in standards pH buffer solutions mixed with different concentrations of potassium ion from 0.1 to 1 M in the sequence from pH 2 to 13, then back to pH 2. The result is shown in Figure 4-33 (a)-(e). The potential for the pH 2, 4, 7, 10 and 13 buffer solutions increased correspondingly, indicating the output of the IrOx working electrode is influenced by the existence of potassium ion. Increasing the potassium concentration from 0.1 to 1 M, the potentials are increased by 52.4 mV, 62 mV, 85 mV, 51 mV, and 47 mV for pH = 2, 4, 7, 10 and 13 respectively. The results show the influence of the potassium ion is not uniform or linear, and becomes more severe in the neutral solution. The pH sensitivities of the IrOx electrode with different concentrations of potassium ion are shown in Figure 4-33 (f). Apart from the potential drifts due to potassium ion concentrations, the sensor shows linearity with no obvious

sensitivity change. The sensitivities are 61.3, 61.5, 62.4, 62.5, and 62.8 mV/pH for the potassium

ion concentrations of 0.1, 0.2, 0.4, 0.6 and 1 M, respectively.
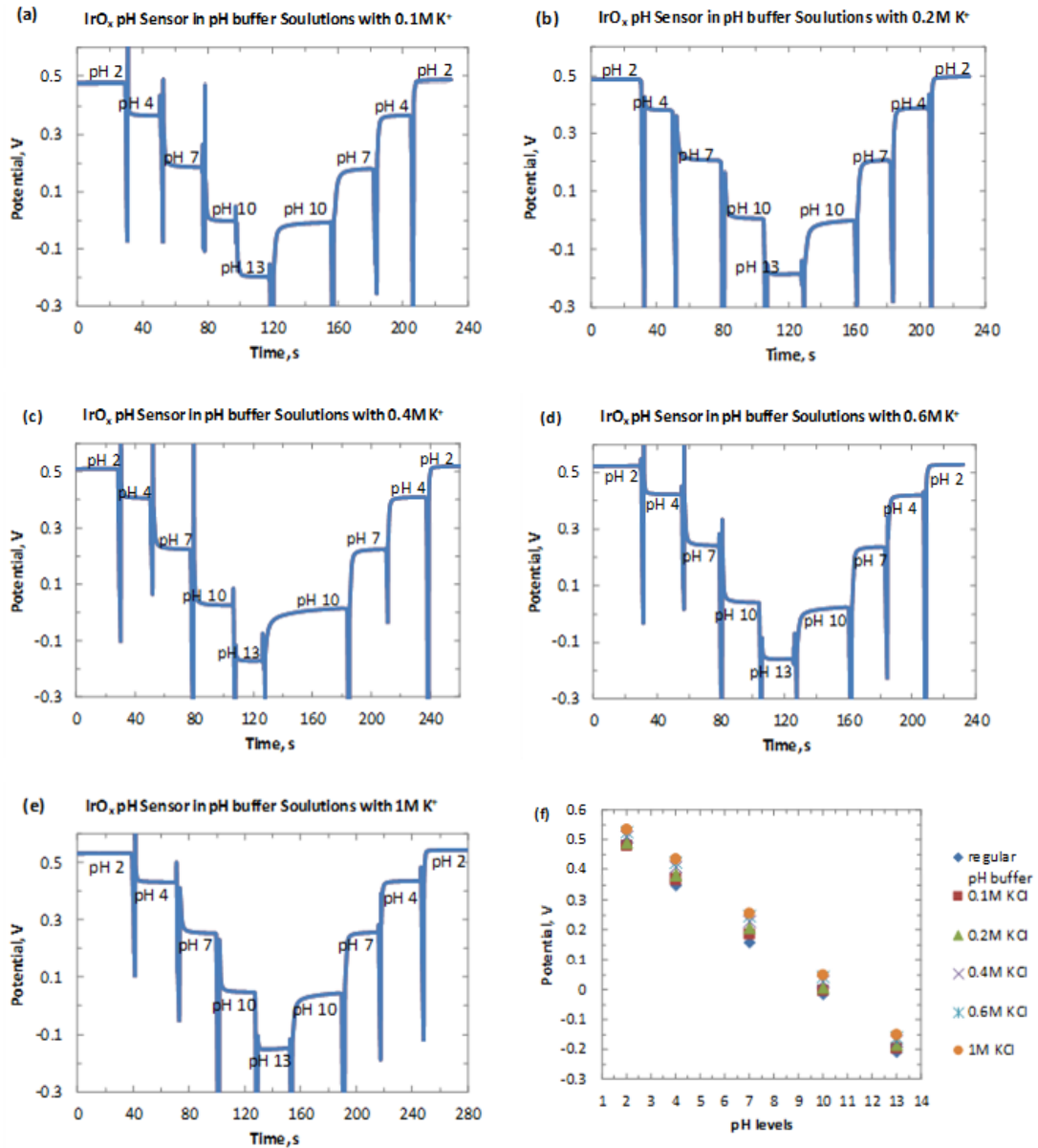
Figure 4- 33. (a)-(e): Potential response of the potassium ion sensor pH = 2, 4, 7, 10, and 13 buffer solutions with increasing potassium ion concentration. (f): Sensitivity of the IrO$_x$ electrode with different concentrations of potassium ion in the pH buffer solutions.

4.6.5.2. Fabrication of the Potassium Ion Sensor

Similar as the previous section, to calibrate the pH sensor we proposed a potassium ion sensor. The fabrication of the potassium ion sensing electrode is based on the IrOx film. A potassium ion selective membrane is coated on the sensing surface of the IrOx electrode. To fabricate the potassium ion sensing membrane, we choose to use the valinomycin as the ion selective material. The advantage of the valinomycin over other materials is that it contains negative oxygen and N, which attract K^+. The size of the ring hole of valinomycin equals to the size of a potassium ion, which guarantees the selectivity. The disadvantage of valinomycin is that it needs to be kept in 4°C and the device is not suitable for long time testing in room temperature. The molecular structure of the valinomycin is shown in Figure 4-34. The lipophilic salt used here is potassium tetrakis [4-chlorophenyl] borate (K-TpClPB). The colloid we used to form the membrane is hydro-aliphatic urethane diacrylate (polyurethane EB2001) and photoinitiator TPO (Chivacure®).
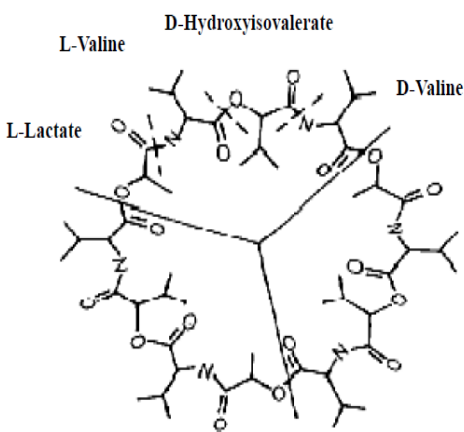
Figure 4- 34. Molecular structure of the valinomycin.

To prepare the potassium ion selective membrane, first 0.1g polyurethane EB2001 is mixed with 0.02g TPO in 1ml THF and ultrasonicate for 30 minutes. Then 33 μL of the mixture is

mixed with 6 mg of valinomycin and 3mg of K-TpClPB and ultrasonicate for 30 minutes in warm water bath. Finally, appropriate amount of the mixture is applied to the electrode and then exposed to UV (350 nm) light for 60s for stabilization [4.40]. The side view of the potassium ion sensing electrode is shown in Figure 4-35. The performance of the potassium ion sensing electrode will be investigated in the future.
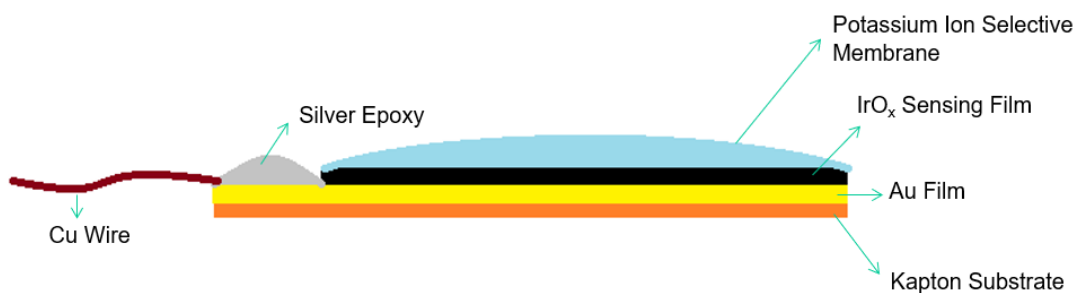
Figure 4- 35. The side view of the potassium ion sensing electrode.

Chapter 5

SKIN pH MEASUREMENT WITH AN ULTRA-FLEXIBLE I$_R$O$_X$-BASED SENSOR

5.1. Introduction

Nowadays, pH measurement has been validly investigated in the field of skin caring. Recent study shows that the optimal skin pH level keeps the skin looking radiant and resists harmful bacteria. However, certain factors such as unbalanced diet, hormones changes, consumptions of tobacco and alcohol, and even stress could lead to a skin pH level changes, leaving a dry and sensitive skin which is prone to spots or irritation. By detecting the accurate daily skin pH level, one could apply appropriate lotions, supplement or medicine accordingly to adjust the skin to the optimal pH level and hence maintain a healthy skin.

The relationship between skin pH levels and antimicrobial effects that prevent microorganism growths has been studied. More comprehensive results later validate the relationship with updated techniques of sensing pH [5.1−5.4]. Since pH values are measured as H+ ion concentration in liquid, the existence of water is needed on the skin for measurements. It presents difficulty for experimental protocols, repeatability and reliability of recorded signals in practical cases for human. The newer techniques with hand-held or tabletop pH sensors and protocols associated with them overcome some of the issues making recent clinical data more robust, however, still present technical challenges and practicality for wearables to monitor and record skin pH in continuous and comfortable fashions.

Healthy and undamaged skin of adults is slightly acidic in the range of 4 to 6, depending on anatomical parts, physiological factors such as circadian rhythm and age, and external factors such as humidity, temperature and exposure to environment [5.5−5.8]. The skin pH and aging of skin are also closely related [5.9−5.11] including wrinkle formation [5.12, 5.13] and skin microbiome effects [5.14].

The current measurement protocols are within controlled experimental environments that target understanding of basic mechanisms but are not suitable for frequent and continuous

99

monitoring of skin while subjects resume regular activities without constraints. Comparing to the historic cases in which utilizing better methods for skin pH measurements have enabled better comprehension of relationship between pH and skin, it is clear that a new tool, which can address the current constraints, can further the knowledge of dynamics and changes of skin biochemistry related to physiological parameters. For example, one can gather data to understand the skin conditions affected by diet, exercise, environments and even emotions for individuals by correlating multi-modality data if the skin pH values can be continuously monitored comfortably without affecting subject's mobility.

The conventional commercialized skin sensors have the disadvantage of bulky design, which made them not suitable for skin wearing. In this section, we developed an ultra-flexible pH sensor for skin pH detection. The miniature size and the excellent conformity to skin tissues give it great advantages over the conventional skin sensors.

The ultra-flexible pH sensor consists of IrOx and AgCl electrodes based on ultra-flexible substrates with robust performance and simple fabrication processes. The ultra-flexible substrates can be easily folded, twisted, warped or contorted to conform onto curvature surfaces.

The pH sensor was first tested in flat and deformed conditions. In both scenarios, it showed a promising sensitivity of 49.3 mV/pH in the pH range between 2 and 13 at the room temperature. The response time, stability, reversibility, and repeatability of the sensors were investigated in both physical conditions. No decrease was observed in sensitivity or responsibility when the sensor was deformed.

Then, the flexible pH sensor was tested on skin. A commercialized skin pH sensor was tested along as comparison. For the skin measurement, our sensor shows promising sensitivity and responsivity. The ultra-flexible pH sensor shows unique capability to be conformed to curved surfaces while provides excellent performance. With the good flexibility and reliable responses, our ultra-flexible pH sensor is proved to be suitable for skin pH monitoring.

5.2. Sensor Fabrication and Measurements

5.2.1. Sensor Configuration

The ultra-flexible pH sensor consists of two electrodes: the iridium oxide working electrode and the silver chloride reference electrode. The pH value is indicated by the potential difference generated between the working and reference electrodes. Both the working and reference electrodes were made on an ultra-flexible polyimide film and patterned by laser cutting. Figure 5-1 shows a photo of the working and reference electrodes being attached to a 3D printed mold. The Electrical wires were attached onto the gold contact pads on the working and reference electrode stripes by silver epoxy.

5.2.2. IrOx Working Electrode

The iridium oxide working electrodes were fabricated in two major steps. First, by the sol-gel process, a thick iridium oxide sensing layer was formed on the ultra-flexible polyimide film with a thin layer of gold. Then the sensing film was tailored by laser cutting to the electrode shapes. The ultra-flexible substrate (Sheldahl, Multek Corp.) consisted of a 25-µm thick polyimide with double-side 900-Å gold film layers. Typical weight is 36 g/m2. The film has a surface resistivity of 1 Ω/square and a working temperature range up to 400 °C for short intervals.
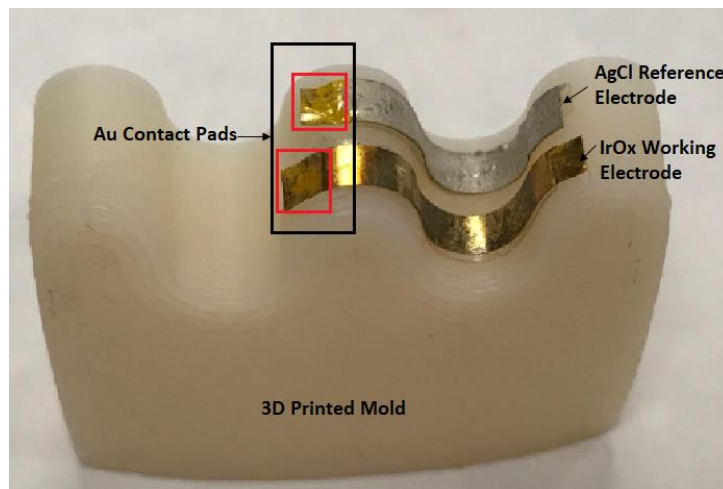
Figure 5- 1. Photo of the ultra-flexible pH sensor being attached to a 3D printed mold.

The iridium oxide sensing film was fabricated by the sol-gel process. The sol-gel precursor was prepared by dissolving 1-g iridium chloride powder into 42-ml ethanol and 10-ml acetic acid. Adding acetic acid is to maintain the mixture at a low pH level to avoid unnecessary chemical reactions. The mixture was stirred constantly with a magnetic stirrer for two hours before use. During the sol-gel process, the ultra-flexible gold film was placed on a carrier and dip-coated with the precursor. The dried film was then undergone a thermal treatment with the temperature increasing from 25°C to 325°C in 3 hours. The temperature was maintained at 325°C for 4 hours and cooled down to 25°C in another 7 hours. After the thermal treatment, the iridium-based compound in the precursor oxidized to crystalline IrOx.

The pH sensing mechanism can be found in Chapter 2. After the thermal oxidation, the ultra-flexible film was released from the carrier and cut by a motor-controlled laser to a desired shape. In this section, the working electrodes were 1×10 mm^2 in size for the ease of handling in liquid tests. Finally, electrical wires were attached onto the contact pads of the working electrode.

Compared with our previous works [5.15, 5.16], the fabrication procedures were greatly simplified by using laser cutting instead of photolithography to reduce the need of three additional photomasks and multiple steps of wet processes in which chemical and mechanical stresses can potentially damage the film and metal patterns. The elimination of additional steps lays a path for low-cost roll-to-roll manufacturing, which can greatly reduce the fabrication costs. After the fabrication, the ultra-flexible film maintained excellent flexibility and conformability, as shown in Figure 5-2. Figure 5-2 (a) shows the working electrode stripe can be twisted without damaging the film. Figure 5-2 (b) shows the electrode stripe can be tightly wrapped around an index finger like a ring.

5.2.3. AgCl Reference Electrode

We fabricated the reference electrodes by printing the AgCl paste (CH Instruments, Inc.) on the ultra-flexible substrate (Sheldahl, Multek Corp.). After cleaning and drying the Au film, the paste was printed on the film and then heated at 125°C for 15 minutes for stabilization. Then film

was cut to a size of 1×10 mm2 stripe by laser. Electrical wires were attached onto the gold contact pads on the electrode stripes.
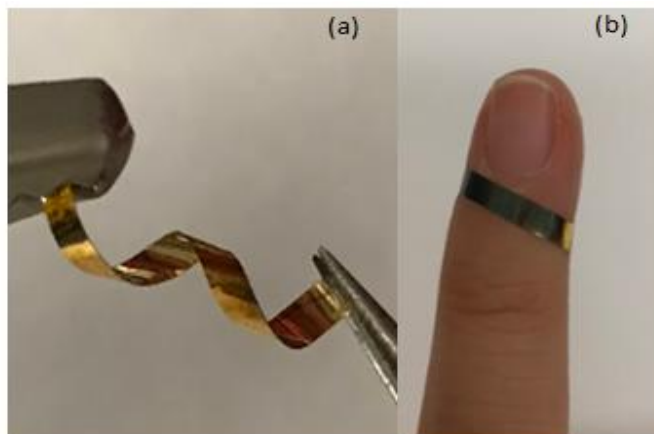
Figure 5- 2. The ultra-flexible sensor (a) was twisted by tweezers and (b) tightly wrapped around an index finger like a ring.

5.2.4. Measurement Procedures

5.2.4.1. Deformation Test

Several experiments were conducted to demonstrate the performance of the pH sensor in the deformed condition. Standard buffer solutions (pH=2, 4, 7, 10, and 13) were used for testing. A data acquisition (NI DAQ-609) card was used for measurements of the potential difference between the working and reference electrodes. A LabVIEW-based program was used to record the real-time potentials. The data were sampled at a rate of 7.5 samples per second. Each pair of the working and reference electrodes were tested in two different conditions, with and without deformation. For deformation, the electrodes were placed firmly onto to 3-D printed molds with dimensions shown in Figure 5-3. The molds had a length L, a height H and a variety of curvature radii R from 3 mm to 10 mm (L = 18 mm and H = 10 mm when R = 3 mm). For small curvature-radius surfaces, the sensor was tugged into the grooves by a human finger thus the film did

experience compressive stress during attachment. Parameters indicating the sensor performances such as sensitivity, reversibility, repeatability, response time and hysteresis were recorded and analyzed in the flat and deformed cases.
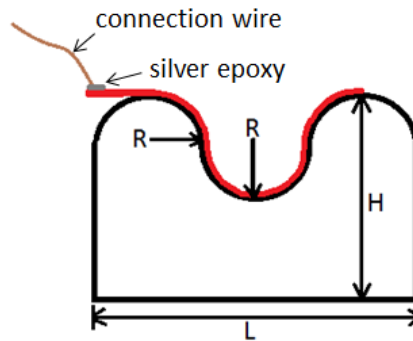
Figure 5- 3. Side-view of the 3-D printed mold for testing a deformed sensor (indicated in red) attached to the surface.

5.2.4.2. Skin Test

The pH sensor was test with standard pH buffer solutions in two conditions: on tissue paper and on skin. A calibration curve was first obtained by testing the sensors inserted inside tissue papers soaked with standard pH buffer solutions. A polynomial relationship between potential and pH was obtained. The skin measurement was conducted by dipping the standard pH buffer solutions on skin and tested by the pH sensors directly. The skin measurement potentials were then calibrated to pH values. A commercialized skin pH sensor was tested along as comparison. The parameters commonly used to define the sensor performance were investigated, such as the stability, repeatability, reversibility, and response time.

5.3. Results and Discussions

5.3.1. Sensitivity

The sensitivity of the sensors in the flat condition was tested by dipping them into the buffer solutions from acid to alkaline. The sensor was tested from pH = 2 until pH = 13, then in a reversed order back to pH = 2. In the cases on deformed curvature surfaces, a pipette was used to apply and retreat the pH buffer solutions on the surface. Each time 200 µl of standard pH buffer solutions was applied to the electrodes. After around 40 seconds the pH solution was withdrawn by the pipette and the solution with another pH level was applied. The electrodes were tested in the same order as that for the flat condition. In all cases, the electrodes were tested 3 times in the same protocol to demonstrate consistency and responses. The sensor surface was not cleaned by deionized water between the buffer solutions, which was mimicking realistic scenarios when sensors encountered pH variations in liquid.

Figure 5-4 (a) shows the sensitivity of the electrodes in the flat condition. The result shows an average sensitivity of 49.3 mV/pH as a Nernstian response with the R2 value of 0.9949. Figure 5-4 (b) shows the sensitivity of the electrodes in the deformed condition with a surface curvature radius of R = 3mm. The result shows the same average sensitivity and responses. These results were obtained from 4 sensors with 12 data sets.

5.3.2. Response Time

Figure 5-5 (a) shows the response times for the sensor in the flat condition. The electrodes were dipped into beakers with different pH buffer solutions. The response time was counted staring when the electrodes were transferred to another beaker until the potentials between the working and reference electrodes stabilized. A low-pass filter was placed to filter out the signal spikes occurred when the sensor initially touched liquid. The plots indicate a longer saturation time is needed for strong acid (pH = 2) and alkaline (pH = 13) solutions. It may be owing to the ion exchanges in the surface pores. Overall the electrodes stabilized quickly within 1 second. Figure 5-5 (b) shows the results for the deformed sensor. The small fluctuations

indicated by red arrows occurred when the pipette was inserted into the liquid. The electrodes in the deformed condition had similar response times. It should be noted that when the sensors were transferred between beakers or during the transition of solution replacement on the sensor surface, the exchange of ions in the film pores and air bubbles on the surface require time to reach an equilibrium state. Thus, the exact response times measured varied. The results shown are from one typical example.
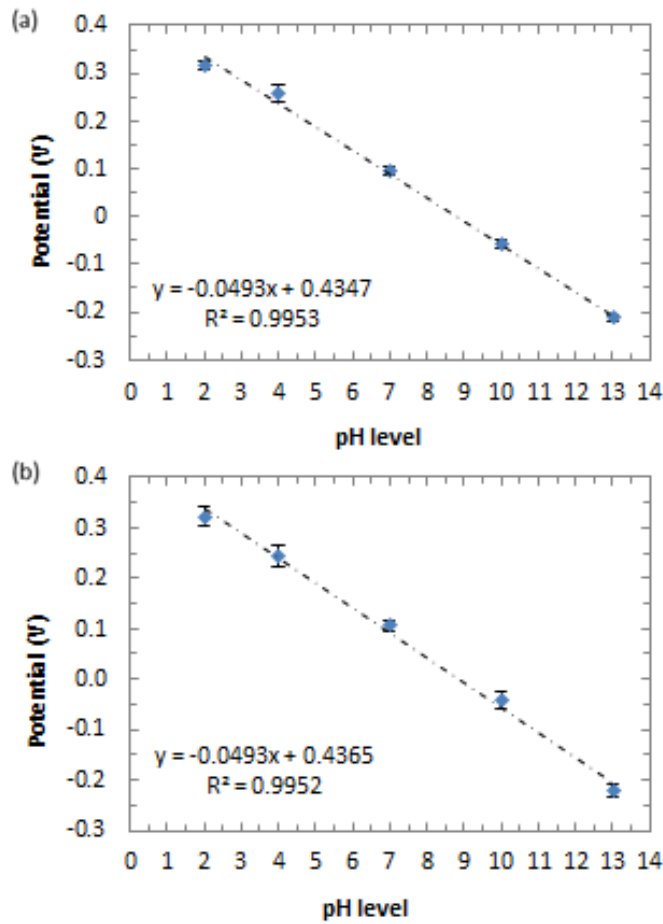
Figure 5- 4. Measured sensitivity of the ultra-flexible pH sensor in the (a) flat and (b) deformed conditions.

5.3.3. Reversibility and Repeatability

The results of reversibility and repeatability for the flat and deformed electrodes are shown in Figures 5-6 (a) and (b) respectively. The potential deviation was defined as the potential difference among tests within the same solution. For the flat condition, potential deviations of 13, 0.9, 4.5, 11.5 and 10 mV were observed in the measurements of pH=2, 4, 7, 10, and 13, respectively. In the deformed state, potential deviations of 30, 17.5, 4.1, 22.5 and 6.9 mV were observed. This phenomenon of larger deviations was probably due to the residue of remaining ions on the surface since it was difficult to remove all solution from the groove with a pipette.
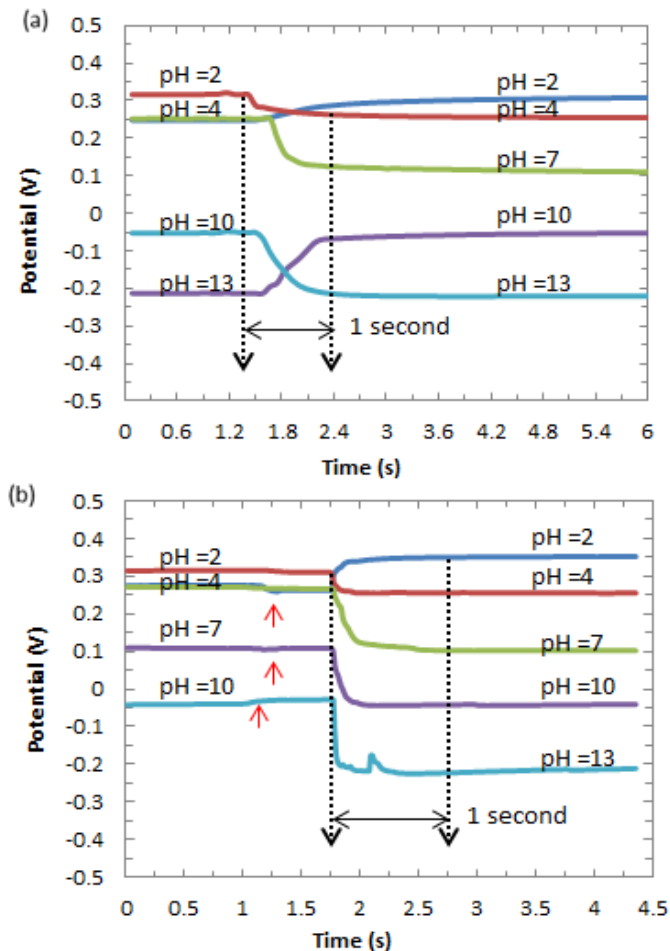
Figure 5- 5. The response times for the sensor in the (a) flat and (b) deformed conditions.

The potential fluctuation was defined as the voltage fluctuation range after the potential started stabilization. In Figures 5-6, larger potential fluctuation was observed when the electrodes were placed on the curved mold (R = 3mm). This was due to the smaller amount of solution applied on the sensor so any hydrodynamic motion would induce noises, compared to the amount of liquid in beakers. Overall the fluctuations throughout the measurements stayed within 6 mV.

Figure 5-6 also demonstrates the repeatability of the ultra-flexible pH sensor. The hysteresis issue is observed in both the flat and deformed states. This phenomenon may due to the ion residue left on the surface, as the sensor surface was not cleaned between tests, which was more palpable in the curved mold as the film was bent. The maximum hysteresis was found to be 35.1, 32, 6.8, 14.7, and 8.1 mV for pH=2, 4, 7, 10, and 13, respectively.
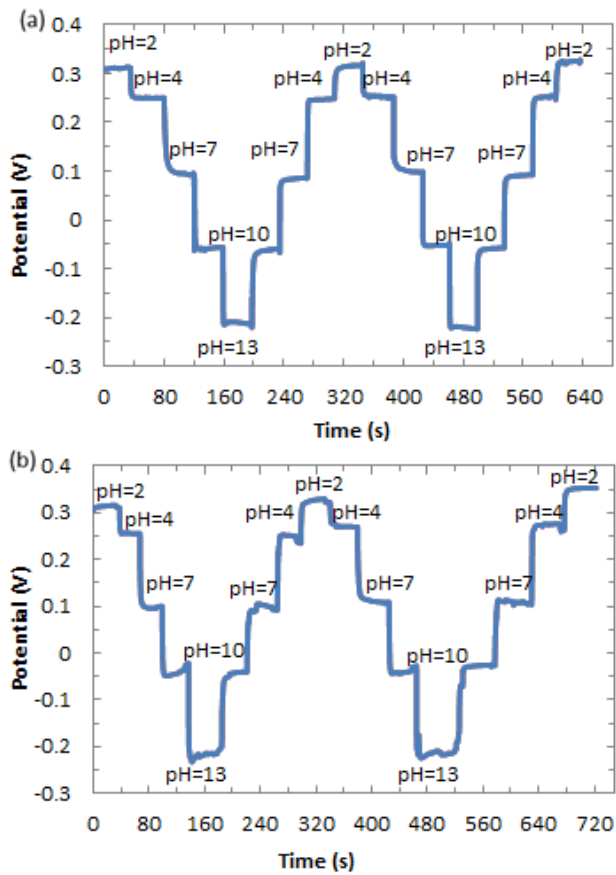
Figure 5- 6. Measured results for the reversibility and repeatability in the (a) flat and (b) deformed conditions with pH varying between 2 and 13.

5.3.4. Skin Measurement Results

Tissue papers were soaked with standard pH buffer solutions pH=5, 6, 7, and 8. The sensors were inserted inside the soaked tissue papers and tested from pH =5 to pH=8, then in a reversed order back to pH=5. The result of the tissue measurement is shown in Figure 5-7. Figure 5-7 (a) shows the continuous step-responses of the sensor to specific pH levels from pH 5 to pH 8, then in a reversed order back to pH 5. Figure 5-7 (b) shows the linearity of the pH sensor with a sensitivity of 28.251 mV/pH. As discussed in section 4.6, the responding time is defined as the time period from the beginning of the measurement until the potential reaches to 90% of the saturated potential value. For the tissue measurement an average responding time of 6.48 s is observed. The average hysteresis for the tissue measurement is 1.3 mV. The experiments were
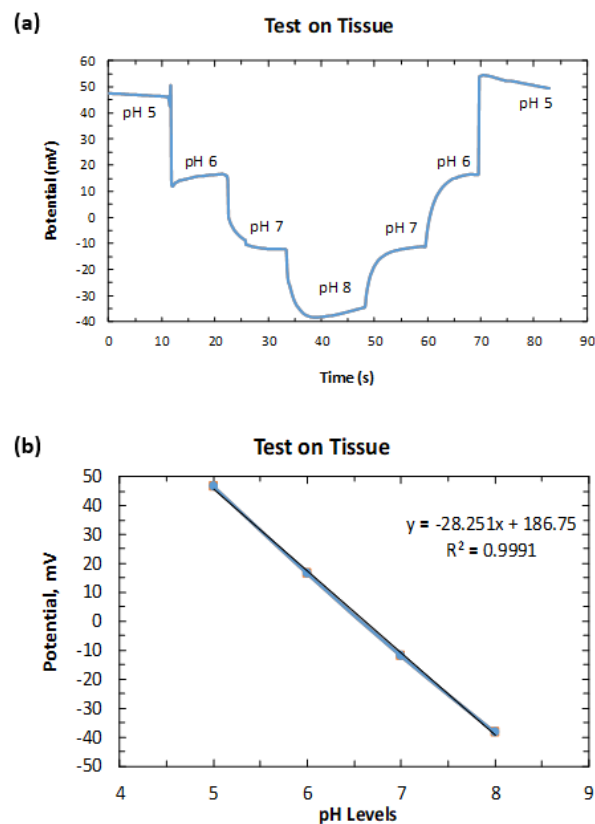
Figure 5- 7. Tissue measurement result shows a linear response
with different pH levels varying between 5 and 8.

repeated three times and same responses were observed, which demonstrates the good repeatability of the sensor.

The skin measurement was conducted by dipping the standard pH buffer solutions on skin and tested by the pH sensors directly. Four pH levels (pH 5, 6, 7, 8) are tested on the back of a hand. The sensor is first tested in the order from pH = 5 to pH = 8, then a reversed-order test is conducted from pH 8 to pH 5 to demonstrate reversibility and stability. The result of the skin measurement is shown in Figure 5-8. The sensor showed stable potential response to each pH level, with little hysteresis. Figure 5-8 (a) shows the continuous step-responses of the sensor to
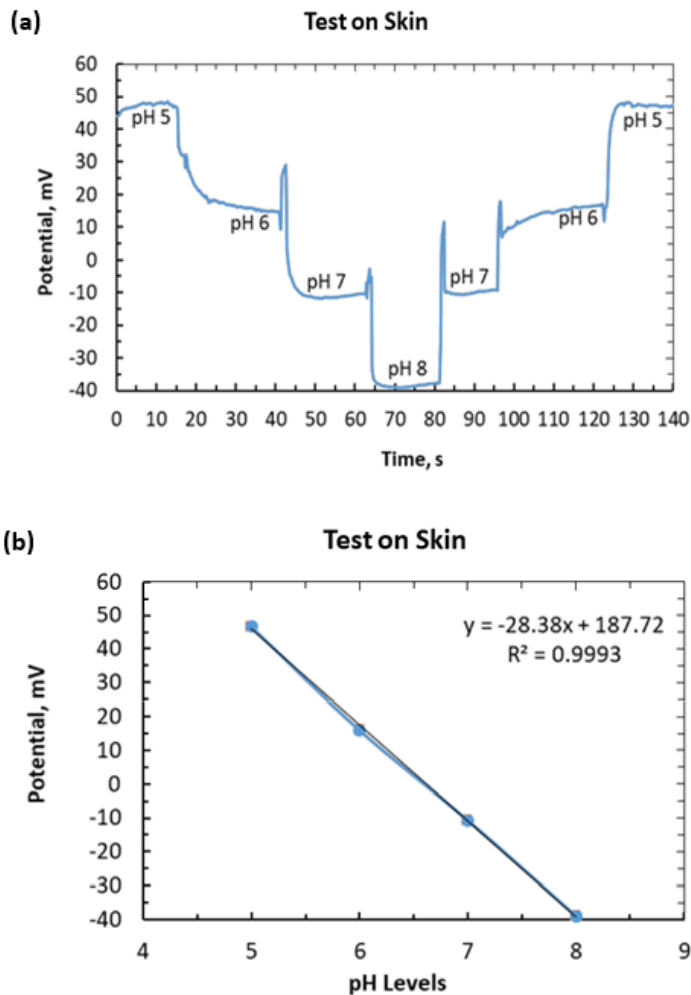
Figure 5- 8. Skin measurement result shows a linear response with pH levels varying between 5 and 8.

specific pH levels from pH 5 to pH 8, then in a reversed order back to pH 5. Figure 5-8 (b) shows

the linearity of the pH sensor with a sensitivity of 28.42 mV/pH. The average responding time of

the skin measurement is 6.62 s. The average hysteresis of the skin measurement is 1.37 mV

A calibration curve between potential and pH was obtained by testing the sensors with

the tissue soaked with different pH levels. The skin measurement potentials were calibrated to

pH values by the tissue measurements. The results were analyzed with the Clarke Error Grid.

The potential output was converted to pH levels. The result shows a linear response with different

pH levels as shown in Figure 5-9. The measured results show a pH difference less than ±0.19

compared with the applied standard pH buffers, which is more accurate than a commercialized

pH sensor (Apera Instruments, AI312 PH60F) with a pH difference of ±0.97.
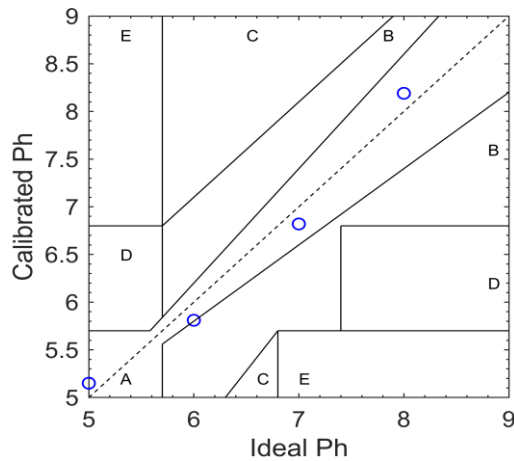
Figure 5- 9. Calibrated skin measurement results by the tissue measurements
and the results were analyzed with the Clarke Error Grid.

A commercialized pH sensor (AI312, Apera Instruments) was tested with pH buffer

solutions (pH 4, 5, 7, and 10) inside a beaker and on skin for comparison. As shown in Figure 5-

10, the blue dots indicate the result tested inside a beaker and the red dots indicate the results

tested on skin. The commercial pH sensor shows accurate pH reading when it is tested inside a

beaker. However, when it is tested on skin the pH discrepancy appears. After signals are

stabilized, discrepancies of 0.71, 1.03, 0.54 and 0.68 for pH = 4, 5, 7, and 8, respectively are obtained. This is possibly due to the built-in averaging mechanism in the commercial device and/or the rigid sensing surface causing the impedance fluctuations between the sensing film and insufficient liquid on the skin. By comparison, the flexible IrOx electrode has a better accuracy when tested in such an environment. For the commercial pH sensor, the responding time for the beaker test is 5 s, while it becomes more than 10 s on skin since the data fluctuate.
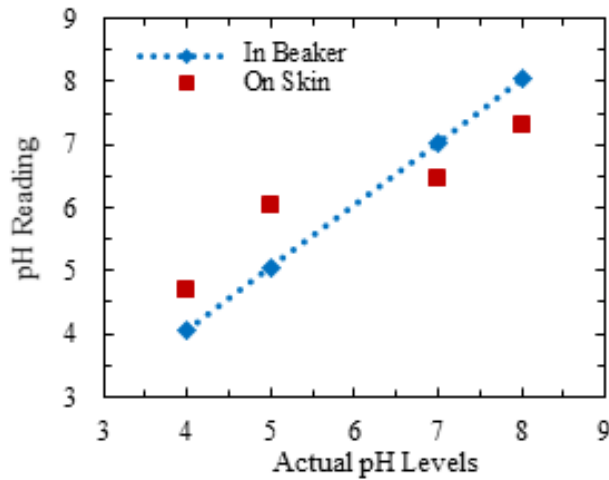
Figure 5- 10. Performance of the commercial pH sensor when tested with standard pH buffer solutions inside a beaker and on skin.

5.4. Conclusions

In this section, we demonstrated an ultra-flexible pH sensor consists of an IrOx working electrode and an AgCl reference electrode for pH measurement on skin. The sol-gel fabrication provides advantages of lower costs, simpler processes and reliable device performance. The pH sensors have been tested for sensitivity, responsivity, reversibility and repeatability in the conditions of being flat and deformed. The reliable performance and flexibility make them suitable for the skin monitoring which requires high conformability. In the skin measurement, the stability, reversibility, responsivity and repeatability were investigated to evaluate the sensor performance.

The miniature size and flexibility provide excellent conformity to skin hence ensures accurate testing results. Comparing with a commercial sensor, our sensing film has the advantages of smaller size, faster responding time, and better accuracy in the testing environment with insufficient liquids. The simple fabrication techniques and reliable performance make it promising for future bio-medical applications.

Chapter 6.

FUTURE WORKS

SWEAT MEASUREMENT WITH AN INTEGRATED MULTI-FUNCTIONAL

I_RO_X-BASED SENSOR-ARRAY

6.1. Introduction

The technique of wearable sensor provides appreciative insights toward personalized medicine through continuous monitoring of the body fluids. Comparing with other biofluids, sweat has become an appealing analyte owing to its easy epidermal availability [6.1]. It also carries abundant biomedical biomarkers related to health assessments and disease diagnoses, such as metabolites [6.2], electrolytes [6.3], and exogenous substances [6.4]. Previously reported sweat based non-invasive biosensors either can only monitor a single analyte at a time or lack the sensor calibration mechanisms for accurate analysis of the physiological state. Given the complexity of sweat secretion, simultaneous and multiplexed screening of target biomarkers is critical and requires full system integration to ensure the accuracy of measurements. [6.3]

Real-time monitoring of sweat can provide immediate information about skin chemistry. Utilizing sweat, instead of applying water discretely, for continuous skin pH evaluation provides advantages of lower costs and implementation ease for healthy individuals. For disease diagnosis, sweat pH is a precursor for detecting alkalosis, cystic fibrosis, cutaneous diseases, and skin dehydration levels [6.5−6.7]. Under normal homeostasis, the sweat pH should be in the range of 4.5−5.5. Skin diseases such as dermatitis and acne change the skin pH levels. For wounded tissues, an increased pH value indicates possible infection by bacterial colonization. Increases in pH can also be related with metabolic alkalosis. These changes are dynamic and time-variant, thus discrete samplings of skin pH without in situ information that can be correlated with other real-time physiological parameters do not provide a complete picture to analyze the skin conditions or diseases.

Apart from pH, there are other sweat compositions indicating abnormal health condition. Sweat lactate can potentially serve as a sensitive marker of pressure ischaemia [6.6]. Excessive loss of sodium in sweat could result in hyponatremia hypokalemia, muscle cramps or dehydration [6.8].

In this chapter we present a flexible and deformable iridium oxide sensor array to be attached on body for multiplexed in-situ sweat analysis, which simultaneously and selectively measures sweat metabolites (lactate) and electrolytes (sodium ion), as well as the skin pH level. In chapter 3, we developed a lactate sensor with a wide lactate acid detecting range, and in Chapter 4 we developed an integrated pH and Na^+ sensor-array for calibrated pH-sensing to distinguish the signals generated by H^+ and Na^+. In this chapter, we developed a multi-functional sensor-array including a lactate sensor, a pH sensor, and a sodium sensor. The flexible sensor-array is tested with artificial sweats.

6.2. Fabrication and Methods

6.2.1. Fabrication of the pH Sensing Electrode

The iridium oxide pH sensing electrode is fabricated with the sol-gel technique as described in section 4.3. Briefly, a flexible 125-μm thick polyimide film coated with 50nm Cr and 200nm Au is used as the substrate. The film is cut to 2×5 mm^2 strips and dip-coated with the sol-gel solution. Then a thermal treatment is conducted to transform the iridium-based compound to crystalline iridium oxide on the strips. A coper connection wire is then connected to the electrode strip with silver epoxy.

6.2.2. Fabrication of the Sodium Sensing Electrode

After the preparation of the IrOx electrode, the sodium membrane is deposited on top of the IrOx sensing film. Briefly, 550-mg poly carboxylate (PVC-COOH) is mixed with 8-mL tetrahydrofuran and ultrasonicated for 30 minutes; 1.2-mL bis (2-ethylhexyl) sebacate (DOS) is added to the mixture and ultrasonicated for 10 minutes; and finally 50-mg sodium ionophore VI (B12C4) and 167-mg lipophilic salt (Na-TFBD) are added to the mixture and ultrasonicated for another 30 minutes. The mixture is then loaded on the the IrOx electrode and rested for 24 hours

at the room temperature for stabilization. A coper connection wire is then connected to the electrode strip with silver epoxy. Detailed information can be found in section 4.6.2.2.

6.2.3. Fabrication of the Lactate Sensing Electrode

After the preparation of the IrOx electrode, the lactate oxidase enzyme is loaded on the IrOx sensing film with a syringe. A coper connection wire is then connected to the electrode strip with silver epoxy. The fabrication details can be found in section 3.2.2.

6.2.4. Fabrication of the AgCl Self-Reference Electrode

The flexible 125-μm thick polyimide strip with the same size of 2×5 mm^2 is cleaned by acetone and dried by pressurized air. Appropriate amount of the AgCl paste (CH Instruments, Inc.) is printed over the strip and then heated at 125°C for 15 minutes for stabilization. A coper connection wire is then connected to the electrode strip with silver epoxy.

6.2.5. The Lamination Process

After the preparation of the pH, lactate, sodium ion sensing electrodes and the AgCl electrodes, these electrodes are integrated and laminated into one array. First, the electrodes are placed on the thermal lamination pouch (TP3854), as shown in Figure 6-1 (a). Then, the Scotch double-side tape is pasted on the other layer of the lamination pouch. Then, the Biopsy punch (086) with the diameter of 2.5 mm is used to open the sensing windows on the double side tape and the lamination pouch. Then, the electrodes are covered by the double-side tape and the lamination pouch with the sensing films exposed to the opening window, as shown in Figure 6-1 (b). Finally, the sensor-array is fed through the laminator. The 76.2-μm thick lamination pouch and the double-side tape work as the insulation layer. Figure 6-1 (c) shows a photo of the sensor-array.

6.2.6 Working Mechanism and Measurement Procedures of the Sensor-Array

A four-channel detection system was built in the following way:

- Channel 1 functioned as the pH detecting system, which collected the potentials generated between the pH sensing electrode and the AgCl reference electrode #1.

116
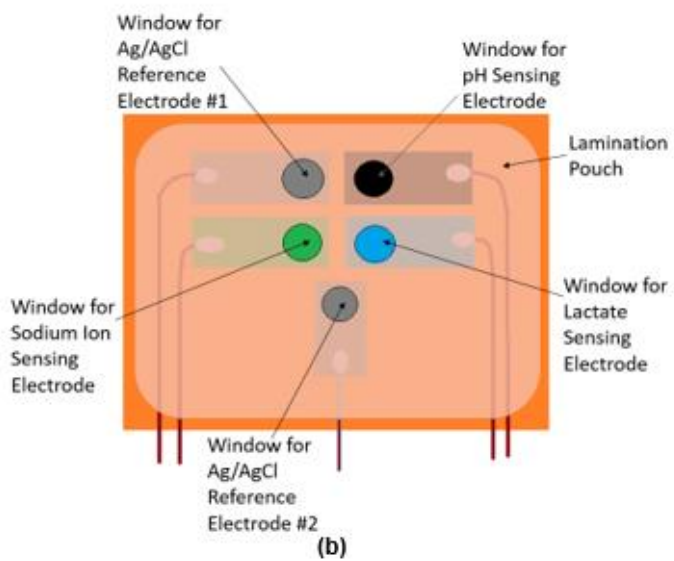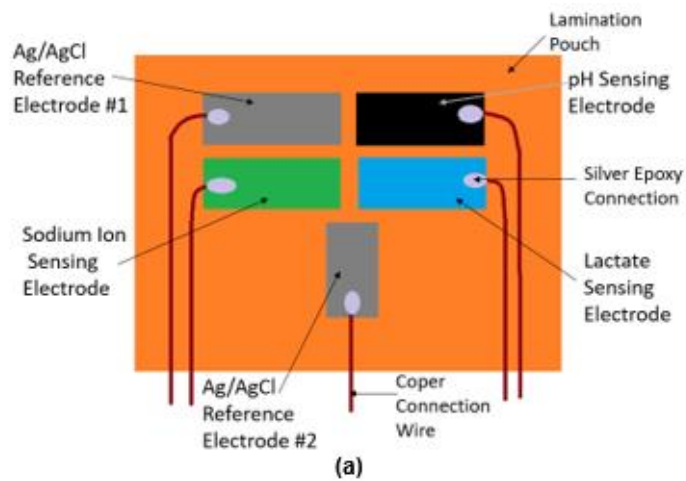
Figure 6- 1. (a) Graph of the sensor-array placed on the lamination pouch. (b) Graph of the end product of the sensor-array. (c) Photo of the sensor-array.

- Channel 2 functioned as the sodium ion detecting system, which collected the potentials generated between the sodium ion sensing electrode and the AgCl reference electrode #1.

- Channel 3 functioned as the lactate detecting system, which collected the current generated between the lactate sensing electrode and the AgCl reference electrode #1.

- Channel 4 functioned as the noise cancelation system, which collected the signals generated between the AgCl electrodes #1 and #2.

For the pH measurement, the sensor-array is tested in the artificial sweats with different pH levels. This pH testing range covers the range form the normal to abnormal sweat pH level. A data acquisition card (NI DAQ-609) with a LabVIEW-based program is used to record the real-time potentials at a 7.5 S/s sampling rate. The signal obtained from the channel 4 is subtracted from the channel 1. The calibrated result revealed the performance of the pH sensor.

For the sodium ion measurement, the sensor-array is tested in DI water with different concentration of Na+. A data acquisition card (NI DAQ-609) with a LabVIEW-based program is used to record the real-time potentials at a 7.5 S/s sampling rate. The signal obtained from the channel 4 is subtracted from the channel 2. The calibrated result revealed the performance of the sodium ion sensor.

For the lactate measurement, the sensor-array is tested in PBS, and PBS with different concentrations of Na^+ with successive additions of lactate. The temperature was maintained at 37 °C in a water bath to imitate the human body. A constant biasing voltage of 0.6 V is applied between the lactate sensing electrode and the AgCl reference electrode. The current generated between the two electrodes are recorded at a 10 S/s sampling rate. The signal obtained from the channel 4 is subtracted from the channel 3. The calibrated result the revealed the performance of the lactate sensor.

6.3. Preliminary Results and Discussion

6.3.1. pH Measurement Results

The pH sensor on the array is tested in the artificial sweats with pH levels of 4, 4.5, 5, 5.5, 6, 6.5, 7, 7.5, and 8. This pH testing range covers the sweat pH levels of the normal and abnormal situations. Figure 6-2 (a) shows the recorded potentials in the pH 4 to 8 artificial sweat solutions. The sensor shows step-responses when the pH level of the solution changes. The potentials settle quickly from a higher pH value to a lower one since there are more H+ ions available in the solution. It takes more time from the lower to higher pH solutions since there are ion residues on the porous sensing surface. The sensitivity is 59.2 mv/pH within the range of pH 4 and 8, as shown in Figure 6-2 (b).

It should be noted that the measurements are conducted in the artificial sweat in which abundant interfering ions exist. During the transition when the sensor is moved to the next test solution, the sensor electrode surface is not cleaned by de-ionized water, thus the interfering ion residues remain on the working and reference electrode surfaces. This is to imitate the realistic scenarios of continuous measurements. The hysteresis data are collected and the worst case is 6.93 mV which presents Δ pH = 0.117.

6.3.2. Sodium Ion Measurement Results

For the sodium ion measurement, the sensor-array is tested in DI water with different concentration of Na+ (40mM, 50mM, 60mM, 70mM, 80mM, and 90mM). The normal concentration of Na^+ in sweat of adults is 70 mmol/liter. The normal concentration of Na^+ in sweat of infant is 40 mmol/liter. And a significantly increased sweat Na+ concentration of 90-120 mmol/liter is observed for the adults with cystic fibrosis [6.6]. This Na^+ testing range covers the concentrations of Na^+ for the normal and abnormal situations. Figure 6-3 (a) shows the recorded potentials in the DI water with Na^+ from 40 mM to 90 mM. The sensor shows step-responses when the sodium ion concentrations changes. The potentials settle quickly with an average
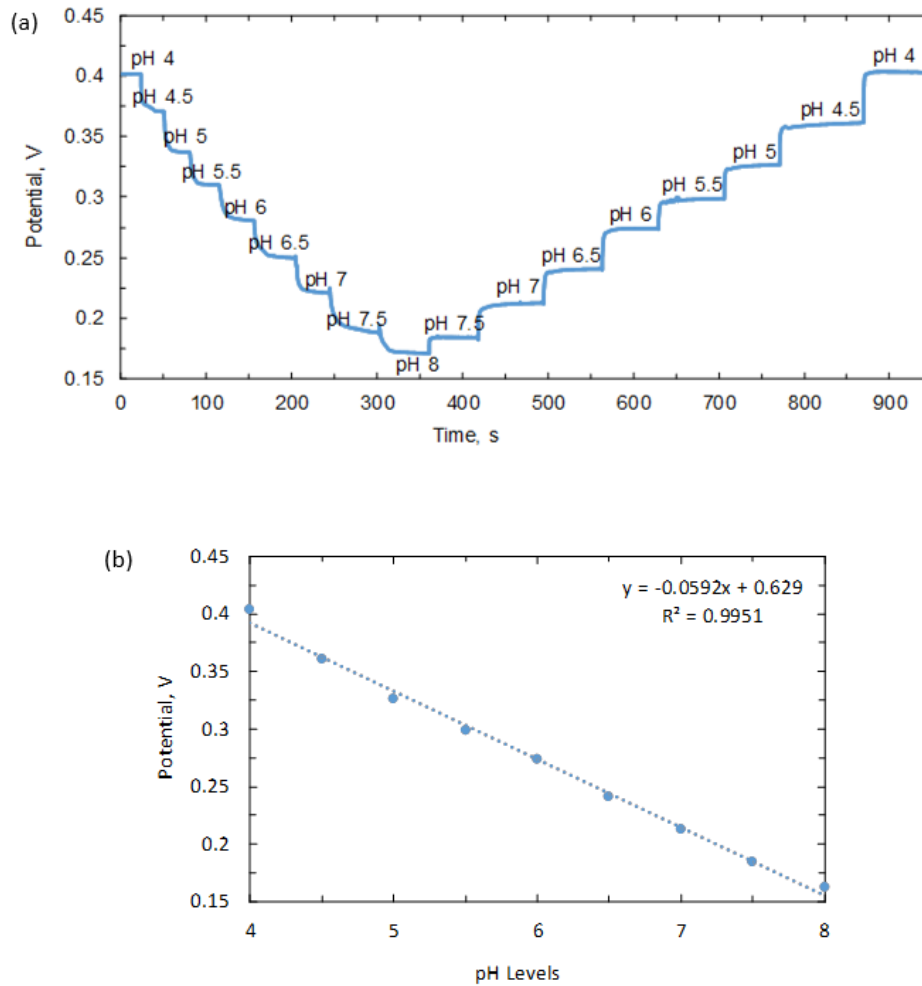
Figure 6- 2. (a) Responses and (b) sensitivity of the sensor tested in the artificial sweat with various pH levels.

responding time of 8 seconds. The sensitivity is 0.54 mv/mM within the range of 40-90 mM, as shown in Figure 6-3 (b). It should be noted that the measurements are conducted in the solution with abundant interfering ions exist. During the transition when the sensor is moved to the next test solution, the sensor electrode surface is not cleaned by de-ionized water, thus the interfering ion residues remain on the working and reference electrode surfaces. This is to imitate the realistic scenarios of continuous measurements.

6.3.3. Lactate Measurement Results

For the lactate measurement, the sensor-array is tested in PBS, PBS with 45 mM Na^+, and PBS with 90 mM Na^+ respectively, with successive additions of lactate. Mixing PBS with Na^+ is to imitate the sweat. The lactate concentration in sweat before exercise is around 20 mM, after exercise is around 60 mM. In our experiment, we increase the lactate concentrations in the testing solutions from 20 mM to 90 mM to cover the lactate concentration range.
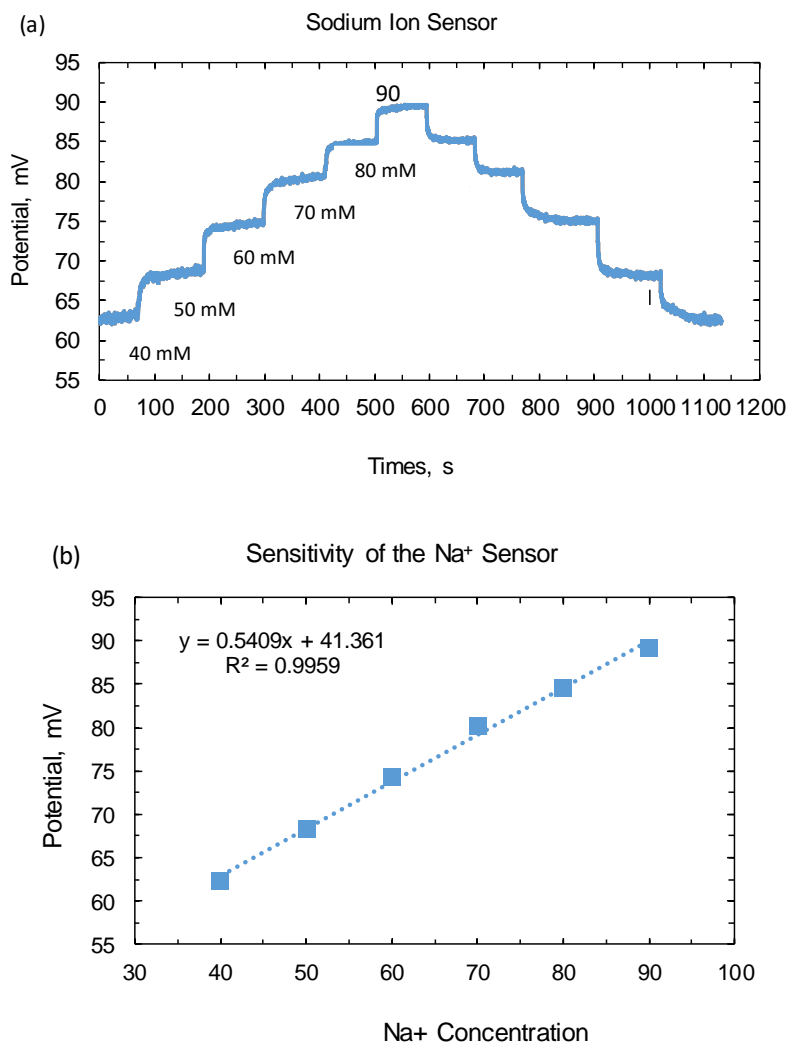
Figure 6- 3. (a) Responses and (b) sensitivity of the sensor tested in the DI water with different Na^+ concentrations.

Figure 6-4 shows the performance of the lactate sensor. The arrows indicate the time when lactic acid is applied to the solutions. Figure 6-4 (a) shows the recorded currents in the PBS with lactate concentration increases from 20 mM to 90 mM. The sensor shows step-responses
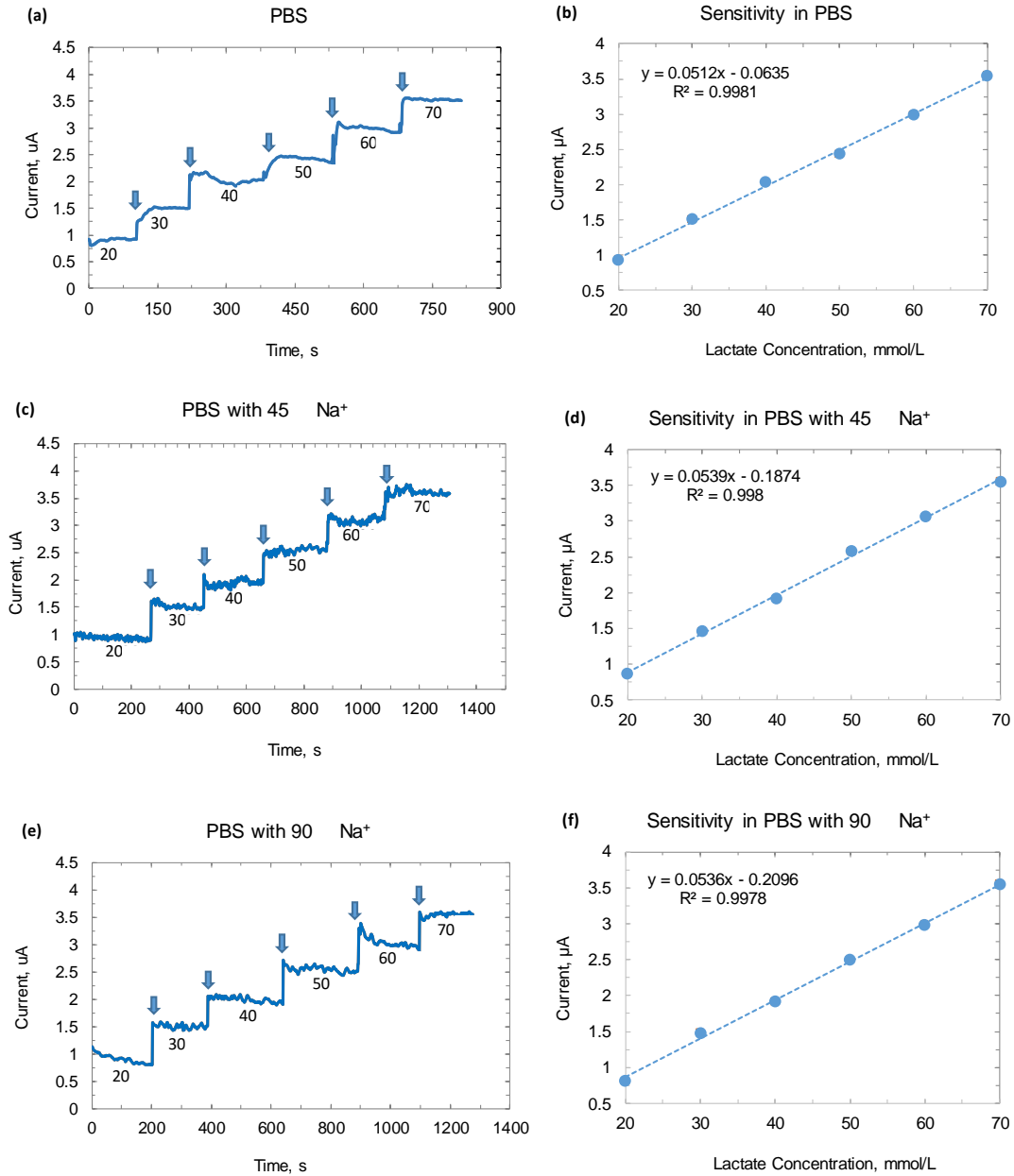
Figure 6- 4. The (a) performance and (b) sensitivity of the lactate sensor in PBS; The (c) performance and (d) sensitivity of the lactate sensor in PBS with 45 mM Na$^+$; The (e) performance and (f) sensitivity of the lactate sensor in PBS with 90 mMNa$^+$;

when the lactic acid is applied to the testing solution. Figure 6-4 (b) shows the sensor has a good linearity with the sensitivity of 51.2 nA/mM. Figure 6-4 (c) shows the recorded currents in the PBS with 45 mM Na^+. The sensor shows step-responses when the lactic acid is applied to the testing solution. Figure 6-4 (d) shows the good linearity of the sensor with the sensitivity of 53.9 nA/mM. Figure 6-4 (e) shows the recorded currents in the PBS with 90 mM Na^+. The sensor shows step-responses when the lactic acid is applied to the testing solution. Figure 6-4 (f) shows the good linearity of the sensor with the sensitivity of 53.6 nA/mM. In general, the sensor shows a standard deviation of 62.58nA, 22.65nA, 65.52nA, 72.59nA, 44.64nA, and 3.21nA for lactate concentrations 20mM, 30mM, 40mM, 50mM, 60mM, and 70mM respectively, which gives the lactate sensor an accuracy of around 1mM.

During the test the sensor electrode surface is not cleaned by de-ionized water to imitate the realistic scenarios of real-life measurements. It should be noted that there are different concentrations of interfering ions exist in the testing solutions which generates different degrees of the background noise, thus the noise level for the 3 tests are different.

6.4. Future Works

The future works include integration of a radio-frequency identification (RFID) integrated circuit for wireless pH sensing; embedded with an integrated programmable wireless system to detect different types of biomaterials; and embedded with a temperature sensor to provide more bio-information.

The RFID circuit is designed to cooperate with the IrOx pH sensor. It contains a transponder circuit and a reader circuit. The transponder circuit harvests radio frequency power transmitted from the reader circuit, and sends the modulated pH data as frequency shifts back to the reader circuit. The sensing concept is to form the resonant frequency and reach the coupling efficiency through inducting coupling between the coil antennas and capacitance. [6.10]

The integrated programmable wireless system includes a recorder and a receiver base station. The recorder includes a microcontroller for signal processing and a RF wireless

transmitter. The recorder is connected to the sensing electrode. The receiver base station includes a host computer which receives and display signals. The wearable recording system can be wirelessly powdered through inductive coupling transmitter antennas. [6.11]

Reference

[2.1]   M. Pourbaix, "Atlas of electrochemical equilibria in aqueous solutions," National Association of Corrosion Engineers, 1974.

[2.2]   Scott Brewer, Dwi Wicaksana, Jon-Paul Maria, Angus Kingon, and Stefan Franzen, "Investigation of the electrical and optical properties of iridium oxide by reflectance FTIR spectroscopy and density functional theory calculations," Chemical Physics, Vol. 313, pp. 25-31, 2005.

[2.3]   Akiyoshi Osaka, Toru Takatsuna, and Yoshinari Miura, "Iridium oxide films via sol-gel processing," Non-Crystalline Solds, Vol. 178, pp. 313-319, 1994

[2.4]   Sheng Yao, Min Wang, and Marc Madou, "A pH electrode based on melt-oxidized iridium oxide," Journal of the Electrochemical Society, Vol. 148, pp. 29-36, 2001.

[2.5]   Michael L. Hitchman, and Subramaniam Ramanathan, "A field-induced poising technique for promoting convergence of standard electrode potential values of thermally oxidized iridium pH sensors," Talanta, Vol. 39, pp. 137-144, 1992.

[2.6]   Michael S. Wilson, and R. David Rauh, "Novel amperometric immunosensors based on iridium oxide matrices," Biosensor and Bioelectronics, Vol. 19, pp. 693-699, 2004.

[2.7]   Keishi Nishio and Toshio Tsuchiya, "Electrochromic thin films prepared by sol-gel process," Solar Energy Materials& Solar Cells, Vol. 68, pp. 279-293, 2001.

[2.8]   C. Jefferey Brinker, George W. Scherer, "Sol-gel science: The physics and chemistry of sol-gel processing, " Academic Press, pp. 788-798, Boston, 1990.

[2.9]   Akiyoshi Osaka, Toru Takatsuna, and Yoshinari Miura, "Iridium oxide films via sol-gel processing," Non-Crystalline Solds, Vol. 178, pp. 313-319, 1994.

[2.10]   Kazusuke Yamanaka, "Anodically electrodeposited iridium oxide films (AIROF) from alkaline solutions for electrochromic display devices," Japanese Journal of Applied Physics, Vol. 28, pp. 632-637, 1989.

[2.11]   Weiland, J.D.; Anderson, D.J. Chronic Neural Stimulation with Thin-Film, Iridium Oxide Electrodes. IEEE Trans. Biomed. Eng. 2000, 47, 911–918.

[2.12]   Weiland, J.D.; Anderson, D.J.; Humayun, M.S. In Vitro Electrical Properties for Iridium Oxide Versus Titanium Nitride Stimulating Electrodes. IEEE Trans. Biomed. Eng. 2002, 49, 1574–1579.

[2.13]   Slavcheva, E.; Vitushinsky, R.; Mokwa, W.; Schnakenberg, U. Sputtered Iridium Oxide Films as Charge Injection Material for Functional Electrostimulation. J. Electrochem. Soc. 2004, 151, E226–E237.

[2.14]   Lee, I.; Whang, C.; Park, J.; Lee, D.; Seo, W. Biocompatibility and Charge Injection Property of Iridium Film Formed by Ion Beam Assisted Deposition. Biomaterials 2003, 24, 2225–2231.

[2.15]   Tolosa, V.M.; Wassum, K.M.; Maidment, N.T.; Monbouquette, H.G. Electrochemically Deposited Iridium Oxide Reference Electrode Integrated with an Electroenzymatic Glutamate Sensor on a Multi-Electrode Arraymicroprobe. Biosens. Bioelectron. 2013, 42, 256–260.

[2.16]   Nguyen, C., Rao, S., Yang, X., Dubey, S., Mays, J., Cao, H., & Chiao, J. C. (2015). Sol-gel deposition of iridium oxide for biomedical micro-devices. *Sensors*, *15*(2), 4212-4228.

[2.17]   Huang, Wen-Ding, Hung Cao, Sanchali Deb, Mu Chiao, and Jung-Chih Chiao. "A flexible pH sensor based on the iridium oxide sensing film." *Sensors and Actuators A: Physical* 169, no. 1 (2011): 1-11.

[2.18]   Cogan, Stuart F., Andrew A. Guzelian, William F. Agnew, Ted GH Yuen, and Douglas B. McCreery. "Over-pulsing degrades activated iridium oxide films used for intracortical neural stimulation." *Journal of neuroscience methods* 137, no. 2 (2004): 141-150.

[2.19]   Wilson, Michael S., and R. David Rauh. "Novel amperometric immunosensors based on iridium oxide matrices." *Biosensors and Bioelectronics* 19.7 (2004): 693-699.

[2.20]   Yang, H., Kang, S. K., Choi, C. A., Kim, H., Shin, D. H., Kim, Y. S., & Kim, Y. T. (2004). An iridium oxide reference electrode for use in microfabricated biosensors and biochips. *Lab on a Chip*, *4*(1), 42-46.

[3.1]   V. P. Zanini; B. L. de Mishima; and V. Solís. An amperometric biosensor based on lactate oxidase immobilized in laponite–chitosan hydrogel on a glassy carbon electrode. Application to the analysis of l-lactate in food samples. Sensors and Actuators B: Chemical 2011, 155, 75-80.

[3.2]   S. Suman; R. Singhal; A. L. Sharma; B. Malthotra; and C. Pundir. Development of a lactate biosensor based on conducting copolymer bound lactate oxidase. Sensors and Actuators B: Chemical 2005, 107, 768-772.

[3.3]   K. Hibi; K. Hatanaka; M. Takase; H. Ren; and H. Endo. Wireless biosensor system for real-time L-lactic acid monitoring in fish. Sensors 2012 , 12, 6269-6281.

[3.4]   F. Palmisano; M. Quinto; R. Rizzi; and P. Zambonin. Flow injection analysis of L-lactate in milk and yoghurt by on-line microdialysis and amperometric detection at a disposable biosensor. Analyst 2001, 126, 866-870.

[3.5]   H. Ishii and Y. Nishida. Effect of lactate accumulation during exercise-induced muscle fatigue on the sensorimotor cortex. Journal of physical therapy science 2013, 25, 1637-2013.

[3.6]   S. Walenta; A. Salameh; H. Lyng; J. F. Evensen; M. Mitze; E. K. Rofstad. Correlation of high lactate levels in head and neck tumors with incidence of metastasis. The American journal of pathology 1997, 150, 409-1997.

[3.7]   S. Walenta; M. Wetterling; M. Lehrke; G. Schwickert; K. Sundfør; and E. K. Rofstad. High lactate levels predict likelihood of metastases, tumor recurrence, and restricted patient survival in human cervical cancers. Cancer research 2000, 60, 916-921.

[3.8]   K. Wasserman and B. J. Whipp. Exercise Physiology in Health and Disease. American Review of Respiratory Disease 1975, 219-249.

[3.9] H. Lange and R. Jäckel. Usefulness of plasma lactate concentration in the diagnosis of acute abdominal disease. The European journal of surgery= Acta chirurgica 1993, 160, 381-384.

[3.10] R. Park. Lactic acidosis. Western Journal of Medicine 1980, 133, 418.

[3.11] D. B. Pyne; T. Boston; D. T. Martin; and A. Logan. Evaluation of the Lactate Pro blood lactate analyser. European journal of applied physiology 2000, 82, 112-116.

[3.12] Phypers; Barrie; and JM Tom Pierce. Lactate physiology in health and disease. Continuing Education in Anaesthesia, Critical Care & Pain 2006, 6.3, 128-132.

[3.13] H. B. Nguyen; E. P. Rivers; B. P. Knoblich; G. Jacobsen; A. Muzzin; J. A. Ressler. Early lactate clearance is associated with improved outcome in severe sepsis and septic shock*. Critical care medicine 2004, 32, 1637-1642.

[3.14] W. Bernal; N. Donaldson; D. Wyncoll; and J. Wendon. Blood lactate as an early predictor of outcome in paracetamol-induced acute liver failure: a cohort study. The Lancet 2002, 359, 558-563.

[3.15] B. Gastrin; H. Briem; and L. Rombo. Rapid diagnosis of meningitis with use of selected clinical data and gas-liquid chromatographic determination of lactate concentration in cerebrospinal fluid. Journal of infectious diseases 1979, 139, 529-533.

[3.16] Y. Hu; Y. Zhang; and G. S. Wilson. A needle-type enzyme-based lactate sensor for in vivo monitoring. Analytica Chimica Acta 1993, 281, 503-511.

[3.17] J. Bakker; M. W. Nijsten; and T. C. Jansen. Clinical use of lactate monitoring in critically ill patients. Annals of intensive care 2013, 3, 12.

[3.18] D. A. Baker and D. A. Gough. A continuous, implantable lactate sensor. Analytical Chemistry 1995, 67, 1536-1540.

[3.19] A. C. B. Dias; R. A. O. Silva; and M. A. Z. Arruda. A sequential injection system for indirect spectrophotometric determination of lactic acid in yogurt and fermented mash samples. Microchemical Journal 2010, 96.1, 151-156.

[3.20] Henry H; Marmy Conus N; Steenhout P; Béguin A; and Boulat O. Sensitive determination of d-lactic acid and l-lactic acid in urine by high-performance liquid chromatography–tandem mass spectrometry. Biomedical Chromatography 2012, 26.4, 425-428.

[3.21] Fumiyuki Yamasaki; Kaoru Kurisu; Yoshinori Kajiwara; Yosuke Watanabe; Takeshi Takayasu; Yuji Akiyama; Taiichi Saito; Ryosuke Hanaya; and Kazuhiko Sugiyama. Magnetic resonance spectroscopic detection of lactate is predictive of a poor prognosis in patients with diffuse intrinsic pontine glioma. Neuro-oncology 2011, 13. 7, 791-801.

[3.22] Dale A. Baker and David A. Gough. A continuous, implantable lactate sensor. Analytical Chemistry 1995, 67.9, 1536-1540.

[3.23] C. G. J. Schabmueller; D. Loppow; G. Piechotta; B. Schütze; J. Albers; and R. Hintsche. Micromachined sensor for lactate monitoring in saliva. Biosensors and Bioelectronics 2006, 21.9, 1770-1776.

[3.24] Jason J. Burmeister; Michael Palmer; and Greg A. Gerhardt. L-lactate measures in brain tissue with ceramic-based multisite microelectrodes. Biosensors and Bioelectronics 2005, 20.9, 1772-1779.

[3.25] J. Perdomo; H. Hinkers; C. Sundermeier; W. Seifert; O. Martınez Morell; and M. Knoll. Miniaturized real-time monitoring system for L-lactate and glucose using microfabricated multi-enzyme sensors. Biosensors and Bioelectronics 2000, 15.9, 515-522.

[3.26] Anthony Guiseppi-Elie; Sean Brahim; Gymama Slaughter; and Kevin R. Ward. Design of a subcutaneous implantable biochip for monitoring of glucose and lactate. IEEE Sensors Journal 2005, 5.3, 345-355.

[3.27] Ryoji Kurita; Katsuyoshi Hayashi; Xu Fan; Katsunobu Yamamoto; Takeshi Kato; and Osamu Niwa. Microfluidic device integrated with pre-reactor and dual enzyme-modified microelectrodes for monitoring in vivo glucose and lactate. Sensors and Actuators B: Chemical 2002, 87.2, 296-303.

[3.28]   Alexander F. Revzin; Kaushik Sirkar; Aleksandr Simonian; and Michael V. Pishko. Glucose, lactate, and pyruvate biosensor arrays based on redox polymer/oxidoreductase nanocomposite thin-films deposited on photolithographically patterned gold microelectrodes. Sensors and Actuators B: Chemical 2002, 81.2, 359-368.

[3.29]   Andreas Weltin; Jochen Kieninger; Barbara Enderle; Anne-Kathrin Gellner; Brita Fritsch; and Gerald A. Urban. Polymer-based, flexible glutamate and lactate microsensors for in vivo applications. Biosensors and Bioelectronics 2014, 61, 192-199.

[3.30]   Pratima Labroo and Yue Cui. Flexible graphene bio-nanosensor for lactate. Biosensors and Bioelectronics 2014, 41, 852-856.

[3.31]   Wenzhao Jia; Amay J. Bandodkar; Gabriela Valdés-Ramírez; Joshua R. Windmiller; Zhanjun Yang; Julian Ramírez; Garrett Chan; and Joseph Wang. Electrochemical tattoo biosensors for real-time noninvasive lactate monitoring in human perspiration. Analytical chemistry 2013, 85.14, 6553-6560.

[3.32]   Dion Khodagholy; Vincenzo F. Curto; Kevin J. Fraser; Moshe Gurfinkel; Robert Byrne; Dermot Diamond; George G. Malliaras; Fernando Benito-Lopez; and Roisin M. Owens. Organic electrochemical transistor incorporating an ionogel as a solid state electrolyte for lactate sensing. Journal of Materials Chemistry 2012, 22.10, 4440-4443.

[3.33]   Cuong M. Nguyen; Jeffrey Mays; Hung Cao; Haydn Allard; Smitha Rao; and J-C. Chiao. A Wearable system for highly selective l-Glutamate neurotransmitter sensing. Biomedical Wireless Technologies, Networks, and Sensing Systems (BioWireleSS), IEEE Topical Conference on 2015, 1-3.

[3.34]   C. M. Nguyen; S. Rao; X. Yang; S. Dubey; J. Mays; and H. Cao. Sol-Gel Deposition of Iridium Oxide for Biomedical Micro-Devices. Sensors 2015, 15, 4212-4228.

[3.35]   James A. Cox and Krzysztof Lewinski. Flow injection amperometric determination of hydrogen peroxide by oxidation at an iridium oxide electrode. Talanta 1993, 40.12, 1911-1915.

[3.36] B. Ziaie; J. Von Arx; and K. Najafi. A micro-fabricated planar high-current IrOx stimulating microelectrode. Engineering in Medicine and Biology Society. Bridging Disciplines for Biomedicine. Proceedings of the 18th Annual International Conference of the IEEE 1996, 270-271.

[3.37] B. Ziaie; Y. Gianchandani; and K. Najafi. A high-current IrOx thinfilm neuromuscular microstimulator. Proc. 6th Int. Conf. Solid-State Sensors and Actuators 1991, 124-127.

[3.38] J.V. Dobson; P.R. Snodin; and H.R. Thirsk. EMF measurements of cells employing metal–metal oxide electrodes in aqueous chloride and sulphate electrolytes at temperatures between 25–250 ˚C. Electrochemical Acta 1976, 21, 527–533.

[3.39] K. Yamanaka. Anodically electrodeposited iridium oxide films (AEIROF) from alkaline solutions for electrochromic display devices. Japanese Journal of Applied Physics 1989, 28, 632–637.

[3.40] N. Hirst; L. Hazelwood; D. Jayne; and P. Millner. An amperometric lactate biosensor using H2O2 reduction via a Prussian Blue impregnated poly (ethyleneimine) surface on screen printed carbon electrodes to detect anastomotic leak and sepsis. Sensors and Actuators B: Chemical 2013, 186, 674-680.

[3.41] M. Gamero; F. Pariente; E. Lorenzo; and C. Alonso. Nanostructured rough gold electrodes for the development of lactate oxidase-based biosensors. Biosensors and Bioelectronic 2010, 25, 2038-2044.

[3.42] B. Ziaie; J. Von Arx; and K. Najafi. A micro-fabricated planar high-current IrOx stimulating microelectrode. Engineering in Medicine and Biology Society. Bridging Disciplines for Biomedicine. Proceedings of the 18th Annual International Conference of the IEEE, 1996, 270-271.

[3.43] J. Hoogvliet; M. Dijksma; B. Kamp; and W. Van Bennekom. Electrochemical pretreatment of polycrystalline gold electrodes to produce a reproducible surface roughness for self-assembly: a study in phosphate buffer pH 7.4. Analytical chemistry 2000, 72, 2016-2021.

[3.44]   A. A. F. Grupioni; E. Arashiro; and T. A. F. Lassali. Voltammetric characterization of an iridium oxide-based system: the pseudocapacitive nature of the Ir0.3 Mn0.7O2 electrode. Electrochimica acta 2002, 48, 407-418.

[4.1]   John G. Webster, "The measurement, instrumentation and sensors handbook," CRC Press and IEEE Press, 71-1, 1999.

[4.2]   Afsaneh Safavi, et. al., "Novel optical pH sensor for high and low pH values," Sensors and Actuators, 90, 143-150, 2003.

[4.3]   Patrick J. Kinlen, et. al., "A solid-state pH sensor based on a Nafion-coated iridium oxide indicator electrode and a polymer-based silver chloride reference electrode," Sensors and Actuators B, 22, 13-25, 1994

[4.4]   Głab, StanisŁAw, et al. "Metal-metal oxide and metal oxide electrodes as pH sensors." Critical Reviews in Analytical Chemistry 21.1 (1989): 29-47.

[4.5]   C. M. Nguyen, et. al., "A Sol-gel Iridium Oxide based pH Sensor Array on Flexible Polyimide Substrate," IEEE Sensors Journal, 13(10), 3857 – 3864, 2013.

[4.6]   M. Pourbaix, "Atlas of electrochemical equilibria in aqueous solutions," National Association of Corrosion Engineers, pp. 374-377, 1974.

[4.7]   Sheng Yao, Min Wang, and Marc Madou, "A pH electrode based on melt-oxidized iridium oxide," Journal of the Electrochemical Society, Vol. 148, pp. 29-36, 2001. 4

[4.8]   M. Pourbaix, "Atlas of electrochemical equilibria in aqueous solutions," National Association of Corrosion Engineers, pp. 374-377, 1974. 5

[4.9]   Erno Pungor, "The theory of ion-selective electrodes," Analytical Sciences. Vol. 14, pp. 249-256, 1998. 6

[4.10] Agner Fog, and Richard P. Buck, "Electronic semiconducting oxides as pH sensors,"Sensors and Actuators, Vol. 6, pp. 137-146, 1984. 7

[4.11]   W. Olthuis, M. A. M. Robben, P. Bergveld, M. Bos and, W. E. van der Linden, "pH sensor properties of electrochemically grown iridium oxide," Sensor and Actuators B, Vol. 2, pp. 247-256, 1990. 8

[4.12]   Keishi Nishio and Toshio Tsuchiya, "Electrochromic thin films prepared by sol-gel process," Solar Energy Materials& Solar Cells, Vol. 68, pp. 279-293, 2001. 11

[4.13]   C. Jefferey Brinker, George W. Scherer, "Sol-gel science: The physics and chemistry of sol-gel processing, " Academic Press, pp. 788-798, Boston, 1990. 12

[4.14]   Akiyoshi Osaka, Toru Takatsuna, and Yoshinari Miura, "Iridium oxide films via sol-gel processing," Non-Crystalline Solds, Vol. 178, pp. 313-319, 1994. 13

[4.15]   Kazusuke Yamanaka, "Anodically electrodeposited iridium oxide films (AIROF) from alkaline solutions for electrochromic display devices," Japanese Journal of Applied Physics, Vol. 28, pp. 632-637, 1989. 14

[4.16]   C. Jefferey Brinker, George W. Scherer, "Sol-gel science: The physics and chemistry of sol-gel processing, " Academic Press, pp. 788-798, Boston, 1990.

[4.17]   Huang, Wen-Ding, "A pH Sensor Based on A Flexible Substrate," (Electrical Engineering, 2014, The University of Texas at Arlington)

[4.18]   H. E. Amor, A. B. Kouki, P. Marsh, K. T. Kim, and H. Cao, "Development of a novel miniaturized LTCC-based wireless pH sensing system," in SENSORS, 2016 IEEE, 2016, pp. 1-3.

[4.19]   Marsh, Paul, Wyatt Moore, Mark Clucas, Ly Huynh, Kyoung-Tae Kim, Soyeon Yi, Hung Cao, and J-C. Chiao. "Characterization of flexible pH micro-sensors based on electrodeposited IrOx thin film." In 2017 IEEE SENSORS, pp. 1-3. IEEE, 2017.

[4.20]   Marsh, Paul, Wyatt Moore, Mark Clucas, Ly Huynh, Kyoung-Tae Kim, Soyeon Yi, Hung Cao, and J-C. Chiao. "Characterization of flexible pH micro-sensors based on electrodeposited IrOx thin film." In 2017 IEEE SENSORS, pp. 1-3. IEEE, 2017.

[4.21]   Elsen, Heather Alyssa. Thermodynamic and Dynamic Investigations of Hydrated Iridium Oxide Potentiometric PH Micro-sensors. University of California, Berkeley, 2007.

[4.22]   C. M. Nguyen, H.C., W. D. Huang, and J.-C. Chiao, An Electro-Deposited IrOx Thin Film pH Sensor, in BMES Biomedical Engineering Society Annual Meeting: Hartford, 2011.

[4.23]   Huang W, Cao H, Deb S, Chiao M, Chiao JC. "A flexible pH sensor based on the iridium oxide sensing film," Sensors & Actuators: A. Physical, pp.1-11, 2011

[4.24]   Ges, I.A., Ivanov, B.L., Schaffer, D.K., Lima, E.A., Werdich, A.A. & Baudenbacher, F.J., "Thin-film IrOx pH microelectrode for microfluidic-based microsystems", Biosensors & bioelectronics, vol. 21, no. 2, pp. 248, 2005.

[4.25]   Ges IA, Ivanov BL, Werdich AA, Baudenbacher FJ. "Differential pH measurements of metabolic cellular activity in nl culture volumes using micro fabricated iridium oxide electrodes," Biosensors and Bioelectronics, pp.22:1303-1310, 2007

[4.26]   Marzouk, S. A., S. Ufer, R. P. Buck, et al. "Electrodeposited Iridium Oxide pH Electrode for Measurement of Extracellular Myocardial Acidosis during Acute Ischemia," Analytical Chemistry, vol. 70/no. 23, pp. 5054-5061, 1998

[4.27]   Marzouk SAM, "Improved electrodeposited iridium oxide pH sensor fabricated on etched titanium substrates," Analytical chemistry, pp.1258-1266, 2005

[4.28]   Saeid Kakooei, Mokhtar Che Ismail, Bambang Ari-Wahjoediz, "An overview of pH Sensors Based on Iridium Oxide: Fabrication and Application," International Journal of Material Science Innovations, pp. 62-72, 2013

[4.29]   Chiao, Jung-Chih. "COMPARISON OF DIFFERENT METALS AS ELECTRODES FOR A FLEXIBLE MICRO pH SENSOR." PhD diss., 2016.

[4.30]   L. Bousse, S. Mostarshed, B. van der Schoot, N.F. de Rooij, Comparison of the hysteresis of Ta2O5 and Si3N4 pH-sensing insulators, Sens. Actuators B 17 (1994) 157–164.

[4.31]   P. Woias, L. Meixner, P. Frostl, Slow pH response effects of silicon nitride ISFET sensors, Sens. Actuators B 48 (1998) 501–504.

[4.32]   J.-C. Chou, C.-Y. Weng, Sensitivity and hysteresis effect in Al2O3 gate pH-ISFET, Mater. Chem. Phys. 71 (2001) 120–124.

[4.33]   D.-H. Kwon, B.-W. Cho, C.-S. Kim, B.-K. Sohn, Effects of heat treatment on Ta2O5 sensing membrane for low drift and high sensitivity pH-ISFET, Sens. Actuators B 34 (1996) 441–445.

[4.34]   Tsai, Chu-Neng, et al. "Study on the sensing characteristics and hysteresis effect of the tin oxide pH electrode." Sensors and Actuators B: Chemical 108.1-2 (2005): 877-882.

[4.35]   L. Bousse, H.H. van den Vlekkert, N.F. de Rooij, Hysteresis in Al2O3-gate ISFETs, Sens. Actuators B 2 (1990) 103–110.

[4.36]   Robinson, Howard W., "The influence of neutral salts on the pH of phosphate buffer mixtures," Journal of Biological Chemistry, vol. 82.3, pp. 775-802, 1929.

[4.37]   Cheng, K. L., and Da-Ming Zhu, "On calibration of pH meters," Sensors vol. 5.4, pp. 209-219, 2005.

[4.38]   Souza, Vanderléa de, Alberto Pires Ordine, Isabel Cristina Serta Fraga, Monique Audrey Getrouw, Paulo Paschoal Borges, Jailton Carreteiro Damasceno, and Paulo Roberto Guimarães Couto, "Effect of NaCl and HCl concentrations on primary pH measurement for the certification of standard materials," Brazilian Archives of Biology and Technology vol. 49, pp. 79-86, 2006.

[4.39]   Kakooei, Saeid, Mokhtar Che Ismail, and Bambang Ari-Wahjoedi, "An overview of pH sensors based on iridium oxide: fabrication and application," Int. J. Mater. Sci. Innovat vol. 1, pp. 62-72, 2013.

[4.40]   Lin, Jyh-Ling, and Hsiang-Yi Hsu, "Study of sodium ion selective electrodes and differential structures with anodized indium tin oxide," Sensors, vol. 10.3, pp.1798-1809, 2010.

[5.1]   J. L. Parra and M. Paye, "EEMCO Guidance for the in Vivo Assessment of Skin Surface pH," Skin Pharmacology and Physiology, Vol. 16, No. 3, pp. 188-202, 2003.

[5.2]   A. Zlotogorski, "Distribution of Skin Surface pH on the Forehead and Cheek of Adults," Archives of dermatological research, Vol 279, No. 6, pp. 398-401, 1987.

[5.3]   S. Dikstein and A. Zlotogorski, "Measurement of Skin pH," Acta dermato-venereologica Supplementum, Vol. 185, pp. 18-20, 1994.

[5.4]   Chikakane, Kenichiro, and H. Takahashi, "Measurement of Skin pH and its Significance in Cutaneous Diseases," Clinics in dermatology, Vol. 13, No. 4, pp. 299-306, 1995.

[5.5]   W. M. Jeanette and H. I. Maibach, "Age and Skin Structure and Function, a Quantitative Approach (I): Blood Flow, pH, Thickness, and Ultrasound Echogenicity," Skin research and technology, Vol. 11, No.4, pp. 221-235, 2005.

[5.6]   J. W. Fluhr and P. M. Elias, "Stratum Corneum pH: Formation and Function of the 'Acid Mantle'," Exogenous Dermatology, Vol. 1, No.4, pp. 163-175, 2002.

[5.7]   F. Rippke, V. Schreiner, and H. J. Schwanitz, "The Acidic Milieu of the Horny Layer," American Journal of Clinical Dermatology, Vol. 3, No.4, pp. 261-272, 2002.

[5.8]   M.A Farage, K. W. Miller, P. Elsner, and H. I. Maibach, "Intrinsic and Extrinsic Factors in Skin Ageing: a Review," International Journal of Cosmetic Science, Vol. 30, No. 2, pp. 87-95, 2008.

[5.9]   K. P Wilhelm, A. B Cua, and H. I. Maibach, "Skin Aging: Effect on Transepidermal Water Loss, Stratum Corneum Hydration, Skin Surface pH, and Casual Sebum Content," Archives of dermatology, Vol. 127, No. 12, pp. 1806-1809, 1991.

[5.10]   M. A Farage, K. W Miller, P. Elsner and H. I. Maibach, "Characteristics of the Aging Skin," Advances in wound care, Vol. 2, No. 1, pp. 5-10, 2013.

[5.11]   J. Kottner, A. Lichterfeld, and U. Blume‑Peytavi, "Maintaining Skin Integrity in the Aged: a Systematic Review," British Journal of Dermatology, Vol. 169, No. 3, pp. 528-542, 2013.

[5.12]   Y. C. Jung, E. J Kim, J. C. Cho, K. D. Suh and G. W. Nam, "Effect of Skin pH for Wrinkle Formation on Asian: Korean, Vietnamese and Singaporean," Journal of the European Academy of Dermatology and Venereology, Vol. 27, No. 3, pp. 328-332, 2013.

[5.13]   E.J. Kim, J.Y. Han, H.K. Lee, Q.Q. He, J.C. Cho, L. Wei, X. Wang, L. Li, L. Wei, H. Liang and X. Gao, "Effect of the Regional Environment on the Skin Properties and the Early Wrinkles in Young Chinese Women," Skin Research and Technology, Vol. 20, No. 4, pp. 498-502, 2014.

[5.14]   E. A. Grice and J. A. Segre, "The Skin Microbiome," Nature Reviews Microbiology, Vol. 9, No. 4, pp. 244-253, 2011.

[5.15]   C. M. Nguyen, H.C., W. D. Huang, and J.-C. Chiao, An Electro-Deposited IrOx Thin Film pH Sensor, in BMES Biomedical Engineering Society Annual Meeting: Hartford, 2011.

[5.16]   Huang W, Cao H, Deb S, Chiao M, Chiao JC. "A flexible pH sensor based on the iridium oxide sensing film," Sensors & Actuators: A. Physical, pp.1-11, 2011

[6.1]   He, Xuecheng, Tailin Xu, Zhen Gu, Wei Gao, Li-Ping Xu, Tingrui Pan, and Xueji Zhang. "Flexible and superwettable bands as a platform toward sweat sampling and sensing." Analytical chemistry 91, no. 7 (2019): 4296-4300.

[6.2]   Parlak, O., Keene, S.T., Marais, A., Curto, V.F. and Salleo, A., 2018. Molecularly selective nanoporous membrane-based wearable organic electrochemical device for noninvasive cortisol sensing. Science advances, 4(7), p. 2904.

[6.3]   Gao, Wei, Sam Emaminejad, Hnin Yin Yin Nyein, Samyuktha Challa, Kevin Chen, Austin Peck, Hossain M. Fahad et al. "Fully integrated wearable sensor arrays for multiplexed in situ perspiration analysis." Nature 529, no. 7587 (2016): 509.

[6.4]   Tai, Li‑Chia, Wei Gao, Minghan Chao, Mallika Bariya, Quynh P. Ngo, Ziba Shahpar, Hnin YY Nyein et al. "Methylxanthine drug monitoring with wearable sweat sensors." Advanced Materials 30, no. 23 (2018): 1707442.

[6.5]   M. J. Patterson, S. D. R. Galloway and M. A. Nimmo, "Effect of Induced Metabolic Alkalosis on Sweat Composition in Me," Acta Physiologica Scandinavica, Vol. 174, No. 1, pp. 41-46, 2002.

[6.6] W. P. Nikolayek and H. M. Emrich, "pH of Sweat of Patients with Cystic Fibrosis," Clinical Weekly, Vol. 54, No.6, pp. 287-288, 1976.

[6.7] K. Chikakane, and H. Takahashi, "Measurement of Skin pH and its Significance in Cutaneous Diseases," Clinics in dermatology, Vol. 13, No.4, pp. 299-306, 1995.

[6.8] Speedy DB, Noakes TD, Schneider C. Exercise-associated hyponatremia: a review. Emerg. Med. 2001; 13:17–27.

[6.9] Ferner, S., et al. "Reference values of Na (+) and Cl (-) concentrations in adult sweat." Zeitschrift fur Erkrankungen der Atmungsorgane 175.2 (1990): 70-75.

[6.10] T. Ativanishayaphong, J. Wang, W. Huang, S. Rao, and J.C. Chiao, "A simple wireless batteryless sensing platform for resistive and capacitive sensor," IEEE Sensors, Vol. 1, pp. 139-142, 2007.

[6.11] Nguyen, Cuong M., et al., IEEE MTT-S International Microwave Symposium, 2015, pp. 1-4.

Appendix A

RECIPES TO COAT PHOTORESIST

The positive photoresist S1813 is used as the wet etching mask in the process for forming metal electrode pattern. The following recipe is applied with the exposure wavelength of 365 nm.

- Step 1: Spin coat photoresist S1813 for 5 seconds at 500 rpm and another 60 seconds at 3000 rpm.

- Step 2: Soft-bake at 90°C for 3 minutes.

- Step 3: Expose for 8 seconds under a power of 20 mW/cm^2.

- Step 4: Develop in developer MF-319 for 25 seconds.

- Step 5: Clean with DI and blow dry.

The negative photoresist SU8-25 is used to form the insulation layer. A 40-μm thick SU8-25 layer is obtained with the following recipe. The exposure wavelength is 365 nm.

- Step 1: Spin coat photoresist SU8-25 for 10 seconds at 500 rpm and another 45 seconds at 1000 rpm.

- Step 2: Pre-bake at 65°C for 5 minutes, and 95°C for 15 minutes.

- Step 3: Expose for 15 seconds under a power of 20 mW/cm^2.

- Step 4: Post-exposure bake at 65°C for 1 minute and 95°C for 15 minutes.

- Step 5: Develop in SU8 developer for 6 minutes.

- Step 6: Clean with propanol and DI, then blow dry.

The negative photoresist SU8-100 is used as the sacrificial layer in the sol-gel process. The following recipe is applied with the exposure wavelength of 365 nm.

- Step 1: Spin coat photoresist SU8-100 for 30 seconds at 3000 rpm and another 30 seconds at 4000 rpm.

- Step 2: Pre-bake at 65°C for 10 minutes and 95°C for 40 minutes.

- Step 3: Expose for 30 seconds under a power of 20 mW/cm^2.

- Step 4: Post-exposure bake at 65°C for 5 minutes and 95°C for 20 minutes.

- Step 5: Develop in SU8 developer for 10 minutes.

- Step 6: Clean with propanol and DI, then dry at 65°C for 5 minutes.

Biographical Information

Xuesong Yang was born in Liaoning, Chian. She received her Bachelor of Science in Electrical Engineering degree from Liaoning Normal University (China) in 2012 with her thesis title "Chaos Model of the Er-Doped Optical Amplifier". Shen received her Master of Science in Technology degree from Texas State University-San Marcos in 2014 with her thesis title "Highly Sensitive Biosensor based on Graphene Field Effect Transistor". Since 2014, she joined iMEMS research group and focused on design and fabrication of implantable and flexible electrochemical sensors featuring with iridium oxide for biomedical applications. Her current research interests include MEMS and BioMEMS devices fabrication, nanotechnology, flexible microelectronics, biomedical sensing systems, and wireless technologies. She is a member of IEEE and BMES societies.